Lyle, M., Wilson, P.A., Janecek, T.R., et al., 2002
Proceedings of the Ocean Drilling Program, Initial Reports Volume 199

10. Site 1217[1]

Shipboard Scientific Party[2]

BACKGROUND AND OBJECTIVES

Site 1217 (16°52.02′N, 138°06.00′W; 5342 meters below sea level [mbsl]; Fig. F1) is one of seven sites drilled to target upper Paleocene crust along a latitudinal transect during Leg 199 and will be used to investigate paleoceanographic processes in the northern tropical early Eocene Pacific Ocean. Site 1217 is situated ~1° north of the Clarion Fracture Zone on abyssal hill topography typical of the central Pacific. Based on magnetic lineations, basement age at Site 1217 should be in magnetic Anomaly C25r or ~57 Ma (Cande et al., 1989; timescale of Cande and Kent, 1995). The Cenozoic history of sedimentation in this region was poorly constrained prior to Leg 199 drilling because the nearest drill site (Deep Sea Drilling Project [DSDP] Site 162) is situated ~300 km south and west on 48-Ma crust. Based on data from this early rotary-cored hole, magnetic anomaly maps, a shallow-penetration piston core near Site 1217 (EW9709-4PC), and seismic profiling (Fig. F2), we expected the sedimentary sequence at Site 1217 to comprise a relatively thick (25 to 35 m thick) section of red clays overlying a radiolarian ooze and a basal carbonate section with possible chert near basement (estimated total depth ~125–150 meters below seafloor [mbsf]) deposited when the site was near the ridge crest in the late Paleocene and early Eocene.

Site 1217 was chosen because it is anticipated to have been located just outside of the equatorial region at 56 Ma, ~5°N, 106°W based upon a fixed hotspot model (Gripp and Gordon, 1990, for 0- to 5-Ma Pacific hotspot rotation pole; Engebretson et al., 1985, for older poles). On the same basis at 40 Ma, the site was located at ~8°N, 111°W. Thus, Site 1217 should help define the paleoceanography of the northern tropical Pacific, in particular locating the ancient North Equatorial Countercurrent (NECC) region. General circulation-model experiments for the

F1. Site location map, p. 22.

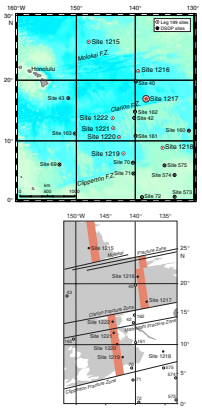

F2. Seismic reflection profile, p. 23.

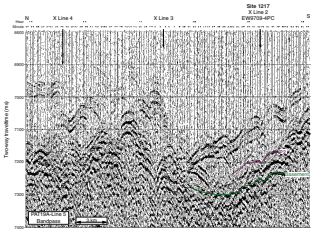

[1] Examples of how to reference the whole or part of this volume.
[2] Shipboard Scientific Party addresses.

Ms 199IR-110

early Eocene (see **Huber,** this volume) suggest that the NECC was a well-developed current during this time period.

Other paleoceanographic and paleoclimatic objectives of drilling the sedimentary sequence anticipated at Site 1217 are as follows: (1) to help define the shift in the Intertropical Convergence Zone through the Paleogene by following the change in eolian dust composition and flux through time (red clays); (2) to help constrain the middle–late Eocene calcite compensation depth (CCD); and (3) to sample the Paleocene/Eocene (P/E) boundary, one of the most climatologically critical intervals of Cenozoic time. Recovery of deep-sea sediments from this time interval during Leg 199 is a high priority because the P/E boundary has never before been sampled in the central tropical Pacific Ocean.

Results from Site 1217 will also provide important information to test whether there was significant motion of the Hawaiian hotspot, with respect to the Earth's spin axis during the early Cenozoic. At 56 Ma, the backtracked location based upon a hotspot reference frame is ~5°N, 106°W, and at 40 Ma is ~8°N, 106°W. If significant hotspot motion or true polar wander occurred since 57 Ma (Petronotis et al., 1994), this drill site could have been much nearer to the equator.

SUMMARY

Site 1217 (16°52.01′N, 138°06.00′W) is situated ~1° north of the Clarion Fracture Zone on abyssal hill topography at a water depth of 5342 m. The site was chosen for drilling because it is thought to have been located just outside of the equatorial region at 56 Ma (~5°N, 106°W based upon a fixed hotspot model; Gripp and Gordon, 1990, for the 0- to 5-Ma Pacific hotspot rotation pole and Engebretson et al., 1985, for older poles). At 40 Ma, the site was located at ~8°N, 111°W. Thus, Site 1217 should help define the paleoceanography of the northern tropical Pacific and, in particular, help to locate the ancient NECC region. Based on site survey seismic data and piston coring together with results from the nearest drill site (DSDP Site 162; situated on 48-Ma crust ~300 km south and west), we expected the sedimentary sequence at Site 1217 to comprise a relatively thick (25–35 m thick) section of red clays overlying a radiolarian ooze. We also expected a basal carbonate section with possible chert near basement (estimated total depth of ~125–150 mbsf) deposited when the site was near the ridge crest in the late Paleocene and early Eocene.

The sedimentary section overlying basalt at Site 1217 is ~138 m thick and records a lower Eocene nannofossil chalk overlain by a poorly recovered lower–middle Eocene chert-clay sequence. Middle Eocene–Holocene deposition is represented by radiolarian ooze followed by red clays at the surface. The recovered sediments from all three holes at Site 1217 were affected by coring disturbance, downhole debris, and flow-in associated with chert fragments blocking the core liner. One stratigraphic interval in the advanced piston corer (APC) cored section was highly disturbed or not recovered in all three holes (~37–49 mbsf), preventing the recovery of a complete continuous sedimentary section. Nevertheless, it was possible to generate a spliced, but discontinuous, record in the upper 90 m of the section.

The uppermost red clays at Site 1217 (Unit I) are ~39 m thick. The clays show an uphole mineralogical transition from smectite rich to illite rich at~7 mbsf, indicating a change in wind-blown dust provenance from American to Asian sources associated with the movement north-

ward of the Pacific plate. The red-clay unit also contains a thin (~2.5 m thick; ~30 mbsf) subunit of nannofossil ooze interbedded with nannofossil clay. Below the red clays are a radiolarian ooze with clay grading to clayey radiolarian ooze (Unit II; ~39–90 mbsf). The radiolarian ooze is of middle Eocene age (~38–43 Ma) and contains rich and well-preserved middle Eocene radiolarian fauna. Below 90 mbsf, we encountered a unit of chert and interbedded clay (90–128 mbsf) before recovering a thin (~1.13 m thick) section of early Eocene chalk (Unit III; 128–129 mbsf). The chalk is partially to extensively dolomitized (washed core catcher samples yield abundant nearly perfect euhedral rhombs ~100 mm in size) but contains nannofossils and planktonic and benthic foraminifers. Basement basalt was encountered at 138 mbsf.

Wet bulk density values at Site 1217 are high between the seafloor and 22 mbsf (mean values = 1.37 g/cm^3) and decrease sharply to a minimum of 1.18 g/cm^3 at 25.58 mbsf, a value that is very similar to the density of the radiolarian oozes at the site. In contrast, the wet bulk densities of the Oligocene nannofossil ooze subunit and lower Paleocene nannofossil chalk are distinctly higher (~1.28 and 1.79 g/cm^3, respectively).

The magnetic intensity of the sediments is relatively strong, and drilling-induced magnetization was mostly removed with mild alternating-field (AF) demagnetization. Site 1217 sediments provided a good record of geomagnetic reversals that could be interpreted as chrons. Characteristic remanent magnetization (ChRM) inclinations are usually shallow, as expected in these latitudes. A record from Chrons C20–C12 was established from the middle Eocene to the early Oligocene, but the reversal stratigraphy in the upper 15 m (late Oligocene–Holocene) could not be established because of the low sedimentation rate of the upper sediments and the lack of either core orientation or an independent age model.

High levels of sulfate and concomitant low levels of ammonium in interstitial pore waters at Site 1217 indicate a relatively oxic system, consistent with very low levels of labile organic matter, occurrences of metalliferous oxides, and the strong and stable magnetic signature within the host sediments. Relatively high pore water silica concentrations are consistent with dissolution of biogenic silica within the sediments. The solid-phase chemical content reflects the microfossil content and the low level of reductive diagenesis. The whole section at Site 1217 shows relatively high levels of Mn and Fe in the solid phase. Within the upper red clays, solid phase Si levels generally increase southward in the Site 1215, 1216, and 1217 transect, presumably indicating higher export of biogenic debris to the ocean floor closer to the paleoequator.

The average linear sedimentation rates (LSRs) in the red clays (shallower than 23 mbsf) are very low (~0.8 m/m.y.). Sedimentation rates in the underlying fossiliferous and cherty lower sections are substantially higher but are, nevertheless, modest (~5 m/m.y.).

Highlights

Lower Oligocene Nannofossil Ooze

Assuming that a distinct normal polarity chron seen in paleomagnetic data at 23.27 mbsf in Hole 1217A represents Chron C12n, the succeeding downhole normal polarity interval is interpreted to represent Chron C13n, which lies at the base of the Oligocene. This interpreta-

tion is consistent with the underlying spacing and length of several normal and reversed intervals and places the thin subunit of nannofossil-rich carbonate ooze (all from nannofossil Zone NP22) in the lowermost Oligocene. This brief interval of carbonate sediment preservation may represent the dramatic deepening of the CCD recorded elsewhere in the deep-sea tropical Pacific Ocean (e.g., DSDP Sites 42, 70, 161, and 162) associated with the Eocene–Oligocene transition, but this possibility can only be validated by shore-based studies.

Middle Eocene Radiolarian Ooze

At Site 1217, we collected the first near-continuously drilled sequence of Eocene radiolarian oozes by deep-sea drilling. In the presence of a well-defined magnetostratigraphy, this section will help to define and calibrate radiolarian stratigraphic zonation. Radiolarian oozes have no modern analog but are prominent sedimentary features of the middle Eocene low-latitude Pacific Ocean having been recovered from piston cores and drill sites up to 4° to the north (e.g., DSDP Sites 40 and 41) and 10° to the south (e.g., DSDP Sites 70 and 162). In contrast, middle Eocene radiolarian oozes are absent at Site 1216. Thus, Sites 1216 and 1217, along with DSDP Sites 40 and 41, appear to define the northern extent of this type of biogenic sedimentation.

Lower–Middle Eocene Chert and Dolomitized Nannofossil Chalk

By coring to basement at Site 1217, we recovered sediments needed to address a number of Leg 199 objectives, including an improvement in our understanding of the following: (1) the location of the P/E paleoequator, (2) the biotic composition and accumulation rate of sediments within the tropical Eocene Pacific Ocean, and (3) the behavior of the silica budget and CCD during the early Eocene. Broadly speaking, the sequence drilled at Site 1217 conforms to the classical sedimentary succession predicted for a deep-sea drill site situated on relatively old oceanic crust in the Central Pacific (red clays overlying siliceous and, in turn, carbonate biogenic sediments). However, the lowermost sediments drilled (lower–middle Eocene chert and chalk) surprised us in two ways. First, these sediments show that average LSRs are relatively slow (<5 m/m.y.), which is consistent with results from Site 1216. Second, the basal lower Eocene chalks that overlie basement are, like their Site 1215 counterparts, dolomitized; an intriguing discovery given their proximity to what is generally considered to be a kinetically more favorable geochemical sink for Mg (alteration minerals in the upper oceanic crust).

OPERATIONS

Transit to Site 1217 (PAT-19A)

The 271-nmi transit to proposed Site PAT-19A was accomplished in 25.2 hr at an average speed of 10.8 kt. At 1700 hr on 8 November, 2001 the vessel slowed to 5 kt, and a short 3.5-kHz survey was made from north to south across the site. Upon conclusion of the 1-hr survey, the vessel came about and returned to site as the thrusters were lowered and the dynamic positioning system was activated. The vessel was on

the Global Positioning System coordinates of the new location by 1815 hr. The hydrophones were lowered, and assembly of the bottom-hole assembly began. A beacon was deployed at 1848 hr. The corrected precision depth recorder (PDR) depth was 5340.9 meters below rig floor (mbrf).

Hole 1217A

After the drill string was deployed to a depth of 5330 mbrf, an APC-mudline core was attempted from 5335.9 mbrf and resulted in a water core. The driller then lowered the bit until the heave compensator appeared to activate, suggesting contact with a firm sea bottom at a bit depth of ~5353 mbrf. The second attempt at a mudline core was made with the bit at 5349.0 mbrf and was successful (0630 hr on 9 November). The seafloor depth indicated by the recovery of this first core was 5353.0 mbrf and was 12.1 m deeper than the PDR depth.

Hole 1217A was deepened to 99.2 mbsf before it was deemed necessary to switch to the extended core barrel (XCB) to achieve the objective of obtaining a sample of basement (Table T1). Two of the twelve APC cores (Cores 6H and 8H) did not achieve a full 9.5-m stroke, presumably the result of striking chert. Many of the fully advanced cores also experienced lateral suctioning (flow-in) of sediment below recovered chert nodules. The cores were oriented starting with Core 3H. No heat flow measurements were attempted because of the high probability of damage to the Adara cutting shoe by chert. Hole 1217A APC operations resulted in 99.2 m of cored section with 86.17 m of material recovered (86.9%).

T1. Coring summary, p. 47.

XCB coring (Cores 13X–17X) deepened the hole from 99.2 to 145.2 mbsf, with recovery consisting of chert fragments and a section of nannofossil chalk near basement. A small sample of basalt was obtained in the last core. XCB coring operations deepened Hole 1217A 46.0 m beyond the APC operations and recovered 3.77 m (8.2%). The total recovery for Hole 1217A was 89.94 m, representing 61.9% of the cored interval.

Hole 1217B

After the bit cleared the seafloor, the vessel was offset 10 m north of Hole 1217A. The bit was washed to 20 mbsf before we initiated APC operations. Hole 1217B was spudded with the APC at 1545 hr on 10 November. Seven piston cores were obtained over the interval from 20.0 to 86.5 mbsf (Table T1). Many of the cores had flow-in or disturbance below recovered chert nodules. All cores from Hole 1217B were oriented. The average recovery was 92.5%.

Hole 1217C

After coring operations in Hole 1217 ceased, the bit was pulled clear of the seafloor, the vessel was moved another 10 m north, and Hole 1217C was spudded at 0630 hr on 11 November. The bit was washed to 32 mbsf, where APC coring operations began. Five oriented cores were taken over the interval from 32.0 to 79.5 mbsf (Table T1). The average recovery was 98.6%, but many cores suffered from flow-in.

After coring operations ceased at Site 1217, the drilling equipment was secured, and the beacon was successfully recovered. The 24-hr transit to the next site (PAT-8) began at 1545 hr on 12 November.

LITHOSTRATIGRAPHY

At Site 1217, we recovered a 145-m section dominated by pelagic clay, radiolarian ooze, chert, and nannofossil chalk (Fig. F3). Fifty-two meters of middle Eocene–Holocene pelagic clay overlies 80 m of middle Eocene radiolarian clay and chert and 1.1 m of nannofossil chalk. Thirty centimeters of basalt were also recovered at the base of this site.

Three holes were drilled at Site 1217. Recovery in Hole 1217B and Hole 1217C began at 20 and 32 mbsf, respectively. The sedimentary section is divided into four lithologic units on the basis of sedimentary facies. Drilling of Holes 1217B and 1217C was terminated above the chert horizon (Subunit IIB); therefore, this description is largely based on results from Hole 1217A. Lithologic Unit I, Subunit IIA, and Unit III are disturbed by drilling and chert in the upper few centimeters of most cores. Chert in Subunit IIB created numerous flow-ins and other disturbances, resulting in poor recovery throughout this interval.

Unit I

Intervals: 199-1217A-1H, 0 cm, through 7H-1, 140 cm; 199-1217B-2H, 0 cm, through 3H-CC; and 199-1217C-2H, 0 cm, through 3H-CC
Depths: 0–52 mbsf (Hole 1217A); 20–39 mbsf (Hole 1217B); and 32–51 mbsf (Hole 1217C)
Age: Holocene to middle Eocene
Lithology: clay and nannofossil ooze with clay

The sediments of Unit I vary between dark yellowish brown (10YR 4/6) and very dark brown (7.5YR 2.5/2) clay. Zeolitic clay and clay with zeolites are present throughout Unit I, with zeolite and iron oxide content increasing downcore. Sediments are commonly mottled, with bioturbation ranging from slight to moderate. Flow-in occurs within Unit I in Cores 199-1217A-5H (38–43 mbsf) and 199-1217C-3H (45–51 mbsf).

Manganese nodules are present at the top of Hole 1217A. The first downhole appearance of chert occurs in Sections 199-1217A-5H-3, 56 cm; 199-1217B-3H-6, 90 cm; and 199-1217C-3H-2, 116 cm. Below this horizon, black (N1) and brownish black (5YR 2/2) centimeter-sized fragmented chert nodules result in core disturbance. A vitric ash layer is present at Section 199-1217B-3H-3, 96 cm. The distinctive dark yellowish brown (10YR 4/4) to very dark brown (10YR 2/2) color change observed at Site 1215, thought to represent a change in the eolian dust source from China to North America (see "Lithostratigraphy," p. 4, in the "Site 1215" chapter), was not observed at Site 1217.

Within Unit I is a lower Oligocene dark yellowish brown (10YR 4/4) nannofossil ooze with clay (intervals 199-1217A-4H-2, 36 cm, to 4H-6, 118 cm; 199-1217B-2H-5, 41 cm, to 2H-CC, 10 cm) and not recovered in Hole 1217C. This interval shows heavy bioturbation/mottling. The upper boundary between the nannofossil ooze and the overlying clay is gradational. At the lower contact of the nannofossil ooze in Hole 1217A, there is a prominent (4 cm thick) light gray (10YR 7/1) vitric ash layer (Fig. F4) (interval 199-1217A-4H-6, 50–54 cm) not represented in Hole 1217B. This ash layer has a bioturbated upper contact with the nannofossil ooze and a sharp basal contact with clay. An ash layer was also observed within the nannofossil ooze in Samples 199-1217A-4H-4, 14–15 cm, and 199-1217B-2H-CC.

F3. Lithologic summary, p. 24.

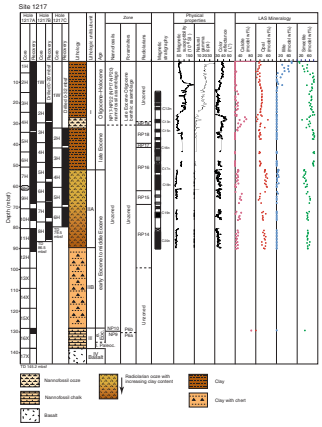

F4. Unit I ash layer within nannofossil ooze, p. 25.

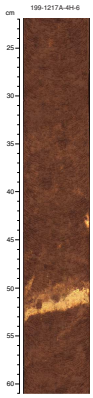

Unit II

Intervals: 199-1217A-7H-1, 140 cm, through Core 15X; 199-1217B-4H, 0 cm, through 8H-CC; and 199-1217C-3H, 0 cm, through 6H-CC
Depths: 52–128 mbsf (Hole 1217A); 39–87 mbsf (Hole 1217B); and 51–80 mbsf (Hole 1217C)
Age: middle to early Eocene
Lithology: radiolarian ooze with clay, clayey radiolarian ooze, chert, and clay

Unit II is divided into two subunits based upon the lithological components. The base of Subunit IIA was only recovered in Hole 1217A.

Subunit IIA

Intervals: 199-1217A-7H-1, 140 cm, through 11H-CC; 199-1217B-4H-1, 0 cm, through 8H-CC; and 199-1217C-3H-1, 0 cm, through 6H-CC
Depths: 52–90 mbsf (Hole 1217A); 39–87 mbsf (Hole 1217B); and 51–80 mbsf (Hole 1217C)
Age: middle Eocene
Lithology: radiolarian ooze with clay and clayey radiolarian ooze

Subunit IIA is composed primarily of a very dark brown (7.5YR 2.5/3) radiolarian ooze with clay. Clay content increases downhole, and the lithology grades into a dark brown (7.5YR 3/4) clayey radiolarian ooze in Sections 199-1217A-7H-6, 120 cm, and 199-1217B-7H-2, 30 cm. The ooze is commonly mottled by brownish yellow (10YR 6/8) markings that denote undifferentiated burrows. The upper contact with the Unit I clay is gradational. As in Unit 1, black (N1) chert nodules and fragments result in core disturbance in some intervals. Traces of oxides are present throughout Subunit IIA. A 2-cm-thick, very pale brown (10YR 8/3) vitric ash layer is present in interval 199-1217B-6H-3, 74–76 cm. Centimeter-scale oscillations of strong brown (7.5YR 4/6), dark reddish brown (5YR 3/4), and dark-brown (7.5YR 3/4) banding are present within Cores 199-1217B-6H and 199-1217C-5H and are also represented in the color reflectance data (see **"Composite Depths,"** p. 13). However, no significant changes in clay or radiolarian content could be distinguished through smear slide examination.

Notable accessories include a medium gray (N5) 3-cm-sized pumice pebble in interval 199-1217B-8H-3, 135–138 cm (Fig. **F5**). A thin section of the pumice indicates a glassy, amorphous structure with accessory minerals including plagioclase. Several voids in the thin section contained radiolarian tests and fragments; one species was tentatively identified as *Siphocampe acephala* (Eocene).

F5. Pumice pebble in Subunit IIA, p. 26.

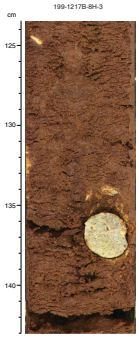

Subunit IIB

Interval: Cores 199-1217A-12H through 15X
Depth: 90–128 mbsf (Hole 1217A)
Age: middle to early Eocene
Lithology: chert and clay

Subunit IIB is differentiated from Subunit IIA by the predominance of chert. Cores 199-1217A-12H to 15X are highly disturbed by the presence

of chert, which resulted in poor recovery. The chert is commonly black (N1) and broken into pebble-sized fragments by the drilling process. Angular pebbles and massive chert are present within a dark-brown (7.5YR 3/2) clay slurry. Massive chert in Core 199-1217A-14X showed black (N1) and brownish black (5YR 2/2) banding. The clay is not in situ because of drilling disturbance and in many instances is completely removed.

Unit III

Interval: Section 199-1217A-16X-1, 0 cm, through 16X-2, 20 cm
Depth: 128–129 mbsf (Hole 1217A)
Age: early Eocene
Lithology: nannofossil chalk with clay and dolomite

Beneath the chert horizons, we recovered a thin (1.13-m-thick) very pale brown (10YR 8/3) nannofossil chalk with clay and dolomite that is intercalated with 3- to 6-cm-thick beds of a very dark brown (7.5YR 2.5/2) nannofossil claystone with dolomite and light-gray (10YR 7/2) nannofossil chalk (Fig. F6A). The dolomite crystals are clear, near-perfect rhombs (Fig. F6B). The nature of the contact with the overlying chert and clay is unknown because of poor recovery. The interval is heavily mottled.

F6. Nannofossil chalk and dolomite rhombs, p. 27.

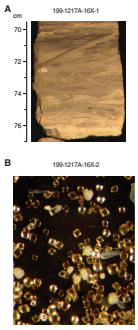

Unit IV

Interval: Core 199-1217A-17X
Depth: 129–138 mbsf (Hole 1217A)
Age: late Paleocene
Lithology: basalt

Core 199-1217A-17X contains a fine-grained, weathered, ocean-floor basalt with aphanitic texture. Rock fragments are composed of elongate white plagioclase and black pyroxene crystals and black glass. Clay was present with nannofossils, which indicates a late Paleocene age (NP9).

Discussion/Summary

The sedimentary section at Site 1217 records lower Eocene nannofossil chalk overlain by lower–middle Eocene chert. Middle Eocene–Holocene deposition is represented by the overlying clay and radiolarian-ooze lithologies. Radiolarian biostratigraphy indicates that the radiolarian-ooze lithology represents ~8 m.y. of deposition; unlike modern siliceous sediments, this ooze is dominated entirely by radiolarians, not diatoms.

The lower Oligocene nannofossil ooze within Cores 199-1217A-4H and 199-1217B-2H is similar to the nannofossil ooze and chalk recovered at DSDP Site 162 (Fig. F7) (van Andel et al., 1975). Paleodepth calculations suggest seafloor depths >4 km at Site 1217, which helps to constrain the depth of the Oligocene CCD at this time (see Fig. F12, p. 63, in the "Leg 199 Summary" chapter).

F7. Carbonate data, DSDP Site 162, p. 28.

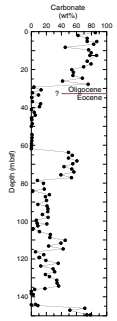

BIOSTRATIGRAPHY

The red clays and radiolarian clays of Site 1217 are mostly barren of calcareous microfossils with the exception of a few short intervals (Fig. F8). The fossil content of the upper part of the sediment sequence is limited to ichthyoliths and occasional concentrations of agglutinated benthic foraminifers. The underlying radiolarian clays, whose top is at ~26.3 mbsf in Section 199-1217A-4H-2, contain radiolarian assemblages indicative of a late Eocene–middle Eocene age (RP18 to RP14). A late Eocene–middle Eocene age for the top of the radiolarian clay sequence is supported by a few samples containing calcareous nannofossils and calcareous benthic foraminifers. A 1.13-m-thick sequence of nannofossil chalk in Core 199-1217A-16X (128.1–129.2 mbsf) contains a diverse and moderately well preserved assemblage of nannofossils, planktonic foraminifers, and benthic foraminifers representative of lower Eocene Zones NP9 and NP10 and Subzone P6a. The presence of rare, poorly preserved benthic foraminifers typical of the late Paleocene in Core 199-1217A-17X suggests that the site may have drilled through the P/E boundary. However, the presence of lower Eocene nannofossils in these same samples raises the possibility that the benthic foraminifers have been reworked from older strata.

F8. Distribution of biostratigraphic zones for radiolarians, p. 29.

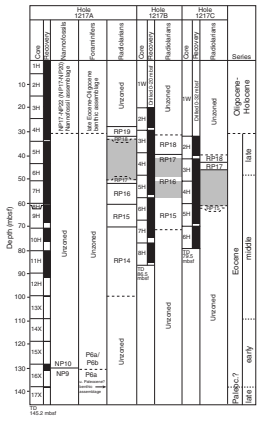

Calcareous Nannofossils

Red-clay and chert facies barren of nannofossils characterize all core catcher samples except for Sample 199-1217A-17X-CC, containing a P/E boundary assemblage from Zone NP9. This core catcher sample also contains basalt. The first downhole occurrence of nannofossils was observed in a short interval in Sections 199-1217A-4H-2 through 4H-4, indicating a brief interval of carbonate preservation interrupting the red-clay facies. Five samples were investigated from this carbonate-bearing sediment and all showed severe calcite dissolution.

The best-preserved sample was observed in Section 199-1217A-4H-4, 10 cm, and includes the following species: abundant *Dictyococcites bisectus, Dictyococcites hesslandii, Reticulofenestra dictyoda,* common *Discoaster deflandrei, Discoaster tanii, Sphenolithus moriformis,* and rare *Reticulofenestra umbilicus* ≥14 µm, *Coccolithus pelagicus, Sphenolithus predistentus,* and *Sphenolithus tribulosus.* Many isolated nonbirefringent placolith shields were observed, which are probably distal shields of *C. pelagicus*. A 2-cm-thick whitish layer in red clays from Section 199-1217A-4H-6 contained a similar nannofossil assemblage, although only rare *D. tanii* was observed in this layer.

The presence of rare *R. umbilicus* and *S. tribulosus,* with abundant *D. bisectus* and the absence of both Eocene rosette-shaped discoasters and *Ericsonia formosa,* suggests that Sections 199-1217A-4H-4 through 4H-6 belong to Zone NP22 of the lower Oligocene (Chron C12r).

Section 199-1217A-16X-1 and upper Section 16X-2 contains a mottled carbonate chalk unit belonging to Zones NP10 and NP9. A dissolved but otherwise indigenous lower Eocene assemblage characterizes Sample 199-1217A-16X-1, 6 cm, with common *Tribrachiatus contortus,* indicating Zone NP10. Calcite overgrowth complicates accurate identification of the evolutionary transitions in the *Rhombaster-Tribrachiatus* lineage. Yet *Tribrachiatus bramlettei* was observed from Sample 199-1217A-16X-1, 24 cm, to Sample 16X-1, 78 cm (NP10). The next deeper

sample (16X-1, 103 cm) contains abundant *Rhomboaster cuspis,* and *T. bramlettei* is absent indicating upper Zone NP9.

Small chalk pockets embedded in a piece of chert (Sample 199-1217A-16X-2, 73 cm) contain common *Discoaster multiradiatus* and *R. cuspis* among a dissolved, indigenous lower Eocene assemblage lacking *Fasciculithus* spp., which indicates upper Zone NP9.

Core 199-1217A-17X only had recovery in the core catcher (pieces of basalt and some clay), which yielded a corroded assemblage with common to abundant *D. multiradiatus* and *Fasciculithus tympaniformis* indicating lower Zone NP9 of the uppermost Paleocene. Other species observed belong to the genera *Chiasmolithus, Coccolithus, Cruciplacolithus, Prinsius, Sphenolithus,* and *Toweius*.

Planktonic Foraminifers

Sediments from Site 1217 are barren of planktonic foraminifers except for the burrow-mottled chalk recovered in Core 199-1217A-16X. Preservation of foraminifers is highly variable through this section. Samples 199-1217A-16X-1, 27–29 cm, and 16X-1, 74–75 cm, contain heavily dissolved assemblages in which only the more resistant species remain. A few degraded specimens of *Morozovella subbotinae, Morozovella gracilis, Morozovella aquea, Acarinina soldadoensis,* and *Acarinina coalingensis* in these samples indicate an early Eocene (Subzones P6a and P6b) age. Preservation is very poor in Sample 199-1217A-16X-1, 105–107 cm, and no age diagnostic species are identifiable. Preservation improves slightly downcore, and Sample 199-1217A-16X-2, 19–21 cm, contains a reasonably diverse assemblage of early Eocene planktonic foraminifers of a typically tropical nature. Specimens are common and poorly to moderately well preserved. Based on the occurrence of *Morozovella marginodentata, M. gracilis, M. subbotinae,* and *M. aquea* and in the absence of Subzone P6b marker *M. formosa* and the Paleocene Zone P5 marker *Morozovella velascoensis,* we place this sample in lower Eocene Subzone P6a. The sample also contains *A. soldadoensis, Acarinina wilcoxensis, Globanomalina pseudoimitata, Subbotina patagonica, Parasubbotina varianta,* and the small unidentified species reported at Site 1215 (cf. *Tenuitella*? sp).

Benthic Foraminifers

Benthic foraminifers are largely absent from the red clay and radiolarian ooze and are present only occasionally at certain intervals in the recovered sections from Site 1217. When present, benthic foraminifers are composed of either agglutinated or calcareous assemblages. The agglutinated assemblages show low diversity, are poorly preserved, and of little stratigraphic use. In contrast, calcareous foraminiferal assemblages are well preserved and relatively diverse, but such assemblages are limited in stratigraphic occurrence. Samples 199-1217A-1H-CC through 3H-CC; 7H-CC through 11H-CC; 12H-1, 0–5 cm; 15X-1, 29–30 cm, and core catchers between Samples 199-1217B-5H-CC and 8H-CC are barren of benthic foraminifers. The distribution of benthic foraminifers is reported in Table **T2.**

Well preserved assemblages of benthic foraminifers are found in Samples 199-1217A-4H-2, 114–116 cm; 4H-3, 27–29 cm; 4H-4, 10–12 cm; and 4H-6, 51–53 cm. Of these, the assemblage in Sample 199-1217A-4H-2, 114–116 cm, shows the greatest diversity. The most common species are *Globocassidulina* sp., *Nuttallides umbonifer, Gyroidinoides*

T2. Distribution of benthic foraminifers, p. 49.

spp., and large specimens of *Cibicidoides grimsdalei* and *Cibicidoides havanensis,* which indicate lower bathyal to abyssal depths (van Morkhoven et al., 1986). The latter two species range from the lower Eocene to the Miocene but are typically most abundant in Eocene–Oligocene deep-sea sediments (van Morkhoven et al., 1986). *N. umbonifer* is a common species in the deep sea after the extinction of *Nuttallides truempyi* and has its last occurrence in the uppermost Eocene (Zone P17; Berggren and Miller, 1989). However, *N. truempyi* more commonly disappears near the middle/upper Eocene boundary (planktonic foraminiferal Zone P15) at abyssal depths (Berggren and Miller, 1989). Assemblages that contain *N. umbonifer* in the absence of *N. truempyi* have also been recognized in bathyal late Eocene sediments (Nomura, 1995). Based on this information, the assemblage of Sample 199-1217A-4H-2, 114–116 cm, can be assigned to a late Eocene or younger age.

Samples 199-1217A-16X-2, 19–20 cm, and 17X-CC contain calcareous foraminifers such as *N. truempyi, Anomalinoides spissiformis, Bulimina semicostata, Globocassidulina globosa,* and *Abyssamina poagi*. Planktonic foraminifers are also present and nearly in equal abundance to the benthic assemblage with a planktonic:benthic ratio of 1.2:1. *Gavelinella beccariiformis, Aragonina velascoensis, Pullenia coryelli,* and *Gyroidinoides globosus,* all of which belong to the Velasco-type foraminifers (van Morkhoven et al., 1986), are rare in Sample 199-1217A-17X-CC. However, they are badly preserved and may be reworked from older sediment. Foraminifer assemblages in these two samples are dominated by *N. truempyi* and *A. poagi,* and they account for 50% of the total assemblage of Sample 199-1217A-16X-2, 19–20 cm, and 69% of Sample 199-1217A-17X-CC. The high abundance of these two species suggests that these assemblages belong to the early Eocene.

Radiolarians

The upper red clay (Unit I) of Hole 1217A contains rare to few, poorly preserved radiolarians from Sample 199-1217A-1H-CC to 6H-6, 45–47 cm. Samples 199-1217A-4H-5, 45–47 cm, and 4H-6, 45–47 cm, probably belong to Zone RP19, although the presence of reworked specimens of *Thyrsocyrtis triacantha* and *Eucrytidium fistuligerum* cast some doubt on the zonal designation. The first occurrence of *Cryptocarpium azyx* in Sample 199-1217A-6H-CC places this sample in Zone RP17, but the faunal assemblage between that sample and the Zone RP19 samples is too poor to allow placement of the RP17/RP18 boundary. These samples were particularly difficult to disaggregate, and the clay content could not be completely eliminated. All subsequent downhole samples contain a rich, well preserved middle Eocene radiolarian fauna. Samples 199-1217A-7H-2, 45–47 cm, through 1217A-7H-CC belong to Zone RP16. At Section 199-1217A-7H-6, ~134–138 cm, there is a band of pure radiolarian ooze. Samples 199-1217A-8H-CC through 9H-CC fall within Zone RP15. The boundary between Zones RP15 and RP14 is defined as the evolution from *Podocyrtis mitra* to *Podocyrtis chalara* but is placed here at the first occurrence of *P. chalara*. Using this definition, the remainder of the studied interval down to Sample 199-1217A-12H-1, 1–5 cm, belongs to Zone RP14.

Sampling from Holes 1217B and 1217C was designed to capture the intervals missed during coring of Hole 1217A. In Hole 1217B, Samples 199-1217B-2H-4, 110–112 cm, and 3H-6, 134–136 cm, contained an impoverished fauna lacking age-diagnostic taxa. The rest of the samples studied contain a common to abundant and well-preserved assemblage.

Samples 199-1217B-3H-2, 32–34 cm; 3H-3, 84–86 cm; and 4H-1, 50–52 cm, belong to Zone RP18. Samples 199-1217B-4H-1, 140–142 cm, and 4H-2, 50–52 cm, are assigned to Zone RP17; Samples 199-1217B-5H-1, 80–82 cm, and 5H-2, 80–82 cm, to Zone RP16; and the remaining samples down to 199-1217B-7H-2, 130–132 cm, fall within Zone RP14.

Four samples were taken from Hole 1217C. The uppermost material from Sample 199-1217C-3H-1, 60–62 cm, contains a moderately well preserved, but somewhat sparse, fauna belonging to Zone RP18. The next sample (199-1217C-3H-2, 10–12 cm) belongs to the same zone but contains a much richer assemblage. Sample 199-1217C-3H-2, 98–100 cm, falls within Zone RP17, and Sample 5H-1, 120–122 cm, falls within Zone RP15.

PALEOMAGNETISM

All archive-half core sections from Holes 1217A, 1217B, and 1217C were measured on the shipboard pass-through cryogenic magnetometer. A total of 134 core sections were measured from the 24 cores recovered in the 3 holes. The natural remanent magnetization (NRM) was measured at 5-cm intervals in each core section, followed by four to five steps of AF demagnetization up to a maximum peak field of 20 mT. For sections with clearly disturbed sediment, a blanket demagnetization at 15 mT was applied, but the directions were not used for establishing the magnetostratigraphy. In addition, 10 discrete samples were taken from Hole 1217A cores to carry out more detailed progressive demagnetization. As at Site 1216, several of the measured cores are in poor condition mostly because of drilling disturbance.

NRM magnetization intensities were in the order of 10^{-2} to 10^{-1} A/m and decreased to about 10^{-3} to 10^{-2} A/m after partial AF demagnetization (Fig. F9). Magnetization intensity for the basal sedimentary unit (the nannofossil chalk at 128–129 mbsf) is slightly lower than in overlying Units I and II but still above the noise level of the cryogenic magnetometer. Also, a chert interval from Core 199-1217A-14H at ~108 mbsf was measured and gave a reliable paleomagnetic signature. A large group of NRM inclinations showed steep downward directions (~70°), indicative of a drilling-induced overprint. This overprint was mostly removed with AF demagnetization, typically disappearing by the 10- to 15-mT demagnetization step. Some magnetic directions did not reach a stable point between 5 and 20 mT, suggesting that the ChRM has been only partially isolated.

F9. Magnetization intensities after AF demagnetization, p. 30.

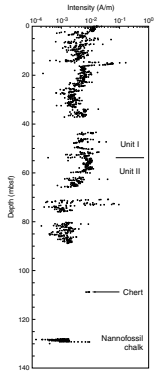

Orientation

The Tensor tool was used to orient APC cores in Hole 1217A, starting with Core 199-1217A-3H, whereas all cores were oriented in Holes 1217B and 1217C. Although the Tensor tool provided a good first-order orientation for most cores, some of them needed to be reoriented by an additional vertical rotation. Reorientation assumes that no tectonic rotation has occurred, which seems very reasonable in this area and is based on the analysis of the paleomagnetic directions. The mean magnetization direction computed for each core was restored to the north direction and all individual magnetization directions were rotated by the same amount. This was straightforward for all cores except for Core 199-1217A-9H, where the correct declination could not be established

unambiguously. For this reason, the magnetic polarity from 61.95 to 66.04 mbsf in Hole 1217A must be treated with caution.

Discrete Sample Analysis

Oriented discrete samples (8-cm³ cubic plastic boxes) from Core 199-1217A-7H were thoroughly AF demagnetized up to 80 mT to examine the stability of the remanent magnetization and compute a more faithful ChRM direction using vector analysis instead of blanket demagnetization. Results are of good quality (Fig. F10) and provide our most reliable estimate of the paleolatitude at this site and for an age corresponding to Chron C18n (38–40 Ma). The average ChRM inclination for this set of 10 samples is 17.2°, corresponding to a paleolatitude of 8.2°N (upper/lower bounds are 9.5° and 6.8°, respectively).

F10. AF demagnetization of a discrete sample, p. 31.

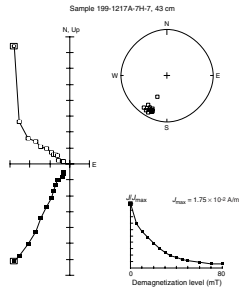

Magnetic Polarity Stratigraphy

Except for sections that had to be discarded because of excessive drilling disturbance, Site 1217 provided a good record of geomagnetic reversals that could be easily interpreted as magnetozones (Table T3). ChRM inclinations are usually shallow, as expected in these latitudes, and a few cores gave a particularly good set of ChRMs (e.g., Core 199-1217A-7H) that passed a reversal test, which suggests that they represent a clean record of the geomagnetic field. The directions from Core 199-1217A-7H gave average declination and inclination values of 32.15° and 22°, respectively, which are rather similar to those obtained from discrete samples. The inclination in the top 15 m of Hole 1217A cannot be unambiguously interpreted, probably because these sediments had a very low accumulation rate from Oligocene to the Quaternary time. The magnetostratigraphy of Site 1217 (Fig. F11) results from a composite of the virtual geomagnetic pole latitudes of Holes 1217A, 1217B, and 1217C that were spliced via the composite depth scale (see "Composite Depths," p. 13). We identify, from bottom to top, Chron C20n followed by Chron C19r, which is only partially resolved because of sediment disturbance. Upward in the section, Chrons C18n–C12n have also been identified. The magnetic ages are corroborated by the radiolarian zones found in the middle and upper parts of the section (see "Radiolarians," p. 11, in "Biostratigraphy"). Flow-in in cores 199-1217A-5H and 6H prevented the clear identification of Chrons C16 and C17, at ~40–45 mcd. Overall, the composite stratigraphic section between 14 and 90 mcd spans ~13 m.y., or from the middle Eocene to the early Oligocene.

T3. Composite depths of geomagnetic reversals, p. 50.

F11. Composite magnetic stratigraphy, p. 32.

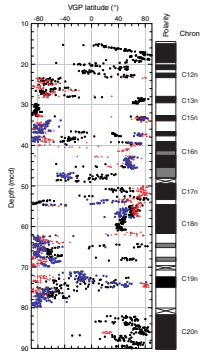

COMPOSITE DEPTHS

The recovered sediments from all three holes at Site 1217 were seriously affected by coring disturbance, downhole debris, and flow-in associated with chert fragments blocking the core liner. In addition to this general coring disturbance throughout the cored interval, one stratigraphic interval was highly disturbed or not recovered in all three holes (~37–49 mbsf), thus preventing the recovery of a complete continuous sedimentary section. Nevertheless, it was possible to generate a spliced, but discontinuous, record in the upper 90 m of the section. Below 90 mbsf (Cores 199-1217A-12H through 15H; 89.70–129.66 mbsf), there was negligible recovery because of difficult drilling conditions as-

sociated with an extensive (~40 m thick) chert-rich interval. Approximately 1.5 m of good-quality quasicyclical claystone and chalk were recovered in Core 199-1217A-16X (129.66–137.70 mbsf), but this interval is omitted from further discussion because it was not cored in Holes 1217B and 1217C and is too stratigraphically removed from the shallower intervals.

Multisensor track (MST) and color reflectance data were collected from Holes 1217A, 1217B, and 1217C. Magnetic susceptibility (MS), *P*-wave velocity, and color reflectance data were collected at 2-cm intervals and gamma ray attenuation (GRA) bulk density data at 4-cm intervals on all core sections recovered from Holes 1217A to 1217C that were not entirely filled by chert fragments (see **"Physical Properties,"** p. 18 and **"Lithostratigraphy,"** p. 6, for details about MST and color reflectance data). Table **T4** lists intervals from Holes 1217A to 1217C that are interpreted to be disturbed and are excluded from further discussion.

Figure **F12** illustrates the MST and color reflectance data from Site 1217 on the mbsf depth scale, after culling MST data from the disturbed intervals listed in Table **T4.** The interhole correlation of the upper ~40 mbsf is straightforward as the result of a strong and clear variation of MS data as well as a clear decreasing pattern in the natural gamma ray (NGR) data that was also observed at Sites 1215 and 1216. Coring in Holes 1217B and 1217C began below 20 mbsf; thus, no data are available from these holes to aid in composite-depth construction in the upper 20 mbsf. Therefore, no depth adjustment was made to Cores 199-1217A-1H, 2H, and 3H.

A continuous composite record can be constructed from the top of Core 199-1217A-3H (15.00 mbsf; 15.00 meters composite depth [mcd]) down to the base of Core 199-1217B-3H (39.00 mbsf; 41.50 mcd), which corresponds to the middle of Core 199-1217A-5H (a disturbed interval in Hole 1217A). Figure **F13** shows the MST and color reflectance data after adjusting to a common depth scale, and Table **T5** lists the offsets that were applied to the top of each core. Below 42 mcd (Core 199-1217B-3H), several cores can be placed into a composite depth framework (i.e., correlated to each other), but a continuous section cannot be constructed and it was not always possible to establish the true stratigraphic position of cores. For example, data from Cores 199-1217B-4H and 199-1217C-3H can be correlated to each other. In Figure **F13,** this interval is plotted between ~42.5 and 45.8 mcd, but the position of these cores is not constrained with respect to Hole 1217A or the other intervals above or below in any of the holes. This uncertainty also applies to the relative position of other core segments below 49 mcd (Core 199-1217A-6H).

With the understanding that the composite depth scale aligns features within continuously cored segments but does not represent the relative sediment thickness across unconstrained intervals, one can construct a partially spliced record as defined by the splice table (Table **T6**) and shown in Figure **F14.** The interhole correlation developed here is consistent with radiolarian biostratigraphic datums (see **"Biostratigraphy,"** p. 9) and paleomagnetic data (see **"Paleomagnetism,"** p. 12).

SEDIMENTATION AND ACCUMULATION RATES

Average LSRs at Site 1217 are based primarily on paleomagnetic reversals and nannofossil and radiolarian datums as defined in Holes

T4. Core disturbance intervals, p. 51.

F12. GRA bulk density, magnetic susceptibility, color reflectance (L*), *P*-wave velocity, and natural gamma count data plotted vs. depth, p. 33.

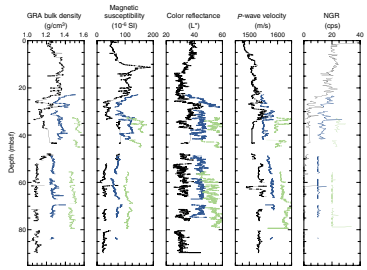

F13. GRA bulk density, magnetic susceptibility, color reflectance (L*), *P*-wave velocity, and natural gamma count data plotted vs. composite depth, p. 34.

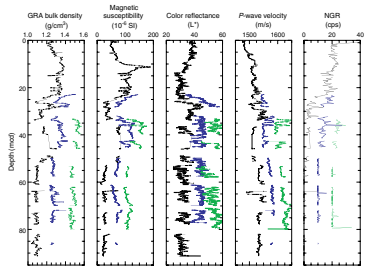

T5. Composite depth offsets, p. 52.

T6. Splice tie points, p. 53.

F14. Spliced records of GRA bulk density, magnetic susceptibility, color reflectance (L*), *P*-wave velocity, and natural gamma count data plotted vs. composite depth, p. 35.

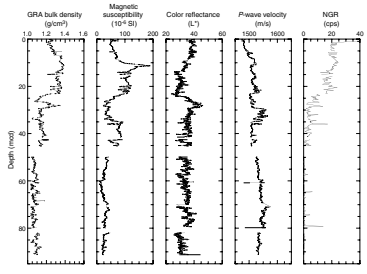

1217A through 1217C (Tables T7, T8). A few nannofossil datums are critical to determining the age at the base of the section. Radiolarian datums are not sufficiently well tied to the paleomagnetic timescale to allow their use in this part of the section. LSRs are calculated using the mcd scale (see "Composite Depths," p. 13) (Table T4) for each datum used in constructing the sedimentation rate plots (Figs. F15, F16). The values of these sedimentation rates are combined with the dry bulk density (DBD) data from porosity measurements on individual samples averaged over the intervals reported (see "Physical Properties," p. 18) (Table T13) to determine the mass accumulation rates (MARs) of the sediments.

Density measurements on piston core EW9709-4P, taken in the site survey area, show a good similarity with density measurements from the spliced density record measured in cores from Site 1217 (Fig. F16). The EW9709-4P record spans a similar depth range in Site 1217 (down to ~14 m); however, there are no biostratigraphic or paleomagnetic datums that constrain this correlation.

From ~20 to 80 mbsf, the paleomagnetic data (see "Paleomagnetism," p. 12) (Fig. F11) show several distinct reversals. The uppermost distinct reversal (at 23.27 mbsf) in Hole 1217A is taken to be the base of Chron 12n. If we accept this point as the shallowest age control below the seafloor, we estimate the average LSR of the nonfossiliferous pelagic clays to be ~0.76 m/m.y. (Fig. F15). The interpretation for the base of Chron 12n leads to the identification of the next deeper normal interval in Hole 1217A as Chron13n, which lies at the base of the Oligocene. This identification fits with the underlying spacing and length of several normal and reversed interval and with the thin part of the lithologic Unit I containing a layer of nannofossil-rich carbonate ooze (see "Lithostratigraphy," p. 6). This ooze, all from nannofossil Zone NP22, we take to represent the dramatic deepening of the CCD at the Eocene–Oligocene transition (see "Biostratigraphy," p. 9).

Using identifications of the magnetic reversals, sedimentation rates in the clay underlying the carbonate are ~3.3 m/m.y., increasing to ~4.4 m/m.y. downhole as the more radiolarian-rich sediments of lithologic Unit II are encountered downcore (Fig. F17). In the lower part of the more well-dated section (~60–80 mcd), sedimentation rates appear to increase to 10 m/m.y. (Fig. F17). However, sedimentation rate estimates for this rather short interval are subject to substantial errors arising from even a small error in age or depth estimates. The overall LSR estimate for fossiliferous and cherty lower section of lithologic Units II and III is 4.8 m/m.y. (Fig. F15).

By combining LSR values with DBD, we determine the MAR of the total sediment (Table T9) and, when appropriate geochemical concentration data are available, the MAR of each sedimentary component. Sediment with an LSR of 1.0 cm/k.y. and a DBD of 1.0 g/cm^3 will have a MAR value of 1.0 g/cm^2/k.y. The observed values are rarely this high, so we report the data in milligrams per centimeter squared per thousand years (mg/cm^2/k.y.). The accuracy of this calculation is ±10%–20%.

Lithologic Unit I (pelagic clays) is characterized by LSR and MAR values that increase downhole: LSR from 0.76 m/m.y. in the upper 22.5 m (Fig. F15) to 4.4 m/m.y. in the interval just above 52 mcd (Fig. F17). Because of downhole increases in DBD, the total mass flux increase from 45 mg/cm^2/k.y. (in the age range 0–31 Ma) progressively to 150 mg/cm^2/k.y. (between 35 and 38 Ma) (Figs. F15, F17). This is the first record clearly showing clay fluxes that increase downhole. Prior records indicate downcore decreases in the MAR of the red clays during middle

T7. Paleomagnetic datums, p. 54.

T8. Nannofossil and radiolarian events, p. 55.

F15. Plot of biostratigraphic and paleomagnetic datum levels used to constrain average LSR vs. depth, p. 36.

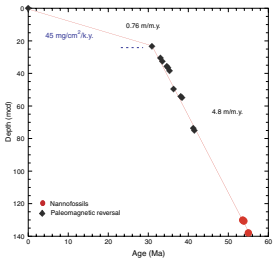

F16. Core EW9709-4P density compared with Site 1217 GRA density, p. 37.

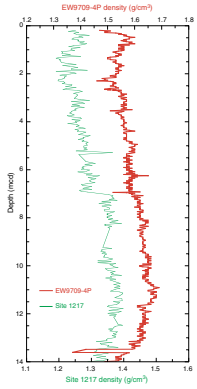

F17. Plot of all biostratigraphic and paleomagnetic datum levels, p. 38.

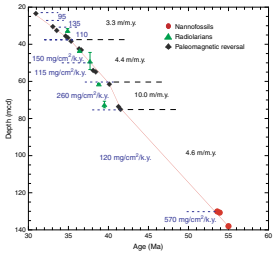

T9. Linear sedimentation rates and mass accumulation rates for the major lithologic units, p. 56.

Cenozoic time (Janecek and Rea, 1983; Kyte et al., 1993; J.D. Gleason et al., unpubl. data). The clayey carbonate ooze that occurs within Unit I has a MAR value of 135 mg/cm²/k.y. (Fig. F17).

The radiolarian oozes of Subunit IIA accumulated relatively slowly (115 mg/cm²/k.y.) between ~37.7 and 40 Ma then more than double (260 mg/cm²/k.y.) for a brief period in the middle Eocene between ~40 and 42 Ma (Fig. F17). Older radiolarian oozes and clayey radiolarian oozes accumulated more slowly, at ~120 mg/cm²/k.y. (Fig. F17). These values represent the first definition of a middle Eocene maximum in the accumulation rate in this facies. Subunit IIB spans ~14 m.y. of time and accumulated at a gross overall rate of ~120 mg/cm²/k.y.

The lower Eocene chalks of Unit III, near the base of the hole, accumulated at ~570 mg/cm²/k.y. (Fig. F17).

GEOCHEMISTRY

Interstitial Water Geochemistry

We collected interstitial waters from seven samples in Hole 1217A at depths ranging from 2.95 to 84.65 mbsf (Table T10; Fig. F18). Chemical gradients in the interstitial waters from Site 1217 reflect the dissolution of biogenic opal, the limited amount of organic matter diagenesis, and possibly the precipitation of authigenic minerals and the diffusive influence of reactions in the underlying basalt.

T10. Interstitial water data, p. 57.

F18. Interstitial water data, p. 39.

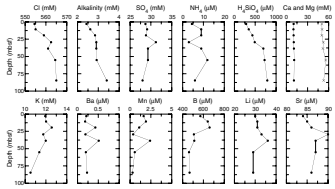

Chlorinity, as measured by titration, increases with depth from values of ~555 mM at 2.95 mbsf to values of ~565 mM at 84.65 mbsf. Chlorinity of the interstitial water samples from the upper two cores are lower than standard seawater (559 mM). Sodium concentrations as determined by charge balance (on average 1% lower than those measured by ion chromatograph) are similar to that of average seawater (480 mM) and show no consistent trend downhole. Salinity, as measured by a handheld refractometer, does not vary downhole; all interstitial waters were measured as 35.0, with the exception of a measurement of 36.0 at 55.15 mbsf.

Alkalinity values for the entire hole are higher than International Association for the Physical Sciences of the Ocean (IAPSO) standard seawater (2.325 mM) and increase slightly downhole from 2.43 mM at 2.95 mbsf to 3.40 mM at 84.65 mbsf. The pH ranges from 7.20 at 2.95 mbsf to a peak of 7.37 at 29.45 mbsf. Dissolved silica concentrations increase with depth from ~280 µM at 2.95 mbsf to values of ~789 µM at 84.65 mbsf. Dissolved silica concentrations are higher than at Sites 1215 and 1216, which is consistent with the presence of radiolarian ooze (from ~50 to 90 mbsf) at Site 1217.

Interstitial water sulfate concentrations remain at or above seawater concentrations (~28 mM) throughout the hole, indicating that the amount of labile organic matter available for oxidation is extremely low. Consistent with high sulfate values, ammonium is present at extremely low levels (<10 µM).

Dissolved manganese concentrations are low throughout the interstitial water profile at Site 1217 (<2.5 µM). Lithium and strontium concentrations are approximately or only slightly higher than seawater values (20 and 90 µM, respectively) throughout the pore water profiles.

Calcium concentrations in the pore waters from Site 1217 are similar to IAPSO concentrations (~10 mM). Magnesium concentrations are lower than IAPSO values (from 2.95 to 55.15 mbsf). These low magne-

sium concentrations in the pore waters may indicate magnesium uptake in the precipitation of yet unidentified authigenic minerals. Potassium concentrations increase from 11.9 to 12.6 mM for 0–19.45 mbsf. Below 19.45 mbsf, there is an overall decrease in potassium concentrations from 11.8 to 10.5 mM, which is consistent with higher levels of clay in the upper sediments (0–50 mbsf). The lack of increasing calcium and decreasing magnesium concentrations with depth likely indicates that the diffusive influence of reactions in the underlying basalt is small in these pore waters. Dissolved barium concentrations are low (~<0.50 µM). Boron concentrations range from 461 to 659 µM, higher than seawater value (416 µM).

In summary, the pore water profiles from Site 1217 are influenced by the dissolution of biogenic silica, authigenic mineral precipitation, possibly alteration of underlying basalt, and subsequent diffusion. High levels of sulfate and concomitant low levels of ammonium indicate an oxic environment consistent with the occurrences of metalliferous oxides within the sediment. Silica and alkalinity levels in the interstitial waters are higher than seawater values (and higher than values from Sites 1215 and 1216), indicating the relative importance of biogenic silica as a component of these sediments.

Solid-Phase Geochemistry

We collected bulk-sediment samples adjacent to the interval sampled for physical properties (see "Physical Properties," p. 18), resulting in a sampling resolution of approximately one per section from 0.79 to 128.83 mbsf in Hole 1217A (Table T11; Fig. F19). We also collected samples from 31.74 to 72.73 mbsf in Hole 1217B to fill in gaps in the Hole 1217A sediment column (Table T11; Fig. F19). We show all data plotted against depth in mcd for Site 1217 (Fig. F19). Depth in mbsf and mcd for each hole is provided (Table T11). We measured silicon (Si), aluminum (Al), titanium (Ti), iron (Fe), manganese (Mn), calcium (Ca), magnesium (Mg), phosphorus (P), strontium (Sr), and barium (Ba) concentrations in the sediment by inductively coupled plasma–atomic emission spectroscopy (ICP-AES). Bulk-sediment geochemistry primarily reflects the changing lithology of the sediments from red clay to nannofossil ooze in Unit I to radiolarian ooze and clay in Subunit IIA to nannofossil chalk in Unit III.

Silicon generally ranges between 20 and 30 wt%, which is consistent with the dominance of red clay and siliceous sediment throughout most of the depth range (Fig. F19). The exceptions are a decrease in silicon to ~11 wt% in the nannofossil ooze section between 27 and 29 mcd and a decrease to ~4 wt% in a sample from 129 mcd in the nannofossil chalk.

Aluminum and titanium in Site 1217 sediments follow similar trends of aluminum and titanium in sediments from Sites 1215 and 1216. Aluminum decreases overall downhole from ~9 wt% at 0.79 mcd to <1 wt% at 129.09 mcd (Fig. F19). The nannofossil ooze is marked by lower aluminum values (<3 wt%). Titanium content decreases from 0.91 wt% at 0.79 mcd to 0.01 wt% at 129.09 mcd. Titanium values in the shallowest sediments (0–5 mcd) are higher than observed in Sites 1215 and 1216 sediments. Al/Ti ratios in these shallow sediments are significantly lower (as low as 10) than at Sites 1215 and 1216.

Iron and manganese contents show similar trends to each other (Fig. F19). In the red clay Unit I (~0–50 mcd), iron varies between ~5 and ~9 wt% and manganese varies between 0.5 and ~1.5 wt%. Both iron and

T11. Bulk-sediment data, p. 58.

F19. Bulk-sediment data, p. 40.

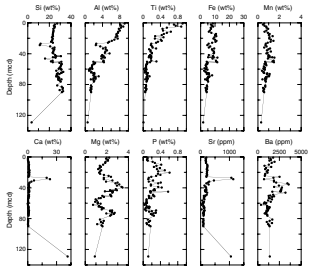

manganese decrease in the radiolarian ooze and the nannofossil chalk (Units II and III).

Consistent with the lack of carbonate in most sections, calcium is generally <2 wt% at Site 1217, with the exception of nannofossil ooze, where calcium is as high as 23 wt% (from ~27 to 29 mcd), and nannofossil chalk, where calcium is measured at ~42 wt% (129 mcd) (Fig. F19). This 42 wt% value for Ca cannot be accurate because 100 wt% $CaCO_3$ is 40 wt% Ca. Possible reasons for this discrepancy are given in "Geochemistry," p. 20, in the "Explanatory Notes," chapter. A more accurate value for $CaCO_3$ (wt%) determined by coulometer is 83.55% (see Table T12). Likewise, strontium is low (at ~200 ppm throughout) with the exception of peaks of ~1000 ppm in the nannofossil ooze and chalk (~27–29 mcd). Magnesium varies between 1.2 and 3 wt%.

T12. Calcium carbonate and organic carbon data, p. 60.

Similar to Sites 1215 and 1216, phosphorus is low (generally <0.5 wt%) in Site 1217 sediments (Fig. F19). Barium contents in Site 1217 sediments are highest between 25 and 50 mcd (>2500 ppm) and are generally higher than at Site 1215 or 1216.

Calcium carbonate ($CaCO_3$) (in weight percent) and organic carbon (C_{org}) (in weight percent) were determined for approximately two samples per section from 0.79 to 128.83 mbsf in Hole 1217A and for one sample per core from 31.74 to 72.73 mbsf in Hole 1217B to fill in gaps in the Hole 1217A sediment column (Table T12). $CaCO_3$ measured by coulometer is low (less than or equal to ~1 wt%) for all of the sediments from Site 1217 except for samples between 26 and 31 mbsf and a further sample at 128.83 mbsf in Hole 1217A. $CaCO_3$ values calculated from Ca contents yielded similar trends to $CaCO_3$ measured via coulometer, although absolute values are lower for low carbonate values (<1 wt%) and higher for values >1 wt% (Table T12). Calculated values were negative for some samples, indicating a problem with the calibration at very low carbonate values (see "Geochemistry," p. 20, in the "Explanatory Notes" chapter). C_{org} is uniformly low (0–0.40 wt%) for all samples measured (Table T12).

In summary, the bulk geochemistry of the sediments from Site 1217 reflects the varying lithology of the sediments between red clay, nannofossil ooze/chalk, and the increasing proportion of siliceous biogenic sediments relative to earlier sites.

PHYSICAL PROPERTIES

Physical properties at Site 1217 were measured on whole cores, split cores, and discrete samples. MST measurements (bulk density, MS, *P*-wave velocity, and NGR) and thermal conductivity comprised the whole-core measurements. Compressional wave velocity measurements on split cores and moisture and density (MAD) analyses on discrete core samples were made at a frequency of one per undisturbed section in Hole 1217A. Intervals that were disturbed or not recovered in Hole 1217A were sampled in Hole 1217B for velocity and MAD analyses. Light absorption spectroscopy (LAS) analyses were performed on the MAD samples as well as an additional one sample per section (located ~50 cm from the MAD sample) in Hole 1217A.

Density and Porosity

Two methods were used to evaluate the wet bulk density at Site 1217. GRA provided an estimate from whole cores. MAD samples gave a second, independent measure of wet bulk density as well as providing DBD, grain density, water content, and porosity from a discrete sample (Table T13). The MAD and GRA bulk density measures display the same trends, but the MAD densities are offset to higher values by 0.05–0.10 g/cm³ (Fig. F20). Crossplots of wet bulk density and DBD vs. interpolated GRA density (Fig. F21) show that despite the offset, the overall match between the data sets is excellent.

Wet bulk density at Site 1217 is highest between the seafloor and 22 mbsf, with values averaging 1.37 g/cm³. Below 22 mbsf, wet bulk density decreases sharply, reaching a minimum of 1.18 g/cm³ at 25.58 mbsf. The density of the nannofossil ooze in lithologic Unit I (between 27 and 32 mbsf) is distinctly higher at ~1.28 g/cm³. Below the nannofossil ooze, the increase in abundance of radiolarians results in lower wet bulk density. Density values average 1.19 g/cm³ with little variation in the sediments recovered from the lower part of Units I and II. The nannofossil chalk of Unit III was sampled at 128.83 mbsf and has a wet bulk density of 1.79 g/cm³.

Grain density (ρ_s) averages 2.62 g/cm³ in the uppermost 5 m at Site 1217. Below 5 mbsf, it decreases and becomes more variable, coinciding with the LAS-indicated decrease in illite and increase in smectite in the sediment (Fig. F20). A grain density increase below 22 mbsf accompanies the LAS-indicated increase in calcite. Between 5 and 34 mbsf, grain density averages 2.53 g/cm³. Below 34 mbsf, grain density is lower and more variable, which coincides with an increase in radiolarian abundance. The average grain density for the lower part of Units I and II is 2.32 g/cm³. The grain density in Unit III is 2.73 g/cm³.

Porosity and water content vary inversely with wet bulk density (Fig. F20). Porosity averages 75% in the uppermost 22 m at Site 1217. Below 22 mbsf, porosity increases sharply and remains high, averaging 88%. The porosity of the Unit III nannofossil chalk is 55%.

LAS

LAS studies were conducted on cores from Hole 1217A at a frequency of two samples per section (see **Vanden Berg and Jarrard,** this volume, for a discussion of the LAS technique). Semiquantitative mineral concentrations were calculated from the collected spectra, assuming a four-component system: calcite, opal, smectite, and illite (Table T14). LAS analyses display the major changes in mineralogy over the different lithologic boundaries (Fig. F22). The upper 10 m of clay contain the distinct illite/smectite transition zone also seen at Sites 1215 and 1216. In the nannofossil ooze between 27 and 32 mbsf, calcite concentrations increase to ~43%, whereas clay contents decrease. The high opal sample (58%) located in this region marks a small bed of radiolarian ooze located at 28 mbsf. An increase in opal concentrations from 25% to 50% marks a change from clay-rich sediments (smectite rich) to a radiolarian ooze with clay at 52 mbsf. Over the interval from 52 to 90 mbsf, clay (smectite) contents increase downcore, whereas opal contents decrease. Lithologic Subunit IIB was not sampled because of severe core disturbance. The final LAS sample is located at 128.8 mbsf and contains 63%

T13. Moisture and density measurements, p. 61.

F20. MAD measurements, p. 41.

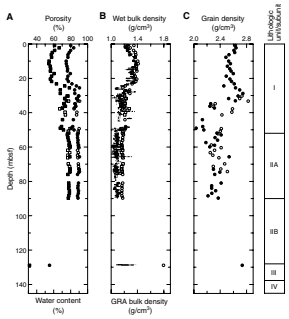

F21. Wet and dry bulk density plotted with GRA bulk density, p. 42.

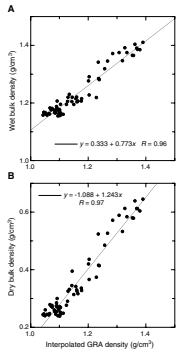

T14. LAS-based mineralogy, p. 62.

F22. LAS mineralogy determinations, p. 43.

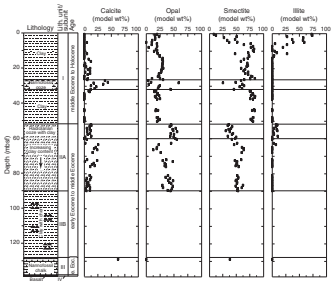

calcite, which is consistent with the lithologic description of a nannofossil chalk.

Compressional Wave Velocity

Compressional wave velocity was measured by the *P*-wave logger (PWL) on whole cores from Holes 1217A, 1217B, and 1217C and the insertion and contact probe systems on split cores from Holes 1217A and 1217B (Table T15). The match between the whole-core and split-core measurements is relatively good for the insertion probe system, but the contact probe values are ~25 m/s higher than the PWL values (Fig. F23). The general trends in the velocities are an increase from 1470 m/s near the seafloor to 1550 m/s at ~30 mbsf, a decrease to ~1510 m/s at 35 mbsf, and higher, more variable velocities below 35 mbsf. The maximum velocity measured was 1595 m/s for the nannofossil chalk of lithologic Unit III.

Velocity anisotropy was calculated from longitudinal (z-direction) and transverse (y-direction) measurements provided by the insertion probe system (Table T15) to evaluate burial-induced changes in sediment fabric. The anisotropy ranges from –0.7% to 1.8% and averages 0.9% (omitting an anomalous value of 3.0%) with no consistent trend with depth.

Thermal Conductivity

Thermal conductivity was measured on the third section of cores from Hole 1217A (Table T16). The thermal conductivity averages 0.75 W/(m·K). As is the case at Sites 1215 and 1216, there is a general inverse relationship between thermal conductivity and porosity at Site 1217.

NGR

NGR was measured on all whole cores at Site 1217 and displays trends similar to the other physical properties (Fig. F24). Between the seafloor and 25 mbsf, NGR values are high (~25 counts per second [cps]). Unlike Sites 1215 and 1216, the LAS-indicated illite/smectite transition in the upper 10 m is not marked by a decrease in NGR values. Below 25 mbsf, the NGR values decrease to ~1 cps and remain at this level to the bottom of Hole 1217A.

MS

Whole-core MS measurements display greater variability than other properties and only somewhat follow the identified changes in lithology (Fig. F25). The susceptibility increases from 50 × 10^{-6} SI at the seafloor to nearly 200 × 10^{-6} SI at 12 mbsf. This increase coincides with a 0.2 g/cm³ increase in the GRA bulk density (Fig. F20) and the transition from illite to smectite clay. Between 12 and 25 mbsf, MS values decrease back to the range of 75 to 125 × 10^{-6} SI. Significantly lower susceptibility (~35 × 10^{-6} SI) marks the calcite-rich nannofossil ooze between 27 and 32 mbsf. Between 32 and 51 mbsf, MS values again increase to ~80 × 10^{-6} SI as a result of an increase in clay content. Lithologic Subunit IIA, radiolarian-rich clay, is characterized by another drop in MS to values of ~50 × 10^{-6} SI.

T15. Split-core velocity measurements, p. 63.

F23. Compressional wave velocity, p. 44.

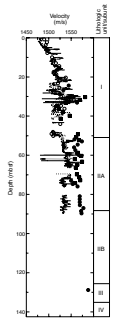

T16. Thermal conductivity measurements, p. 64.

F24. Natural gamma radiation, p. 45.

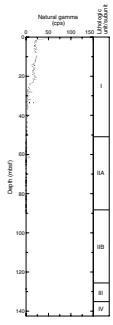

F25. Magnetic susceptibility, p. 46.

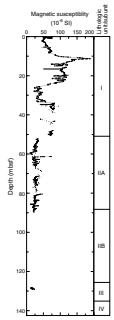

REFERENCES

Berggren, W.A., and Miller, K.G., 1989. Cenozoic bathyal and abyssal calcareous benthic foraminiferal zonations. *Micropaleontology,* 35:308–320.

Cande, S.C., and Kent, D.V., 1995. Revised calibration of the geomagnetic polarity timescale for the Late Cretaceous and Cenozoic. *J. Geophys. Res.,* 100:6093–6095.

Cande, S.C., LaBrecque, J.L., Larson, R.L., Pitmann, W.C., III, Golovchenko, X., and Haxby, W.F., 1989. *Magnetic Lineations of the World's Ocean Basins*. AAPG Map Ser., 13.

Engebretson, D.C., Cox, A., and Gordon, R.G., 1985. *Relative Motions Between Oceanic and Continental Plates in the Pacific Basin*. Spec. Pap.—Geol. Soc. Am., 206.

Gripp, A.E., and Gordon, R.G., 1990. Current plate velocities relative to the hotspots incorporating the NUVEL-1 global plate motion model. *Geophys. Res. Lett.,* 17:1109–1112.

Janecek, T.R., and Rea, D.K., 1983. Eolian deposition in the northeast Pacific Ocean: Cenozoic history of atmospheric circulation. *Geol. Soc. Am. Bull.,* 94:730–738.

Kyte, F.T., Leinen, M., Heath, G.R., and Zhou, L., 1993. Cenozoic sedimentation history of the central North Pacific: inferences from the elemental geochemistry of Core LL44-GPC3. *Geochim. Cosmochim. Acta,* 57:1719–1740.

Nomura, R., 1995. Paleogene to Neogene deep-sea paleoceanography in the eastern Indian Ocean: benthic foraminifera from ODP Sites 747, 757, and 758. *Micropaleontology,* 41:251–290.

Petronotis, K.E., Gordon, R.G., and Acton, G.D., 1994. A 57 Ma Pacific plate paleomagnetic pole determined from a skewness analysis of crossings of marine magnetic anomaly 25r. *Geophys. J. Int.,* 118:529–554.

Sanfilippo, A., and Nigrini, C., 1998. Code numbers for Cenozoic low latitude radiolarian biostratigraphic zones and GPTS conversion tables. *Mar. Micropaleontol.,* 33:109–156.

van Andel, T.H., Heath, G.R., and Moore, T.C., Jr., 1975. *Cenozoic History and Paleoceanography of the Central Equatorial Pacific Ocean: A Regional Synthesis of Deep Sea Drilling Project Data*. Mem.—Geol. Soc. Am., 143.

van Morkhoven, F.P.C.M., Berggren, W.A., Edwards, A.S., 1986. *Cenozoic Cosmopolitan Deep-water Benthic Foraminifers*. Bull. Cent. Rech. Explor.—Prod. Elf-Aquitaine Mem. 11.

Figure F1. Location of Site 1217 in the Leg 199 transect. In the lower panel, gray shading = seafloor depths >5000 mbsl, red shading = approximate position of magnetic Anomaly C25, the nominal target crust of the 56-Ma transect.

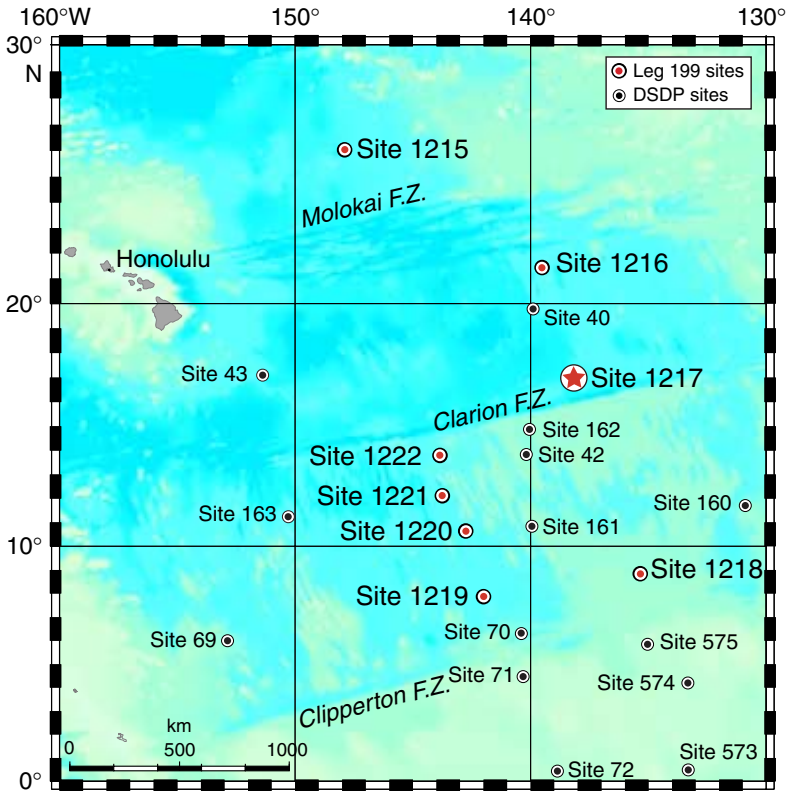

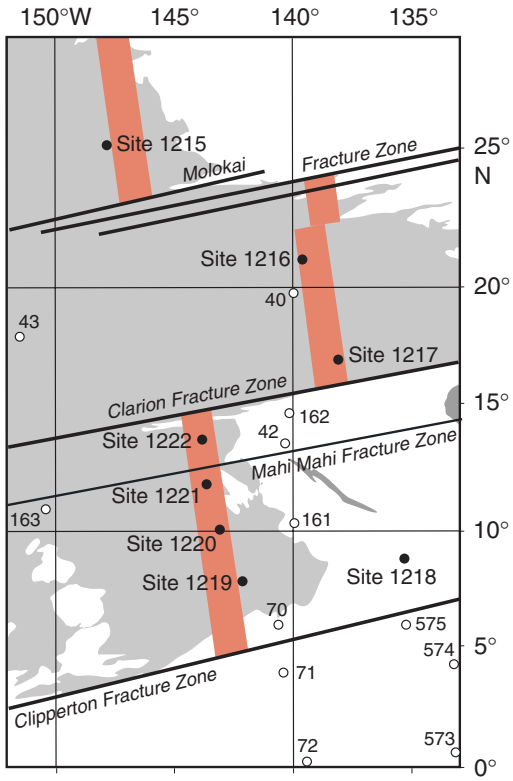

Figure F2. Seismic reflection profile for Site 1217. The sedimentary section is marked by a weak reflection at about 44 ms two-way traveltime (TWT) (~35 mbsf) and stronger reflections below 131 ms TWT (~100 mbsf) that we assumed to mark the basal carbonate sequence.

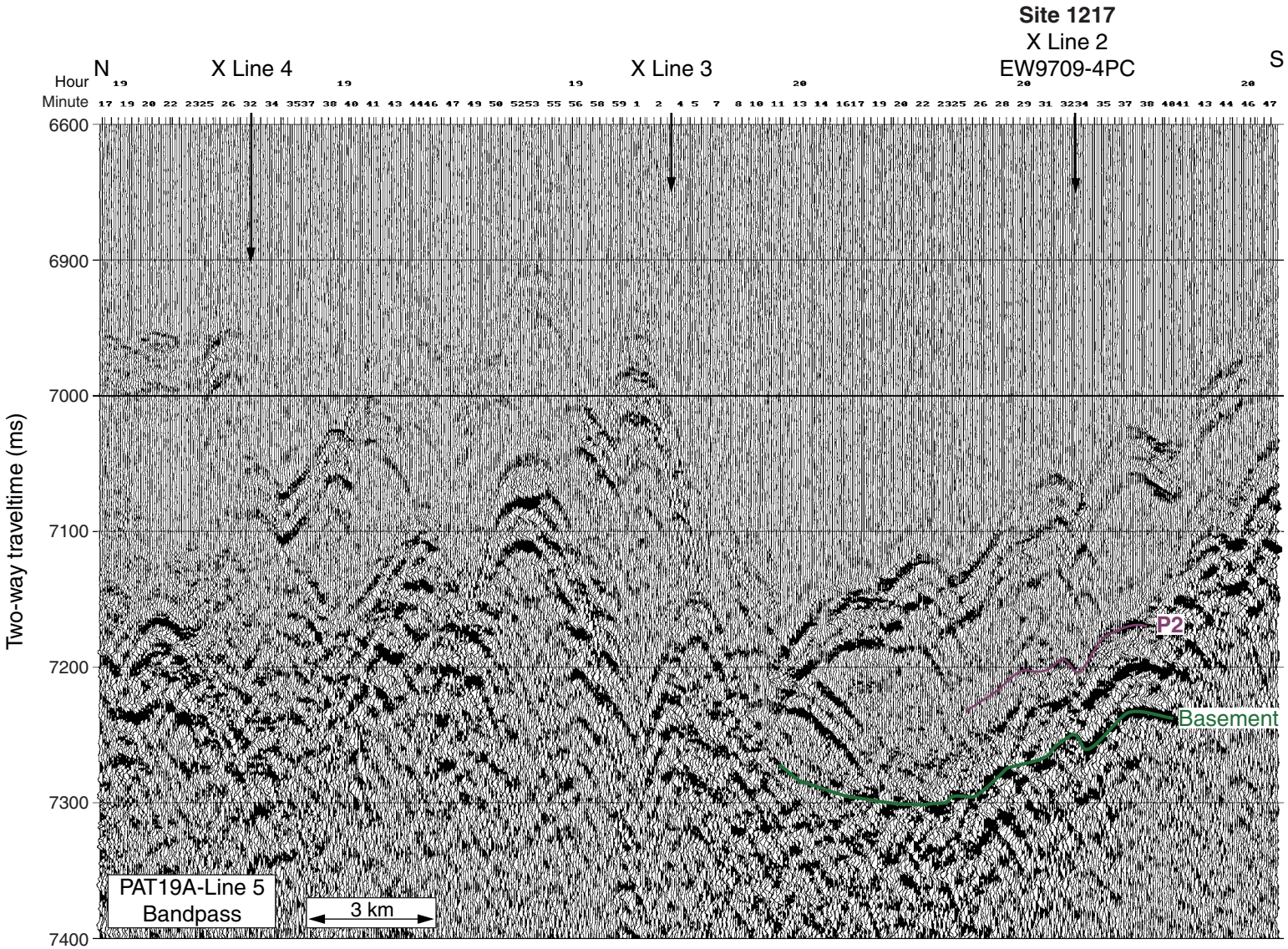

Figure F3. Lithologic summary for Site 1217. LAS = light absorption spectroscopy, cps = counts per second, TD = total depth.

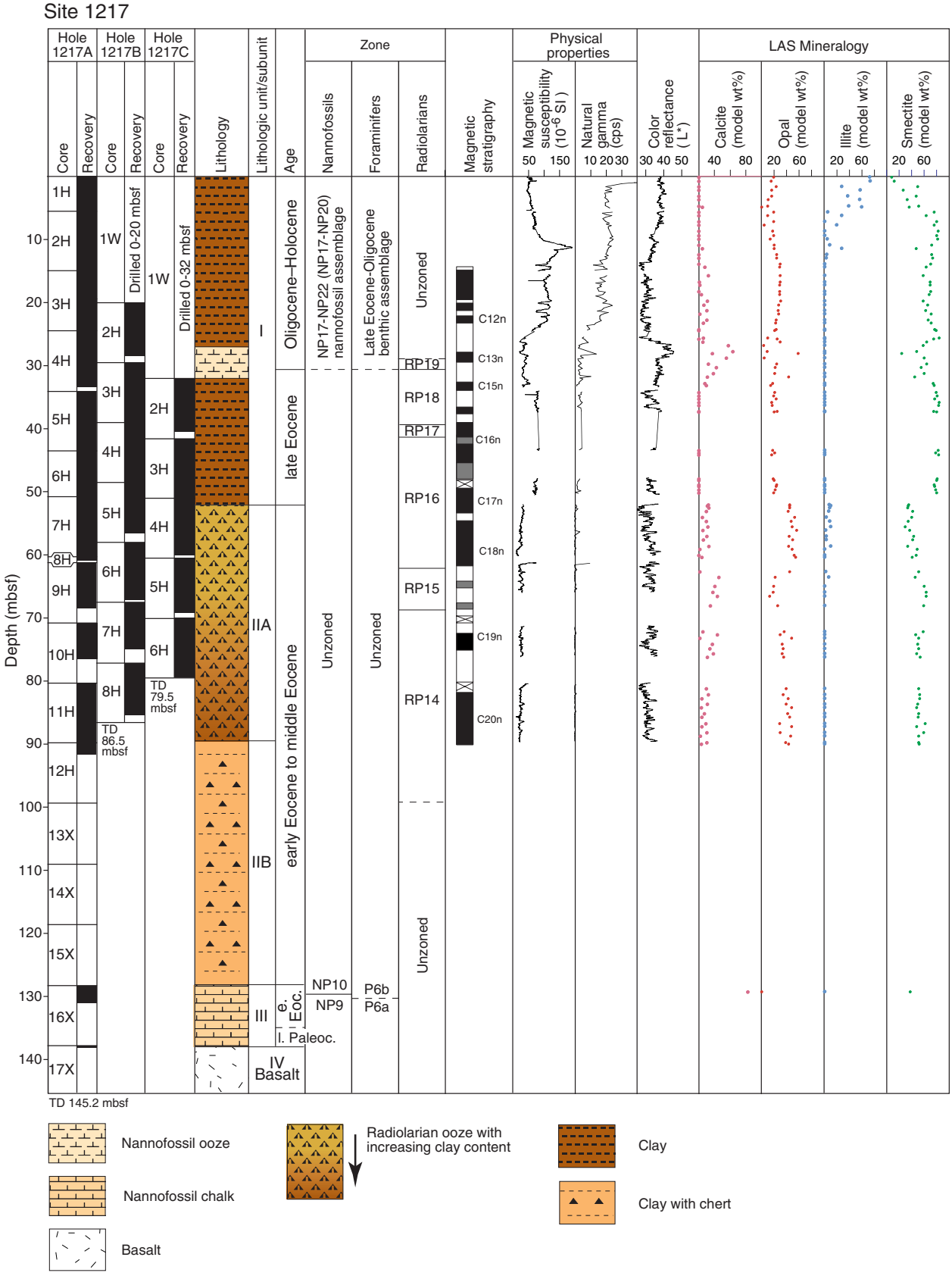

Figure F4. Close-up digital photograph of ash layer within the nannofossil ooze (Unit I; interval 199-1217A-4H-6, 22–61 cm). The ash layer has a sharp lower contact with the nannofossil ooze and bioturbated upper contact.

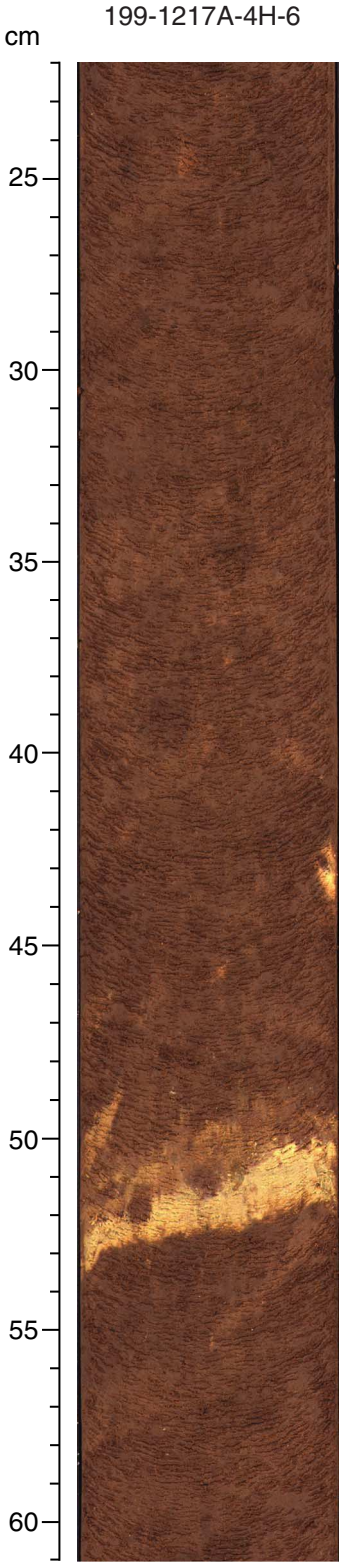

Figure F5. Close-up digital photograph of a pumice pebble from within Subunit IIA (interval 1217B-8H-3, 124–143 cm).

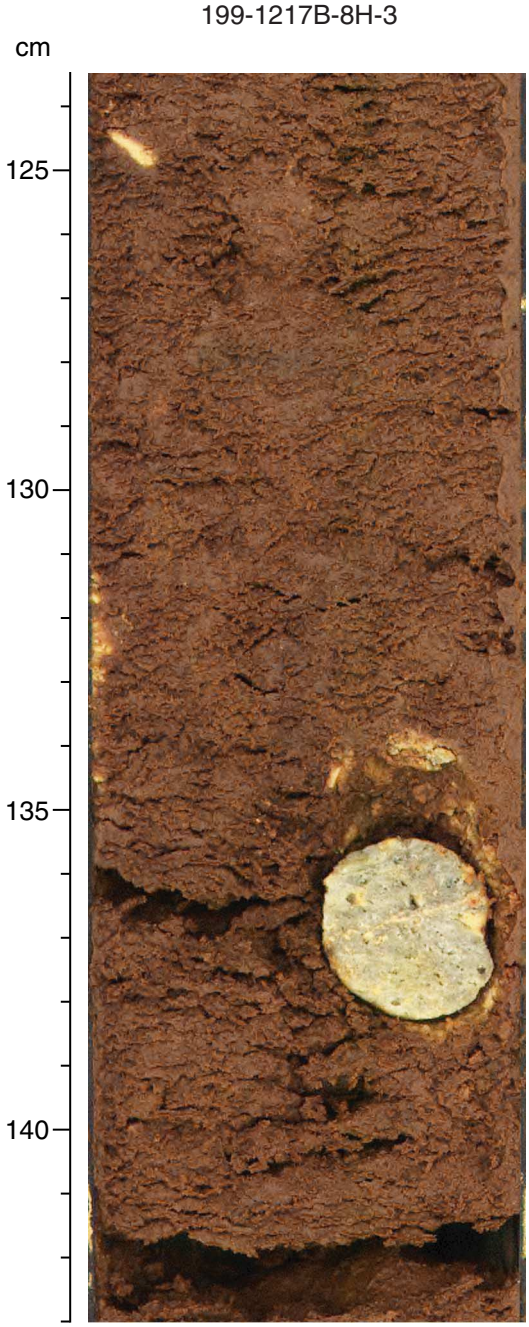

Figure F6. A. Close-up digital photograph of nannofossil chalk with clay and dolomite (Unit III; interval 199-1217A-16X-1, 70–76 cm). The interval is heavily bioturbated. The darker bands are nannofossil claystone with dolomite with lighter bands of nannofossil chalk. **B.** Close-up digital photograph of dolomite rhombs collected on a 63-µm mesh sieve (interval 199-1217A-16X-2, 19–21 cm.)

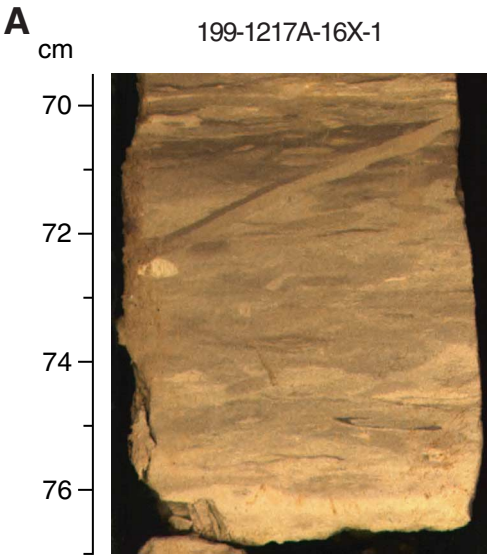

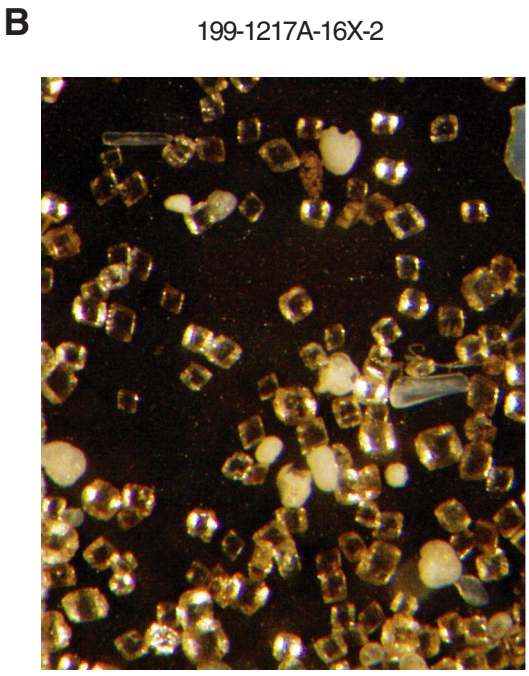

Figure F7. DSDP Site 162 percent carbonate data (van Andel et al., 1975) showing the lower Oligocene nannofossil ooze interval (0–28 mbsf).

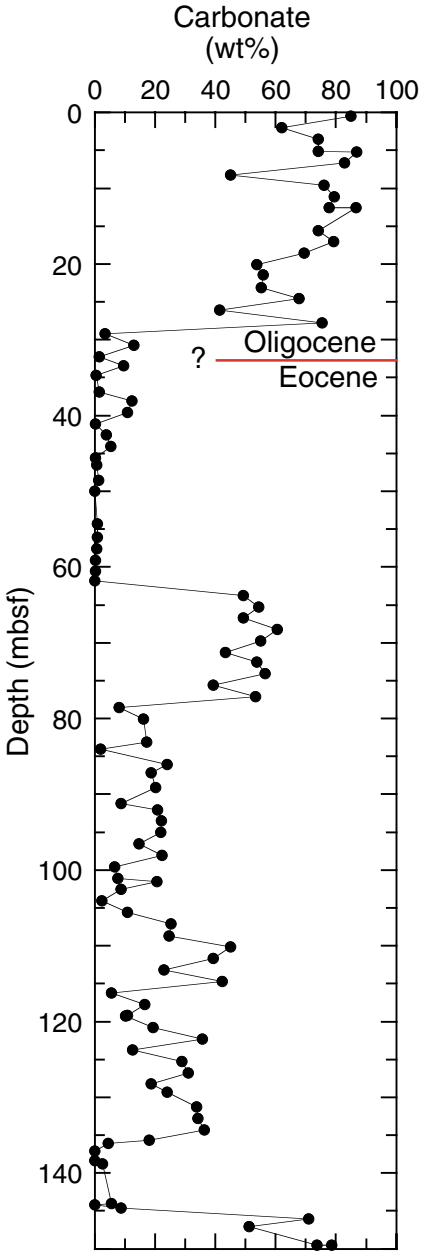

Figure F8. Distribution of biostratigraphic zones for radiolarians at Site 1217 (Sanfilippo and Nigrini, 1998). Shaded areas = unsampled or poorly preserved material. Horizontal dashed lines = boundary can only be approximated by available biostratigraphy. TD = total depth.

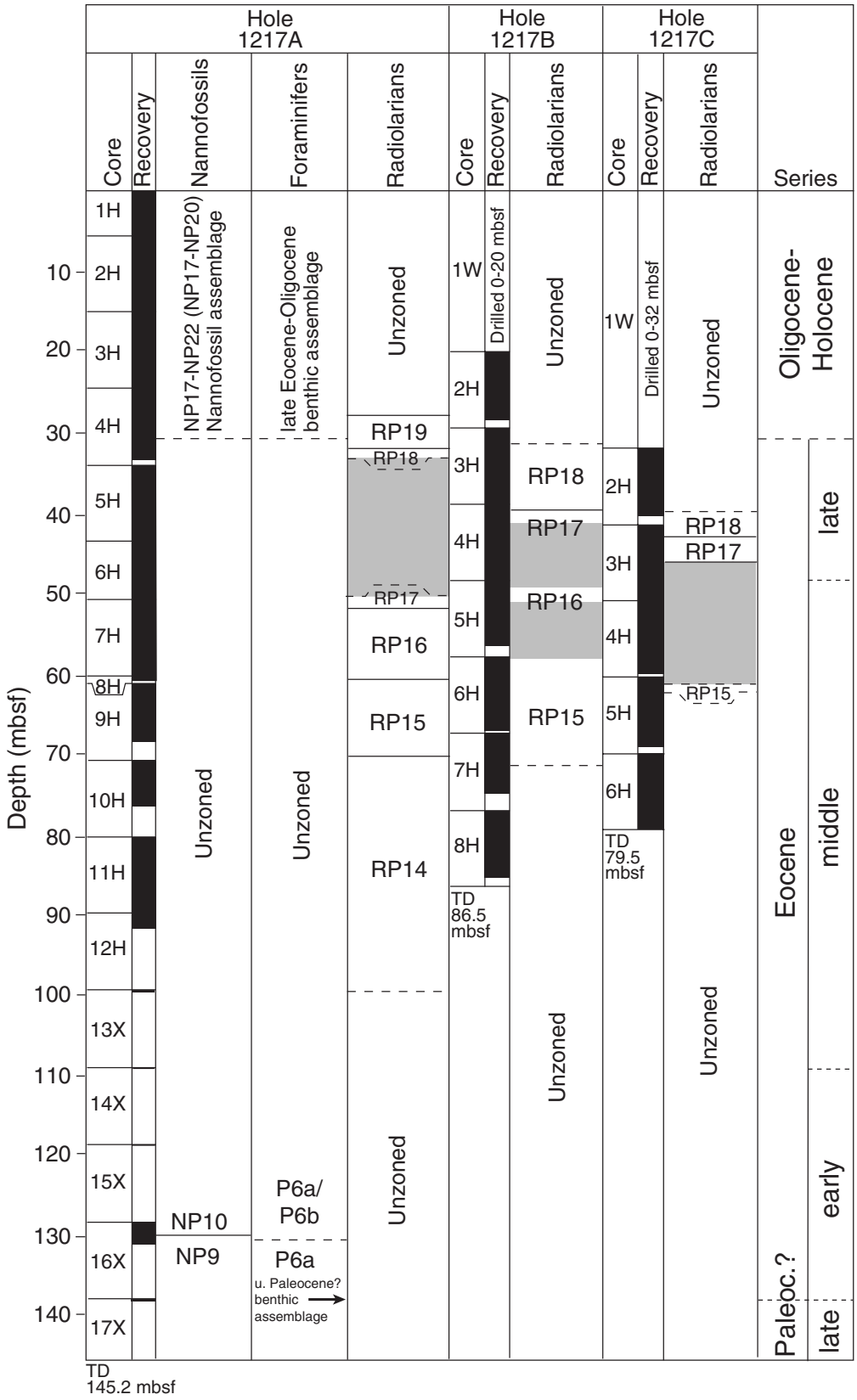

Figure F9. Archive-half magnetization intensities after AF demagnetization at a peak field of 20 mT from Hole 1217A. Lithologic Unit I/II boundary shown on right.

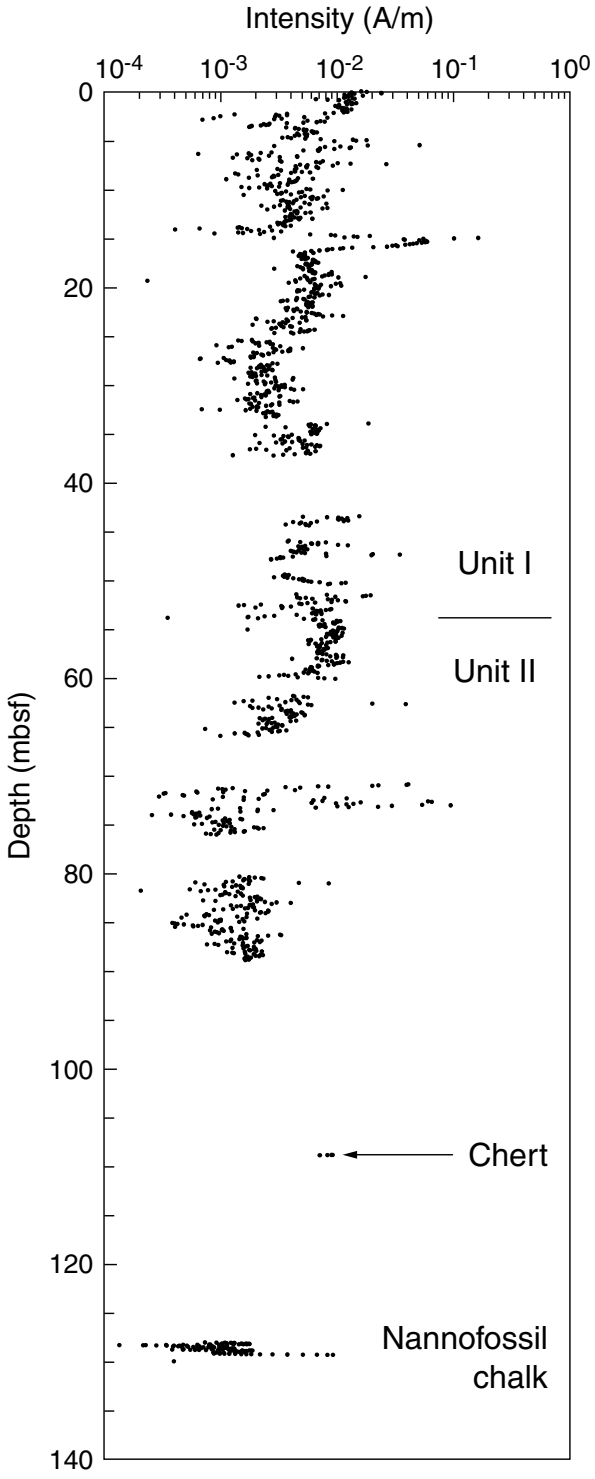

Figure F10. Example of progressive AF demagnetization of Sample 199-1217A-7H-7, 43 cm. *J* = intensity.

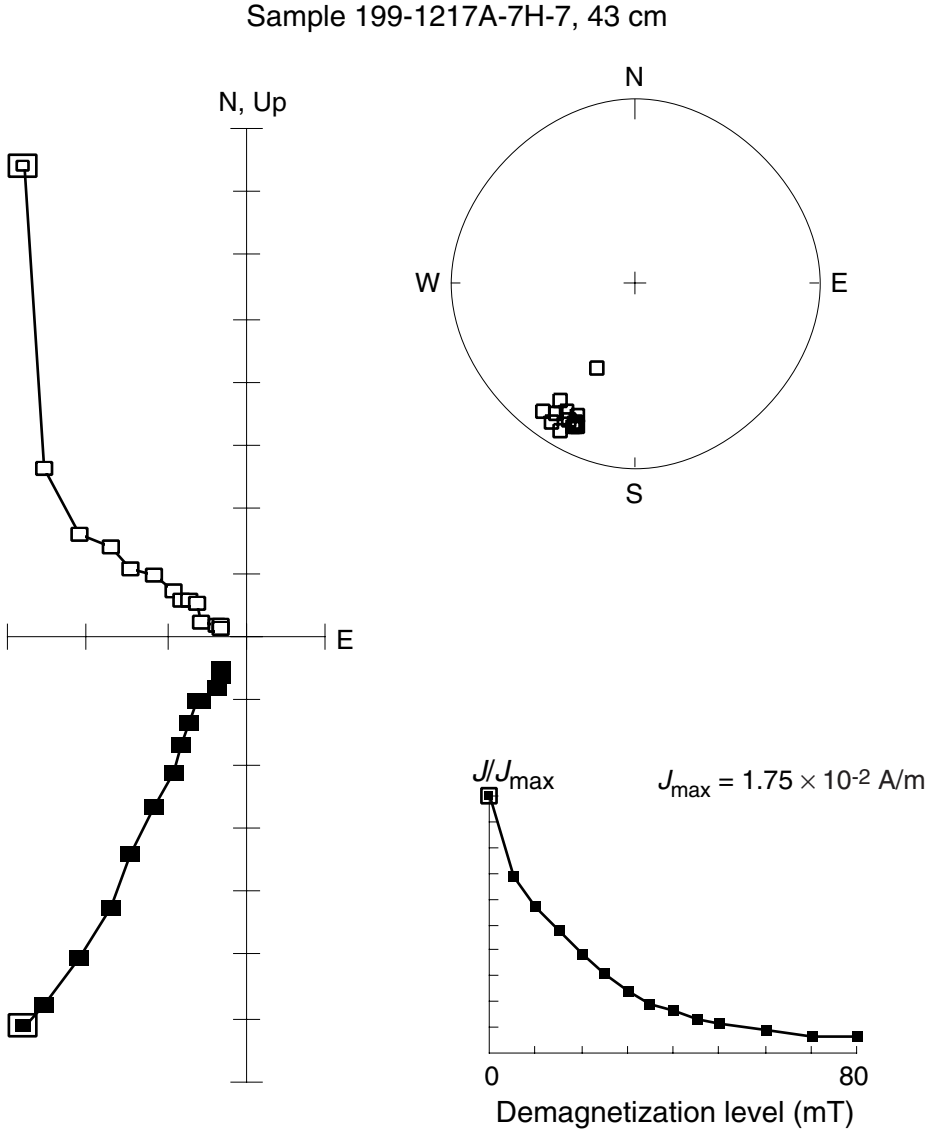

Figure F11. Composite magnetic stratigraphy at Site 1217. Virtual geomagnetic pole (VGP) latitudes were obtained after partial AF demagnetization of continuous measurements at a peak field of 20 mT. Polarity column shows interpreted zones of normal (black) and reversed (white) magnetization. Gray intervals indicate zones with an uncertain polarity interpretation. Solid circles = Hole 1217A, triangles = Hole 1217B, open circles = Hole 1217C.

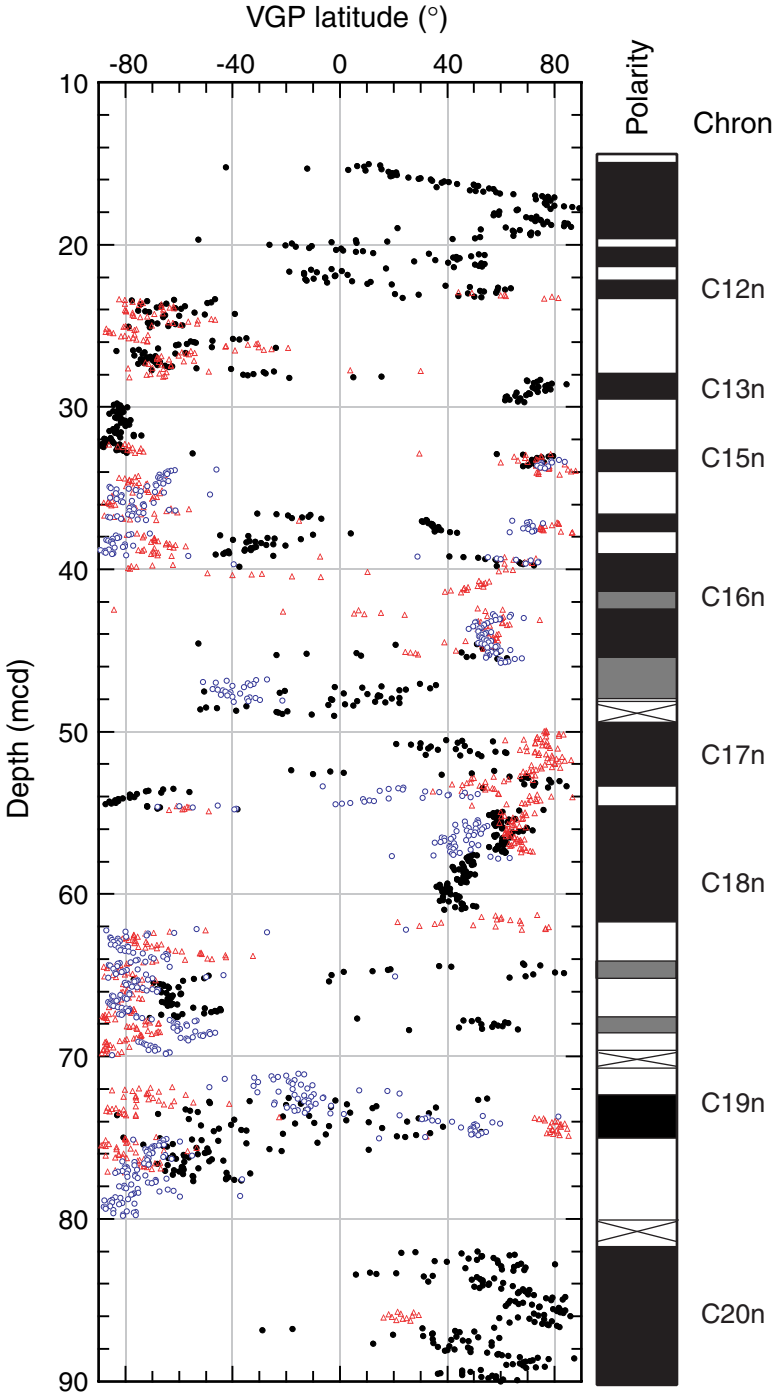

Figure F12. MST data plotted vs. depth at Hole 1217A. Gamma ray attenuation (GRA) bulk density, magnetic susceptibility, color reflectance (L*), *P*-wave velocity, and natural gamma count data are shown for Holes 1217A (left curve in each panel), 1217B (middle curve in each panel), and 1217C (right curve in each panel). The data from Holes 1217B and 1217C are offset by constants for illustration purposes. All data sets (except natural gamma counts) are smoothed with a nine-point Gaussian filter. Intervals with obvious flow-in or drilling disturbance were removed from the data sets (see Table **T4,** p. 51). NGR = natural gamma ray, cps = counts per second.

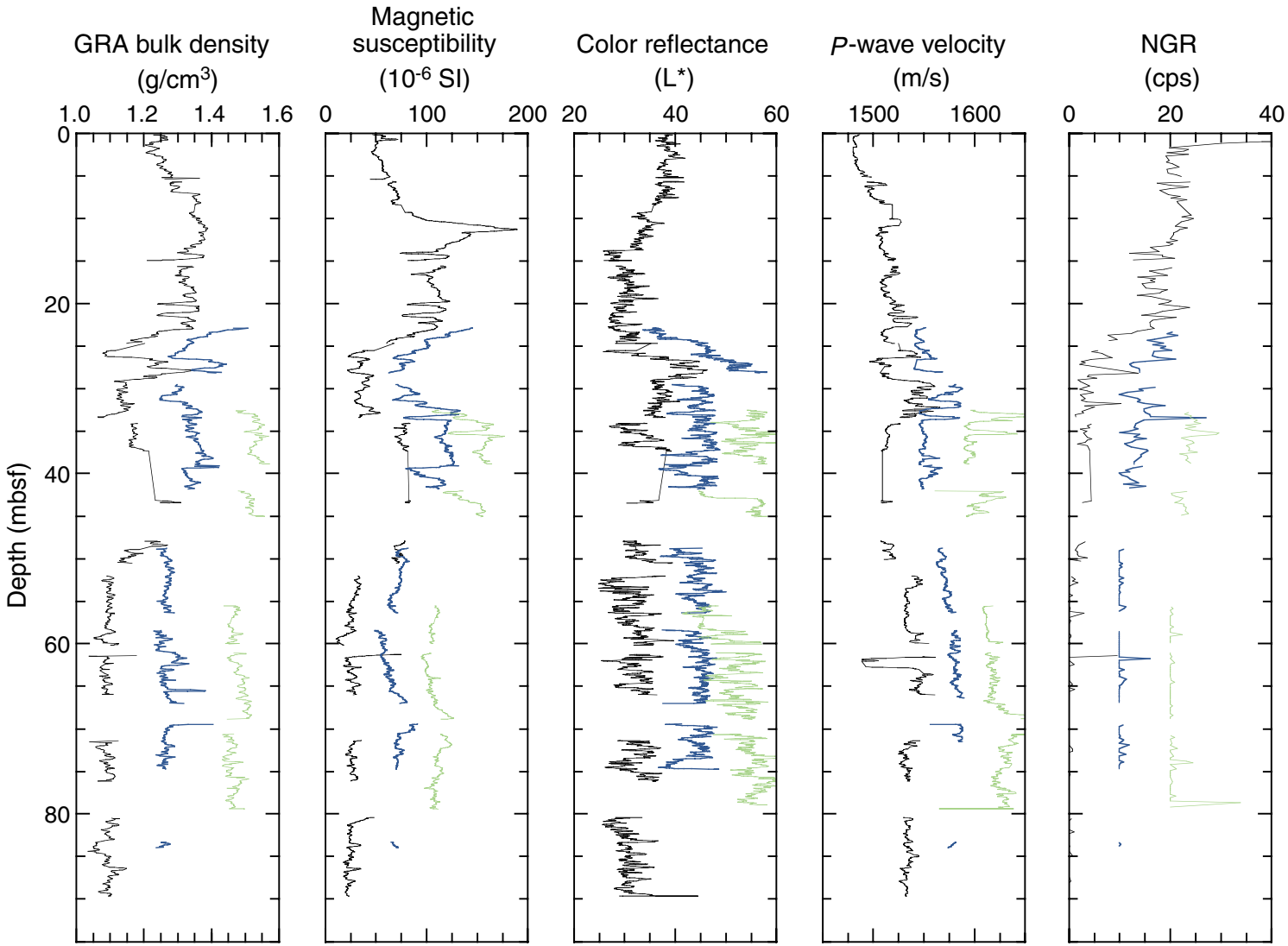

Figure F13. MST data plotted vs. composite depth at Hole 1217A. Gamma ray attenuation (GRA) bulk density, magnetic susceptibility, color reflectance (L*), *P*-wave velocity, and natural gamma count data are shown for Holes 1217A (left curve in each panel), 1217B (middle curve in each panel), and 1217C (right curve in each panel). The data from Holes 1217B and 1217C are offset by constants for illustration purposes. All data sets (except natural gamma counts) are smoothed with a nine-point Gaussian filter. Intervals with obvious flow-in or drilling disturbance were removed from the data sets (see Table **T4**, p. 51). NGR = natural gamma ray, cps = counts per second.

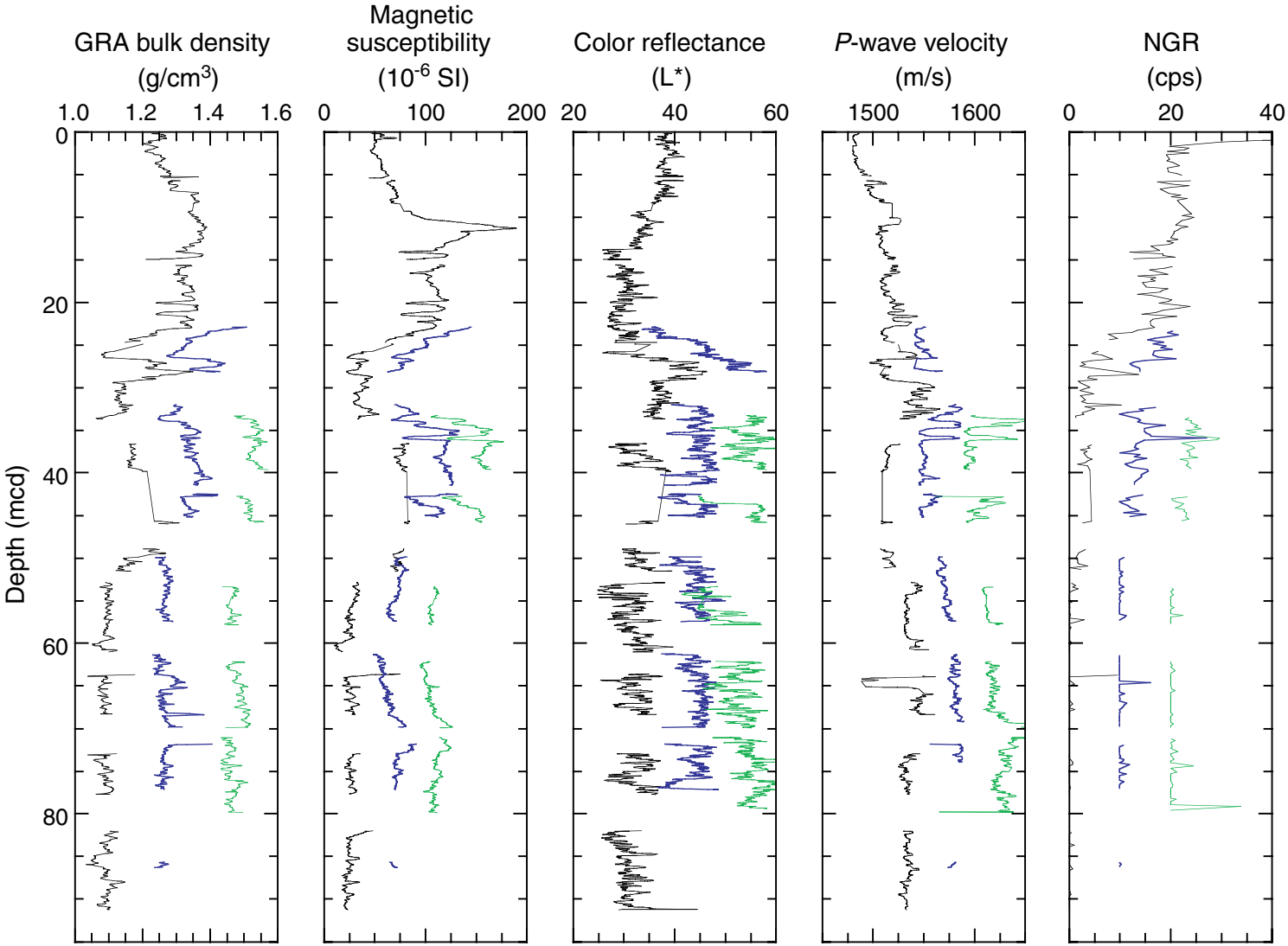

Figure F14. Spliced records of gamma ray attenuation (GRA) bulk density, magnetic susceptibility, color reflectance (L*), *P*-wave velocity, and natural gamma count data for Site 1217 plotted vs. composite depth. The splice for each record was constructed using the Table **T6,** p. 53. All data sets (except natural gamma counts) are smoothed with a nine-point Gaussian filter. Intervals with obvious flow-in or drilling disturbance were removed from the data sets (see Table **T4,** p. 51). NGR = natural gamma ray, cps = counts per second.

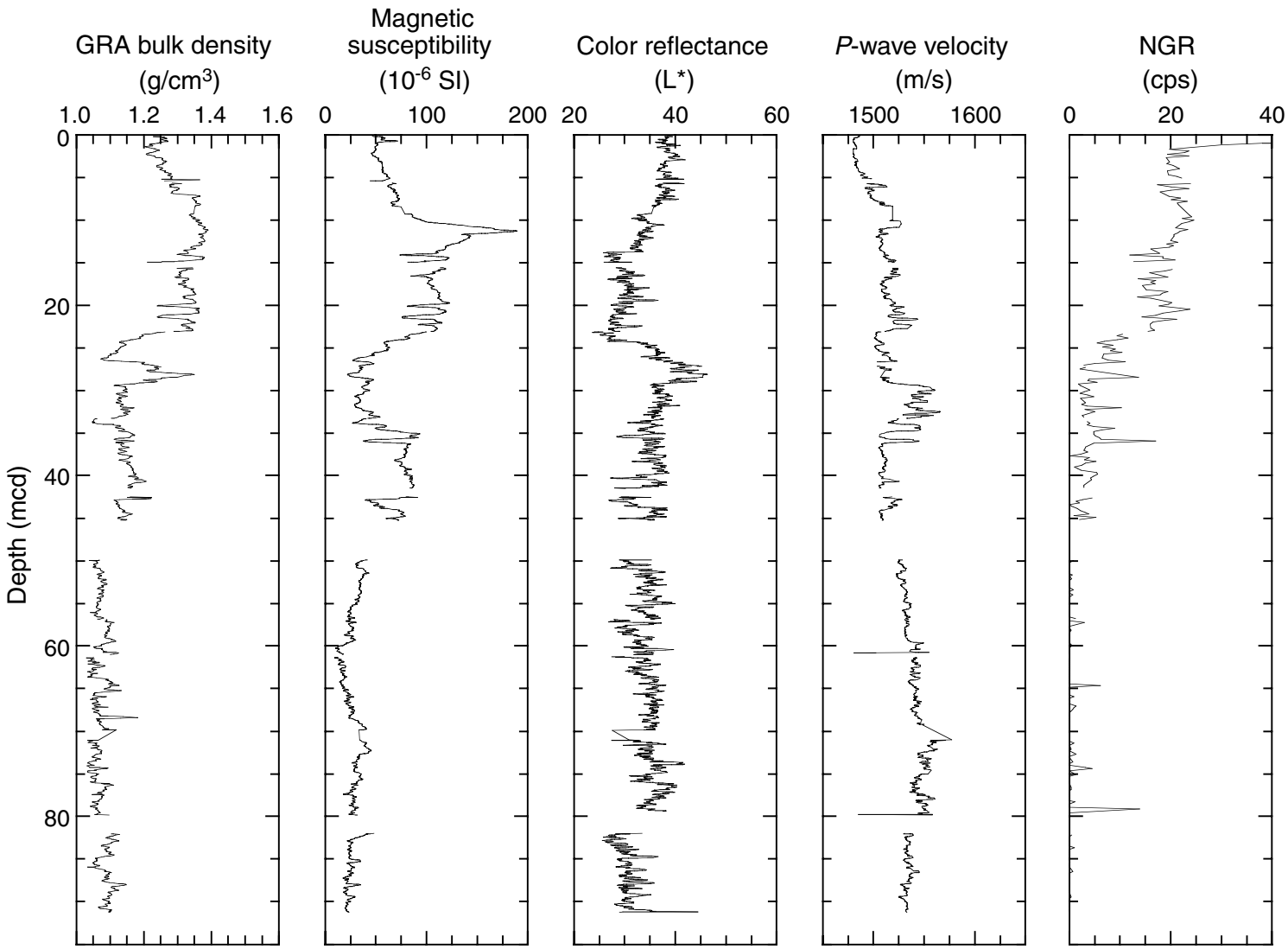

Figure F15. Plot of biostratigraphic and paleomagnetic datum levels (see Tables T7, p. 54, and T8, p. 55) used to constrain average LSR vs. depth. Individual symbols represent different types of stratigraphic datums: solid circle = nannofossils datums, solid diamond = paleomagnetic reversal. Solid line segments = linear regressions of selected data points with the slope of these lines indicating sedimentation rates in m/m.y., as shown next to each segment. MARs are shown as values in mg/cm²/k.y. (see Table T9, p. 56). MAR values for the lower interval are shown in detail on Figure F17, p. 38.

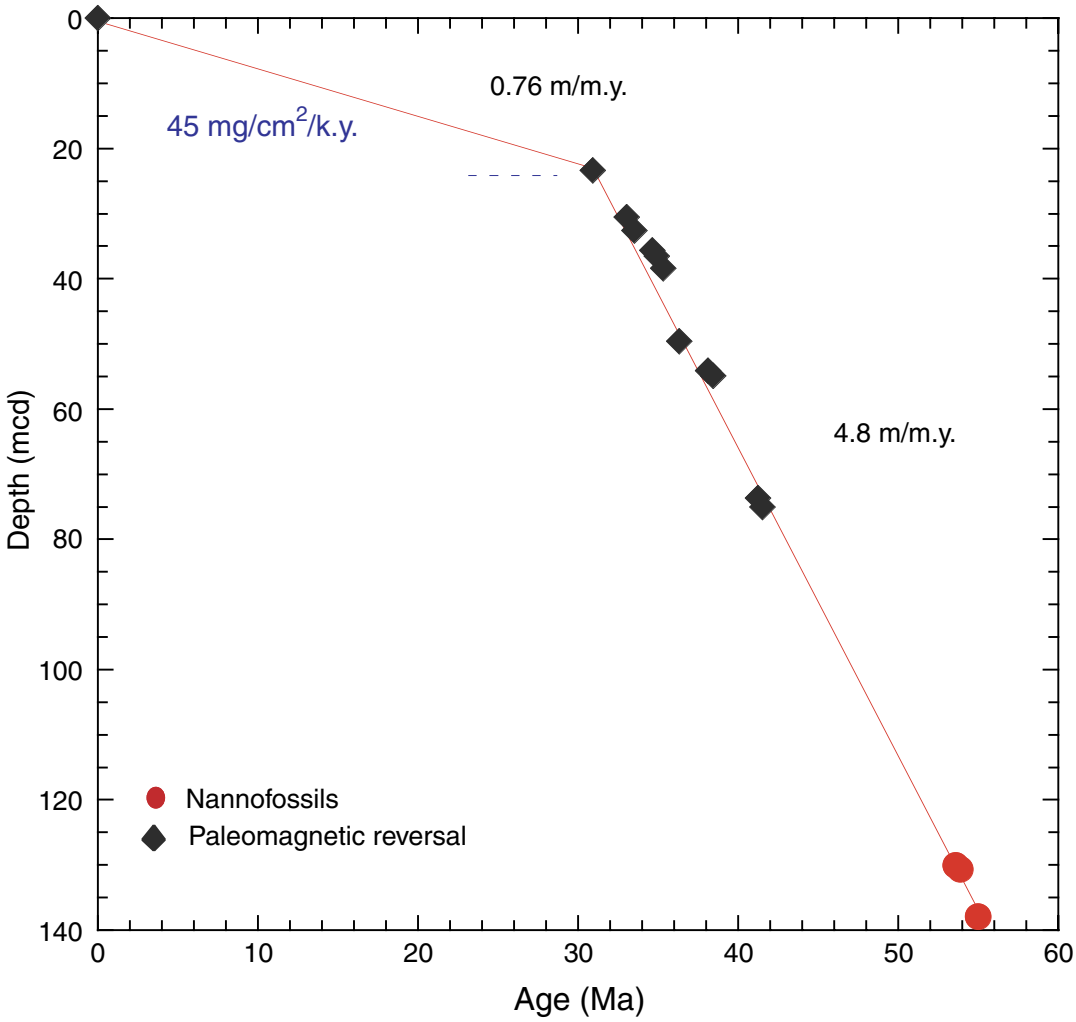

Figure F16. Density record of site survey core EW9709-4P compared with the spliced GRA density record of Site 1217.

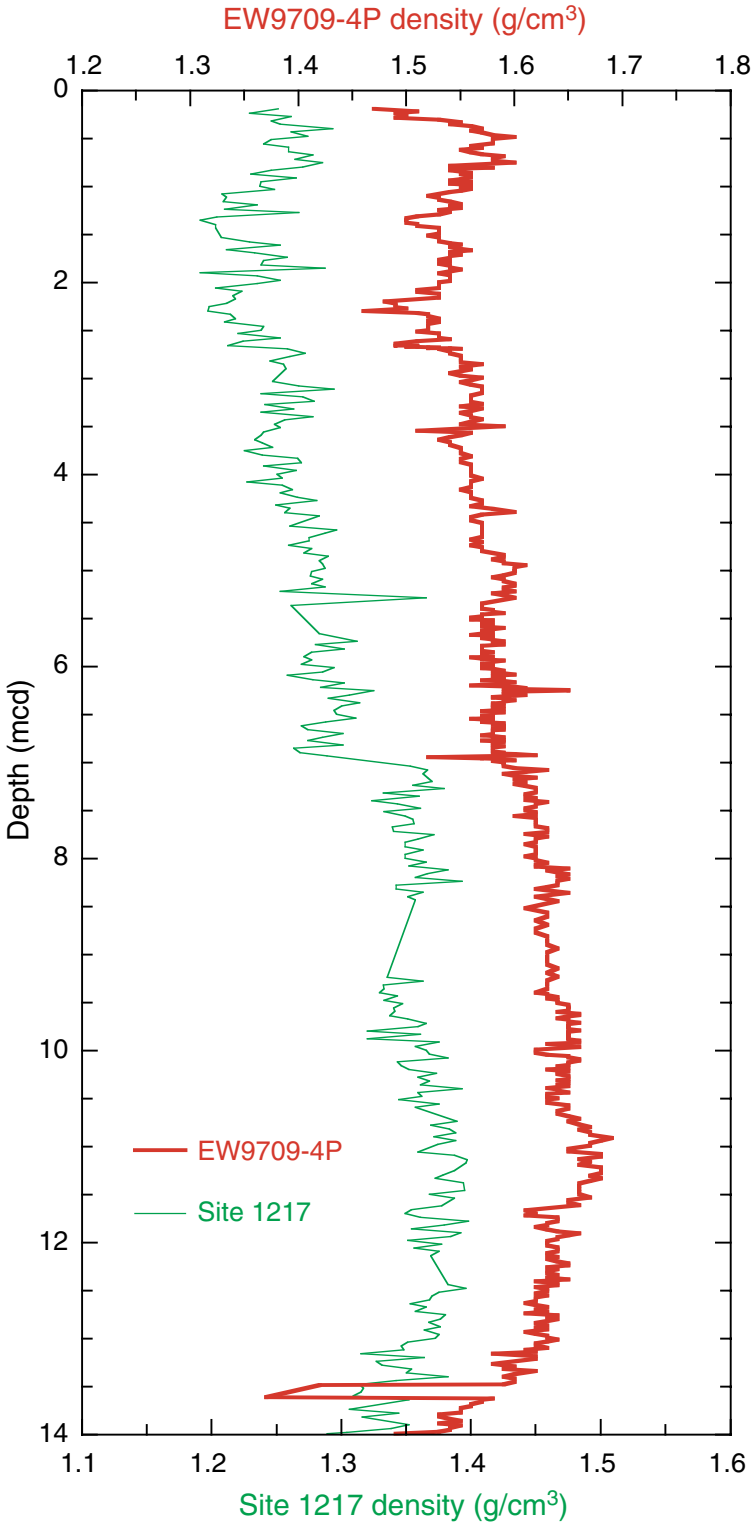

Figure F17. Expanded plot of biostratigraphic and paleomagnetic datum levels (see Tables T7, p. 54, and T8, p. 55) for the early Eocene–early Oligocene part of the geologic record. Paleomagnetic reversals and nannofossil datums are used to constrain average LSR vs. depth. Individual symbols represent different types of stratigraphic datums: solid circle = nannofossils datums, solid triangle = radiolarian datum, solid diamond = paleomagnetic reversal. Solid line segments = linear regressions of selected data points with the slope of these lines indicating sedimentation rates in m/m.y., as shown next to each segment. MARs are shown as values in mg/cm²/k.y. (see Table T9, p. 56).

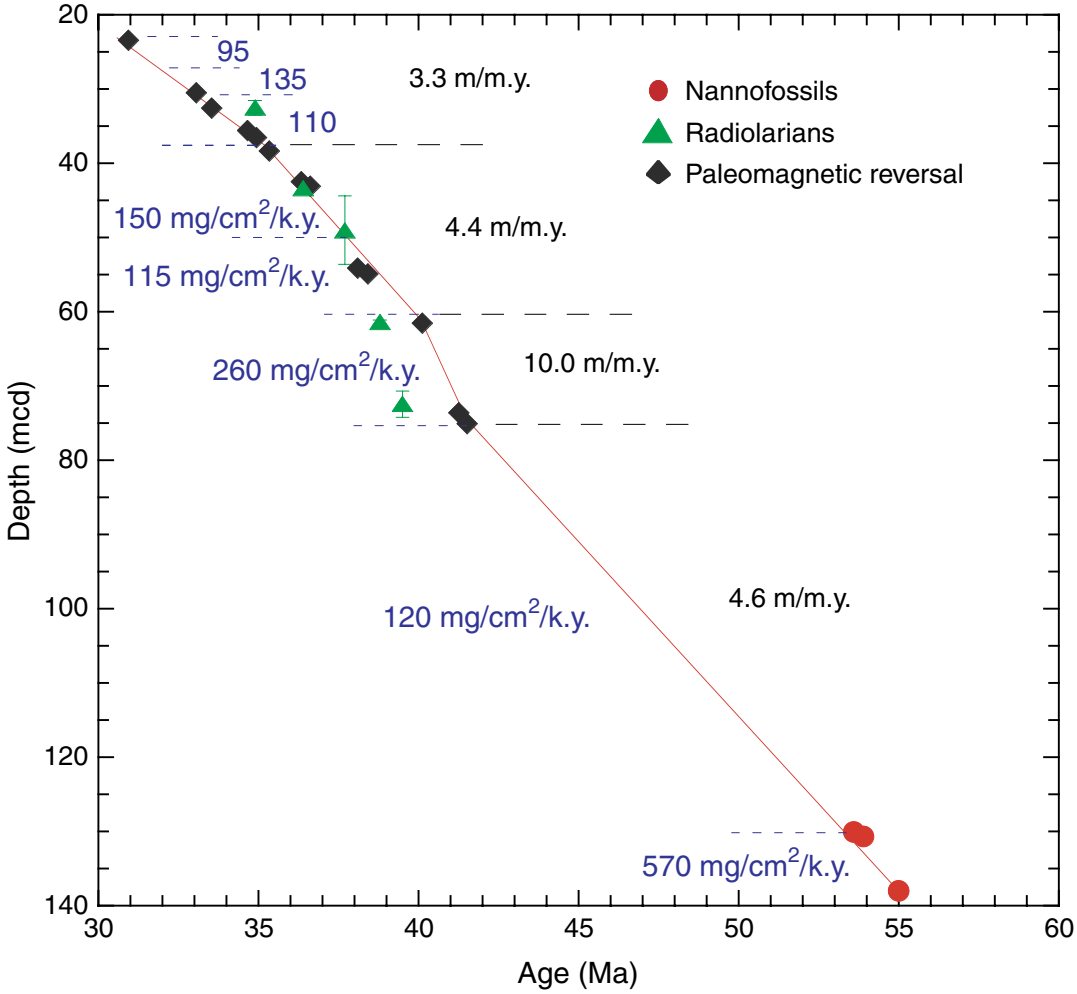

Figure F18. Interstitial water data from Site 1217. Solid circles = Ca, crosses = Mg.

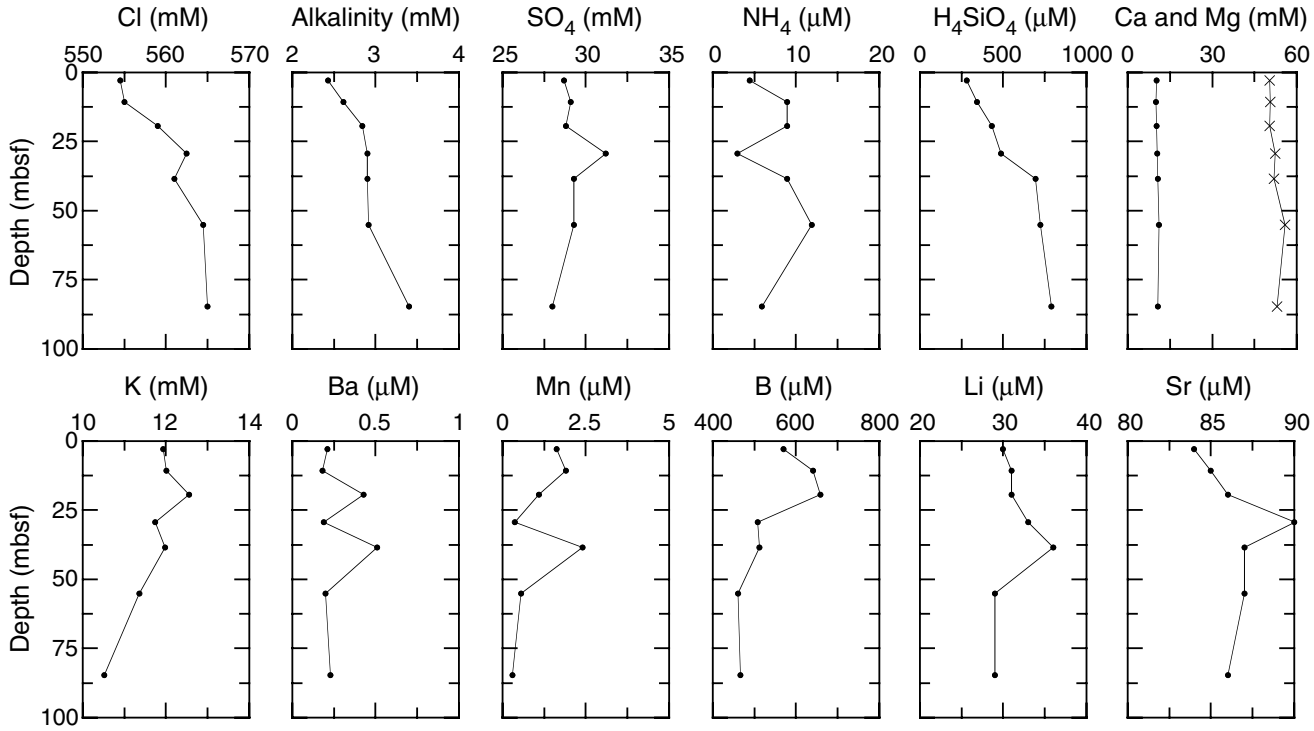

Figure F19. Bulk-sediment data from Site 1217. The high Ca value of 41.53 wt% at 129 cm cannot be accurate because 100 wt% $CaCO_3$ would be equivalent to 40 wt% Ca (see **"Geochemistry,"** p. 20, in the "Explanatory Notes" chapter).

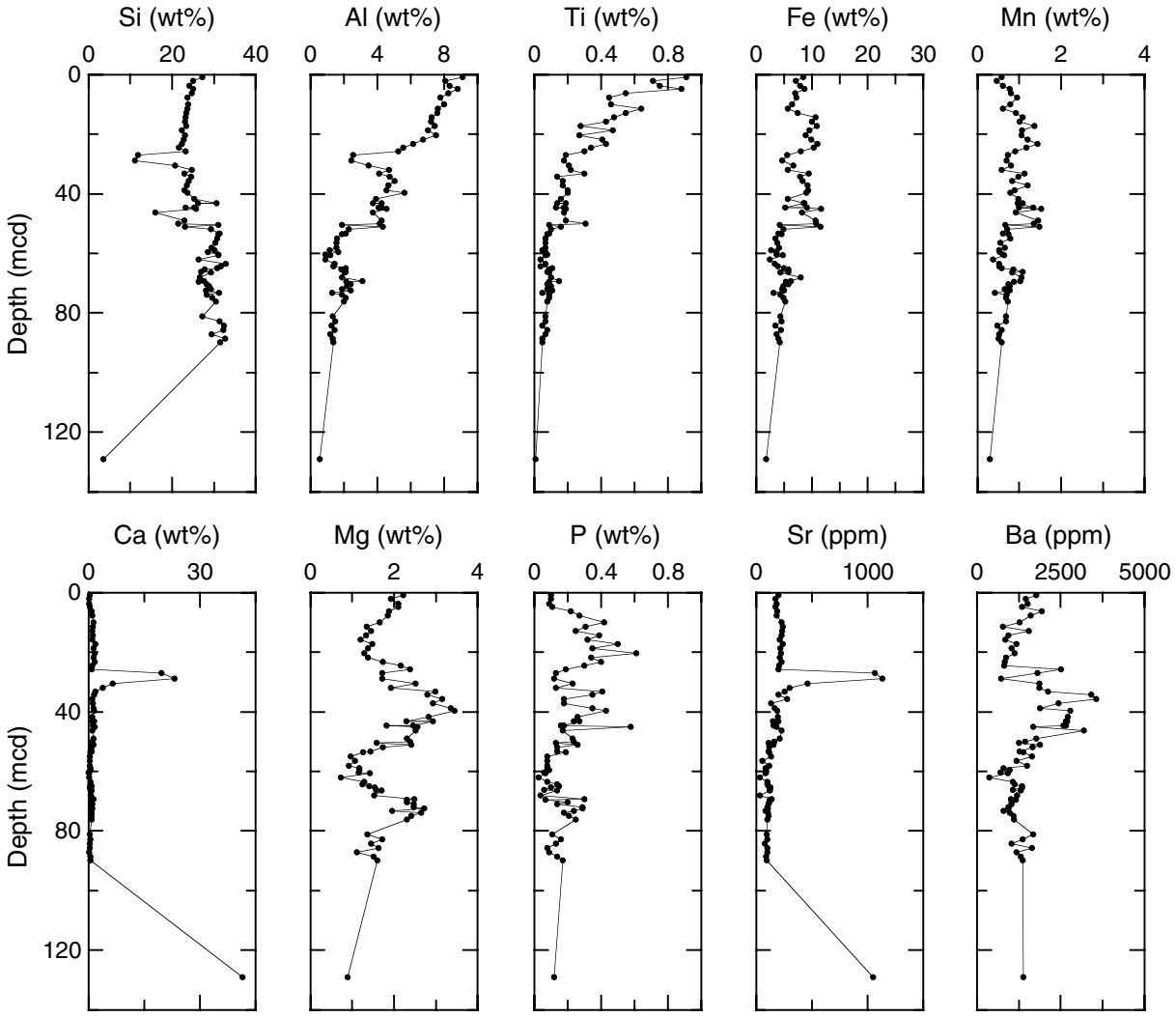

Figure F20. MAD measurements at Site 1217. **A.** Porosity (circles) and water content (squares) for Holes 1217A (solid symbols) and 1217B (open symbols). **B.** Discrete-sample wet bulk density for Holes 1217A (open circles) and 1217B (open squares) and gamma ray attenuation (GRA) bulk density for Holes 1217A (solid line), 1217B (dashed line), and 1217C (dashed line). **C.** Grain density for Holes 1217A (solid symbols) and 1217B (open symbols). Lithologic Units I–IV are noted on the right side of the figure.

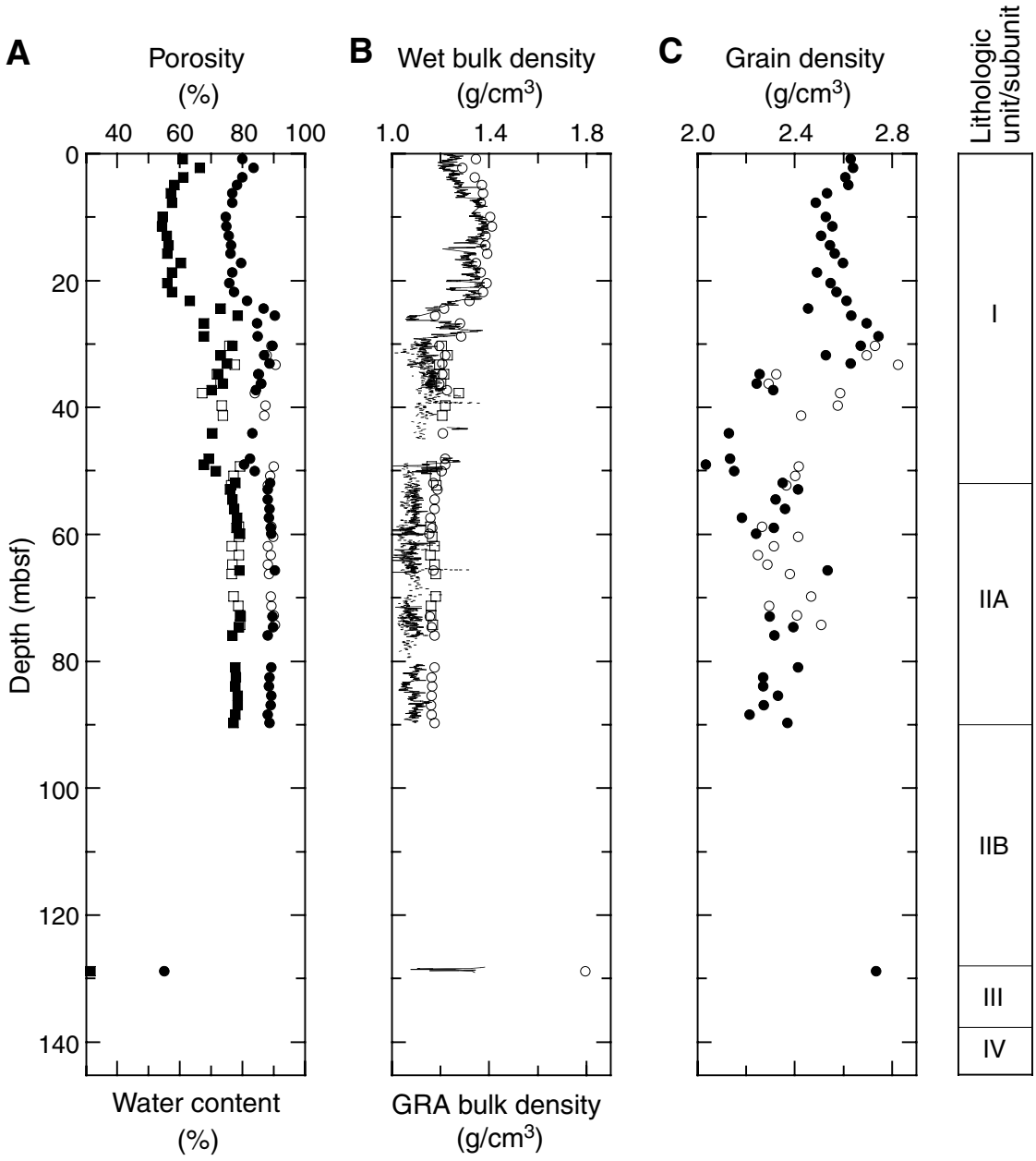

Figure F21. (A) Wet and (B) dry bulk density from discrete samples at Site 1217 plotted with gamma ray attenuation (GRA) density interpolated with a 20-cm-wide Gaussian window.

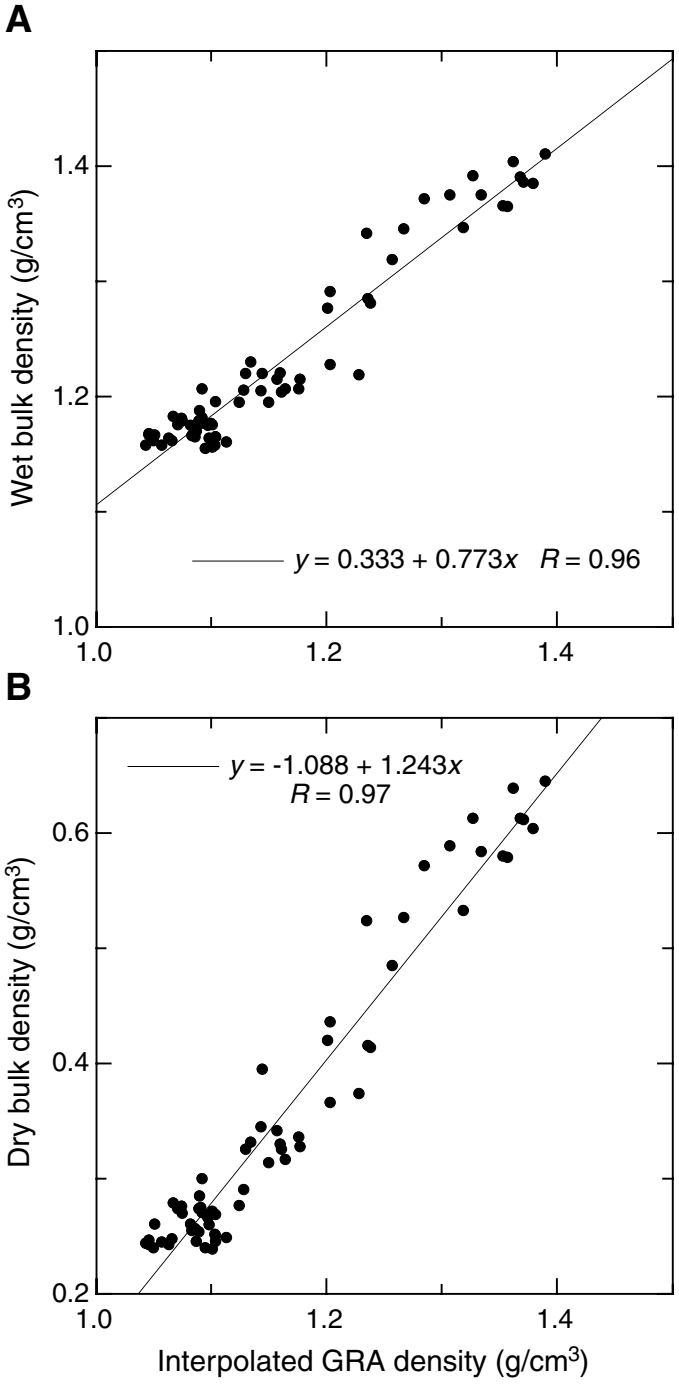

Figure F22. LAS mineralogy determinations for Hole 1217A. Lithologic Units I–IV and relative ages are noted to the left of the figure.

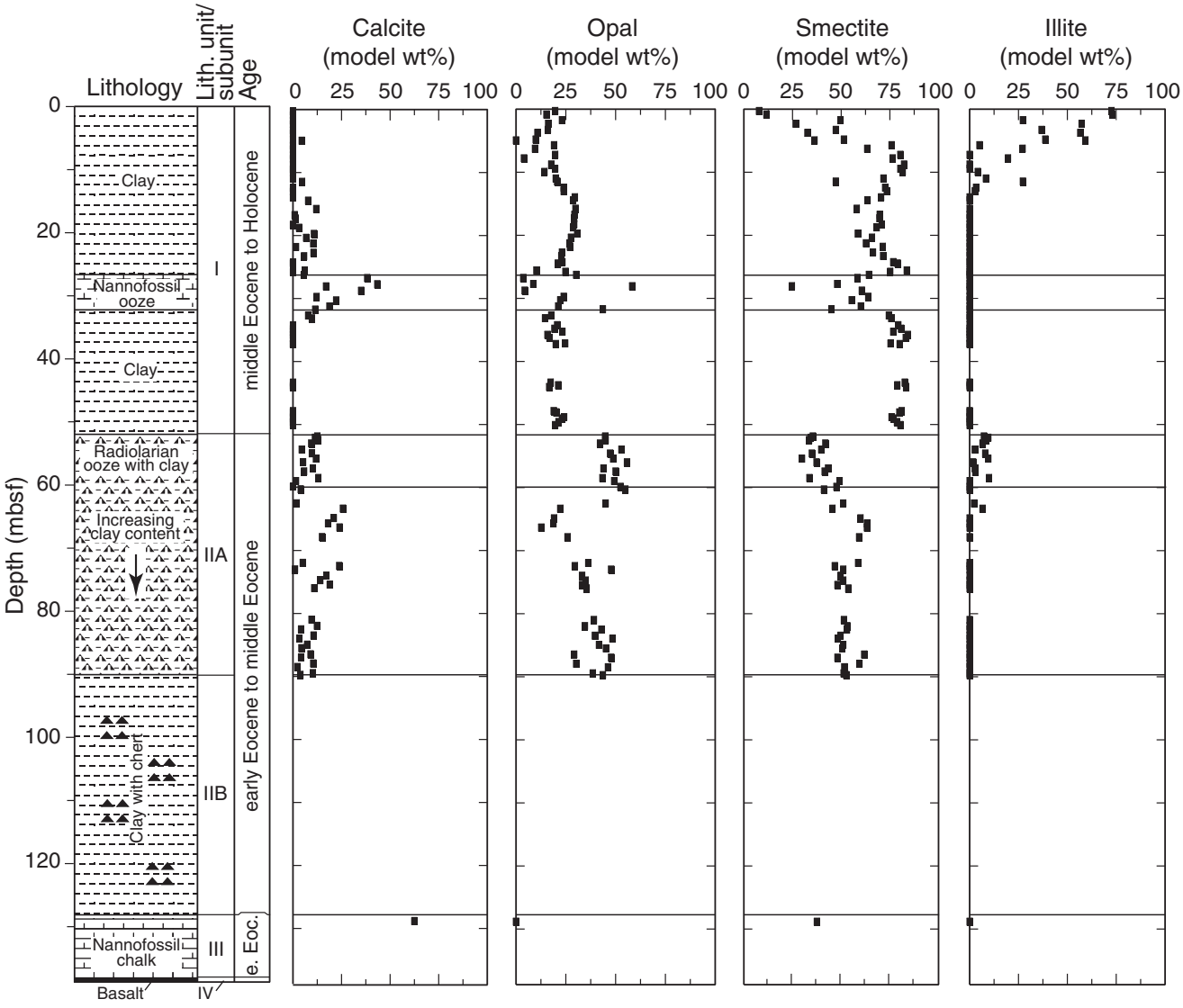

Figure F23. Compressional wave velocity from the PWL from Holes 1217A (line), 1217B (upper dashed line), and 1217C (lower dashed line). Transverse velocity measurements of the insertion (open symbols) and contact probe (solid symbols) systems for Holes 1217A (circles) and 1217B (squares). Lithologic Units I–IV are noted on the right side of the figure.

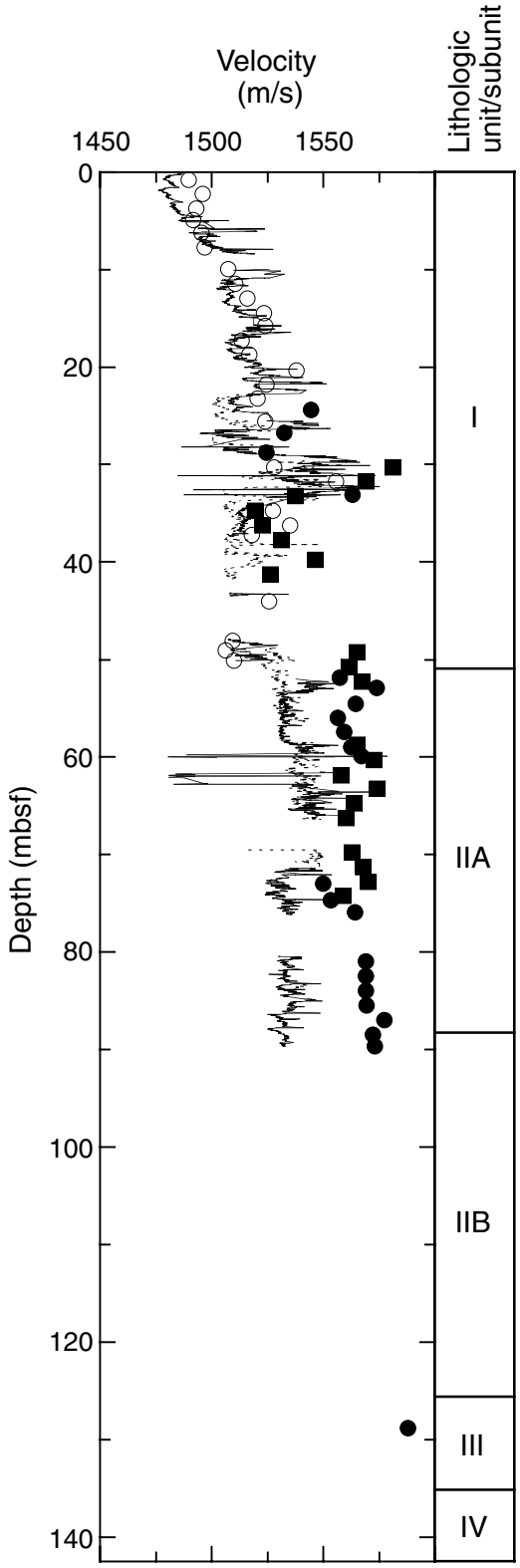

Figure F24. Natural gamma radiation for Holes 1217A (solid line), 1217B (upper dashed line), and 1217C (lower dashed line). Lithologic Units I–IV are noted on the right side of the figure. cps = counts per second.

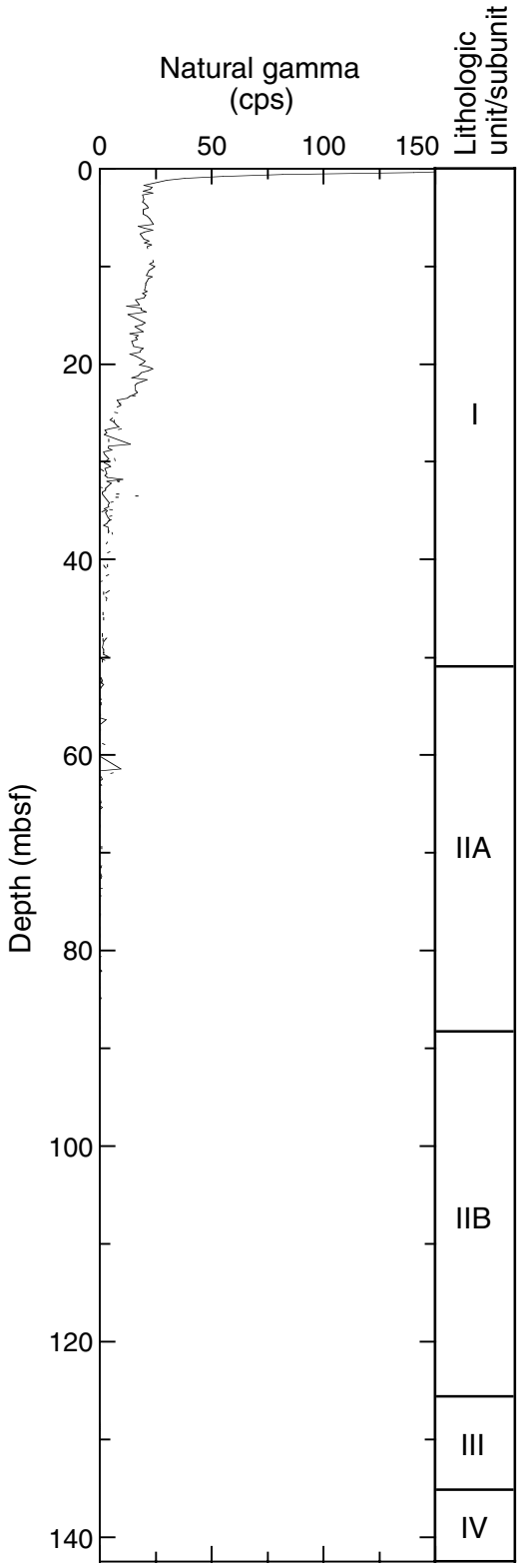

Figure F25. Magnetic susceptibility for Holes 1217A (solid line), 1217B (upper dashed line), and 1217C (lower dashed line). Lithologic Units I–IV are noted on the right side of the figure.

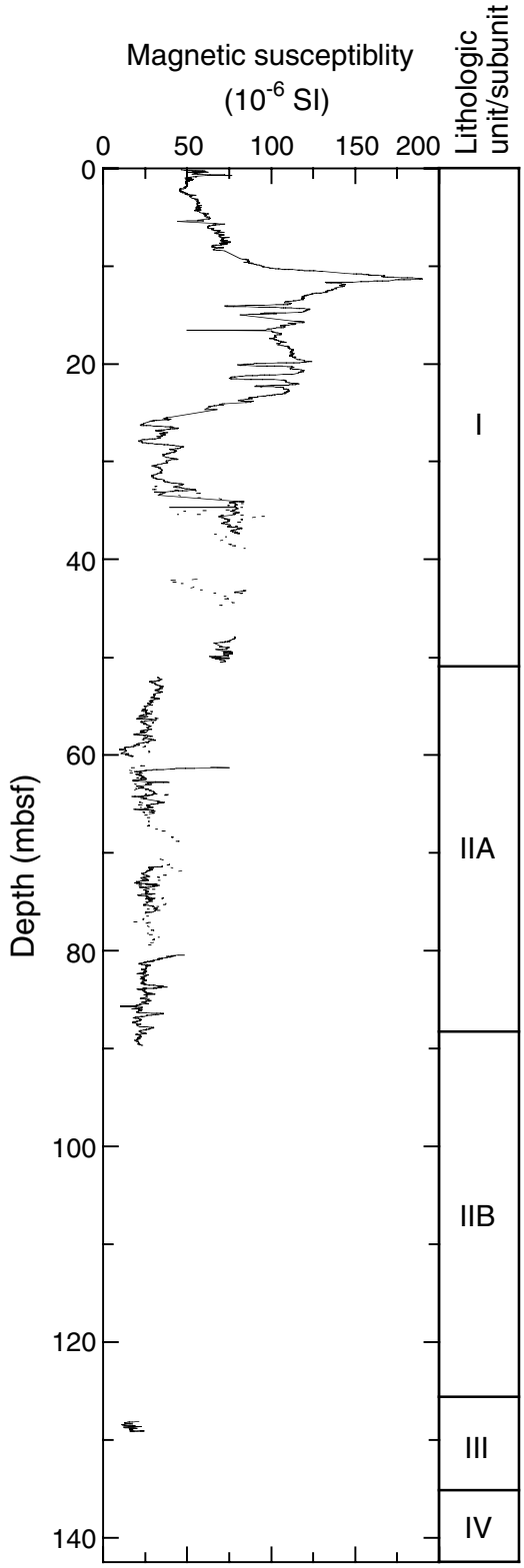

Table T1. Coring summary, Site 1217. (See table note. Continued on next page.)

Hole 1217A
Latitude: 16°52.0133′N
Longitude: 138°5.9981′W
Time on site (hr): 79.25 (1815 hr, 8 Nov–0130 hr, 12 Nov 2001)
Time on hole (hr): 45.00 (1815 hr, 8 Nov–1515 hr, 10 Nov 2001)
Seafloor (drill pipe measurement from rig floor, mbrf): 5353.0
Distance between rig floor and sea level (m): 10.9
Water depth (drill pipe measurement from sea level, m): 5342.1
Total depth (drill pipe measurement from rig floor, mbrf): 5498.2
Total penetration (meters below seafloor, mbsf): 145.20
Total length of cored section (m): 145.2
Total core recovered (m): 89.94
Core recovery (%): 61.9
Total number of cores: 17
Total number of drilled intervals: 0

Hole 1217B
Latitude: 16°52.0175′N
Longitude: 138°6.0007′W
Time on hole (hr): 15.00 (1515 hr, 10 Nov–0615 hr, 11 Nov 2001)
Seafloor (drill pipe measurement from rig floor, mbrf): 5353.0
Distance between rig floor and sea level (m): 10.9
Water depth (drill pipe measurement from sea level), m: 5342.10
Total depth (drill pipe measurement from rig floor, mbrf): 5439.5
Total penetration (meters below seafloor, mbsf): 86.5
Total length of cored section (m): 66.5
Total length of drilled intervals (m): 20.0
Total core recovered (m): 61.49
Core recovery (%): 92.5
Total number of cores: 7
Total number of drilled intervals: 1

Hole 1217C
Latitude: 16°52.023′N
Longitude: 138°6.001′W
Time on hole (hr): 19.25 (0615 hr, 11 Nov–0130 hr, 12 Nov 2001)
Seafloor (drill pipe measurement from rig floor, mbrf): 5353.0
Distance between rig floor and sea level (m): 10.9
Water depth (drill pipe measurement from sea level, m): 5342.1
Total depth (drill pipe measurement from rig floor, mbrf): 5432.5
Total penetration (meters below seafloor, mbsf): 79.5
Total length of cored section (m): 47.5
Total length of drilled intervals (m): 32.0
Total core recovered (m): 46.82
Core recovery (%): 98.6
Total number of cores: 5
Total number of drilled intervals: 1

Core	Date (Nov 2001)	Local time (hr)	Depth (mbsf) Top	Depth (mbsf) Bottom	Length (m) Cored	Length (m) Recovered	Recovery (%)
199-1217A-							
1H	9	0710	0.0	5.5	5.5	5.50	100.0
2H	9	0825	5.5	15.0	9.5	9.80	103.2
3H	9	1000	15.0	24.5	9.5	10.13	106.6
4H	9	1120	24.5	34.0	9.5	9.10	95.8
5H	9	1240	34.0	43.5	9.5	10.18	107.2
6H	9	1345	43.5	50.7	7.2	7.25	100.7
7H	9	1500	50.7	60.2	9.5	9.78	102.9
8H	9	1600	60.2	61.2	1.0	0.64	64.0
9H	9	1720	61.2	70.7	9.5	7.16	75.4
10H	9	1830	70.7	80.2	9.5	5.74	60.4
11H	9	1945	80.2	89.7	9.5	10.05	105.8
12H	9	2050	89.7	99.2	9.5	0.84	8.8
13X	10	0110	99.2	108.9	9.7	0.29	3.0
14X	10	0415	108.9	118.5	9.6	0.13	1.4
15X	10	0715	118.5	128.1	9.6	0.30	3.1
16X	10	1020	128.1	137.7	9.6	2.83	29.5
17X	10	1400	137.7	145.2	7.5	0.22	2.9
				Cored totals:	145.2	89.94	61.9

Table T1 (continued).

Core	Date (Nov 2001)	Local time (hr)	Depth (mbsf) Top	Depth (mbsf) Bottom	Length (m) Cored	Length (m) Recovered	Recovery (%)
199-1217B-							
			*****Drilled from 0.0 to 20.3 mbsf*****				
2H	10	1735	20.0	29.5	9.5	8.46	89.1
3H	10	1855	29.5	39.0	9.5	9.92	104.4
4H	10	2020	39.0	48.5	9.5	9.84	103.6
5H	10	2140	48.5	58.0	9.5	8.11	85.4
6H	10	2310	58.0	67.5	9.5	9.20	96.8
7H	11	0150	67.5	77.0	9.5	7.55	79.5
8H	11	0310	77.0	86.5	9.5	8.41	88.5
				Cored totals:	66.5	61.49	92.5
				Drilled total:	20.0		
				Total:	86.5		
199-1217C-							
			*****Drilled from 0.0 to 32.0 mbsf*****				
2H	11	0850	32.0	41.5	9.5	9.38	98.7
3H	11	1020	41.5	51.0	9.5	9.94	104.6
4H	11	1155	51.0	60.5	9.5	9.23	97.2
5H	11	1310	60.5	70.0	9.5	8.72	91.8
6H	11	1440	70.0	79.5	9.5	9.55	100.5
				Cored totals:	47.5	46.82	98.6
				Drilled total:	32.0		
				Total:	79.5		

Note: The expanded coring summary table is available in ASCII (see the **"Supplementary Material"** contents list).

Table T2. Distribution of benthic foraminifers, Holes 1217A and 1217B.

Core, section, interval (cm)	Depth (mbsf)	Preservation	Group abundance	Bathymetry	*Abyssamina poagi*	*Abyssamina quadrata*	*Ammodiscus* sp.	*Anomalinoides semicribratus*	*Anomalinoides spissiformis*	*Aragonia velascoensis*	*Bathysiphon* spp.	*Buliminella macilenta*	*Buliminella semicostata*	*Buliminella beaumonti*	*Cibicidoides grimsdalei*	*Cibicidoides havanensis*	*Cibicidoides* spp.	*Eggerella bradyi*	*Ellipsoglandulina* sp.	*Gavelinella beccariiformis*	*Globocassidulina globosa*	*Globocassidulina* sp.	*Gyroidinoides* spp.	*Heronallenia lingulata*	*Hippocrepinella* sp.	*Lagenoglandulina* sp.	*Lockhartia cylindrica*	*Nodogenerina bradyi*	*Nodosarella tuberosa*	*Nuttallides truempyi*	*Nuttallides umbonifera*	*Oridorsalis umbonatus*	*Placentammina compianata*	*Pullenia coryelli*	*Pullenia eocaenica*	*Pullenia jarvisi*	*Pyrulina* spp.	*Rhizammina* sp.	*Siphonodosaria abyssorum*	*Spiroplectammina spectabilis*	*Subreophax* sp.	*Tappanina selmensis*	*Textularia* spp.	*Thalmannammina simplex*	*Thalmannammina subturbinata*	*Turrilina robertsi*	Unidentified benthic forams	Unilocular species
199-1217A-																																														
1H-CC, 20–25	5.45		B																																											
2H-CC, 12–20	15.22		B																																											
3H-CC, 17–23	25.07		B																																											
4H-2, 114–116	27.14	VG	A	A				R						R	F	R		R	R			A	F	T		R		R			C	F		R		T					R			R		
4H-3, 27–29	27.77	VG	A	A												F		R				A						R	R			F				T								R		
4H-4, 10–12	28.10	VG	A	A												F							R						R	R					F		C								R		
4H-6, 51–53	31.51	VG	C	A							F			R	F		F					C										R			R									R		
4H-7, 107–110	33.57	P	F	A			A																																						R		
5H-CC, 20–30	44.08	P	F	A			C				C																										C							R	F	R		
6H-CC, 8–18	50.65	P	F	A			C				F																										C							F		R		
7H-CC, 13–21	60.40		B																																												
9H-CC, 9–14	68.31		B																																												
10H-CC, 17–22	76.39		B																																												
11H-CC, 26–31	90.20		B																																												
12H-1, 0–5	89.70		B																																												
15X-1, 29–30	118.79		B																																												
16X-2, 19–20	129.43	VG	F	A		F			F				F	F							F									C		R												R	R	
17X-CC, 0–1	137.70	VG	C	A	R	C			R	T			R	R			R			T	R		R							C				T										R		
199-1217B-																																															
2H-CC, 17–22	28.41	G	A	A	R									R	F	R							R		R										R			F	R	T				R	R	
3H-CC, 22–32	39.32	P	A	A			F																				R						R			F			R				R		
4H-CC, 10–15	48.79						R				F																										C							C		C		
5H-CC, 13–18	56.56		B																																												
6H-CC, 0–10	67.10		B																																												
7H-CC, 16–21	75.00		B																																												
8H-CC, 0–8	85.33		B																																												

Notes: Preservation: VG = very good, G = good, P = poor. Abundance: A = abundant, C = common, F = few, R = rare, T = trace, B = barren. Bathymetry: A = abyssal.

Table T3. Composite depths of identified geomagnetic reversals, Site 1217.

	Chron/ Subchron	Depth (mcd)	Age* (Ma)
B	C12n	23.47	30.939
T	C13n	27.90	33.058
B	C13n	29.88	33.545
T	C15n	32.83	34.655
B	C15n	33.98	34.940
T	C16n.1n	36.38	35.343
B	C16n.1n	37.93	35.526
T	C16n.2n	39.24	35.685
B	C17n	53.53	38.113
T	C18n	54.85	38.426
B	C18n	62.24	40.130
T	C19n	73.57	41.257
B	C19n	75.05	41.521
T	C20n	80–81.95	42.536

Notes: * = Cande and Kent (1995). T = top, B = bottom. This table is also available in **ASCII.**

Table T4. Core disturbance, Site 1217.

Core, section, interval (cm)	Depth (mbsf) Top	Depth (mbsf) Bottom	Comments
199-1217A-			
1H-1, 0–13	0.00	0.13	Flow-in (Mn nodule at top)
2H-1, 0–15	5.50	5.65	Flow-in
2H-3, 0–71	8.50	9.21	Split liner (data not culled)
3H-1, 0–60	15.00	15.60	Flow-in
4H-1, 0–13	24.50	24.63	Disturbance (intense)
4H-1, 19–67	24.69	25.17	Disturbance (intense)
4H-1, 67–99	25.17	25.49	Disturbance (intense)
4H-7, 93–109	33.43	33.59	Disturbance (intense)
5H-3, 40–51	37.40	37.51	Disturbance (intense)
5H-3, 51–61	37.51	37.61	Chert (large nodule)
5H-3, 77–86	37.77	37.86	Soupy
5H-3, 61–150	37.61	38.50	Flow-in
5H-4, 0–150	38.50	40.00	Flow-in
5H-5, 0–150	40.00	41.50	Flow-in
5H-6, 0–150	41.50	43.00	Flow-in
5H-7, 0–14	43.00	43.14	Flow-in
6H-1, 0–109	43.50	44.59	Chert
6H-2, 0–150	44.59	46.09	Flow-in
6H-3, 0–150	46.09	47.59	Flow-in
6H-4, 0–30	47.59	47.89	Flow-in
6H-5, 0–20	48.59	48.79	Flow-in (very disturbed)
6H-5, 22–30	48.81	48.89	Soupy
6H-5, 60–67	49.19	49.26	Soupy
7H-1, 0–130	50.70	52.00	Flow-in (soupy at 86 cm)
8H-1, 0–38	60.20	60.58	Downhole debris
8H-1, 38–63	60.58	60.83	Highly disturbed/downhole debris?
9H-4, 141–150	66.00	66.09	Soupy
9H-5, 0–150	66.09	67.59	Soupy
9H-6, 0–63	67.59	68.22	Soupy
9H-CC, 0–14	68.22	68.36	Disturbed
10H-1, 0–65	70.70	71.35	Soupy
11H-1, 0–23	80.20	80.43	Soupy
12H-1, 0–84	89.70	90.54	Downhole debris (chert)
13X-CC, 0–29	99.20	99.49	Chert
14X-CC, 0–13	108.90	109.03	Chert
15X-1, 0–30	118.50	118.80	Chert
16X-2, 0–150	129.24	130.74	Chert
16X-CC, 0–19	130.74	130.93	Chert
17X-CC, 0–29	137.70	137.99	Basalt
199-1217B-			
2H-1, 0–150	20.00	21.50	Flow-in
2H-2, 0–135	21.50	22.85	Flow-in
3H-1, 0–3	29.50	29.53	Soupy
3H-1, 11–23	29.61	29.73	Crack
3H-2, 48–49	31.48	31.49	Crack
3H-3, 114–115	33.64	33.65	Crack
3H-4, 42–45	34.42	34.45	Crack
3H-6, 107–120	38.07	38.20	Chert
4H-2, 133–150	41.83	42.00	Flow-in
4H-3, 0–150	42.00	43.50	Flow-in
4H-4, 0–149	43.50	44.99	Flow-in
4H-5, 0–149	45.00	46.49	Flow-in
4H-6, 0–148	46.50	47.98	Flow-in
4H-7, 0–68	48.00	48.68	Flow-in
5H-1, 0–30	48.50	48.80	Chert fragments
5H-CC, 7–12	56.50	56.55	Disturbed
6H-1, 0–40	58.00	58.40	Chert breccia
7H-1, 0–150	67.50	69.00	Disturbed (very)
7H-2, 0–45	69.00	69.45	Chert breccia (soupy)
8H-1, 0–150	77.00	78.50	Chert breccia (disturbed)
8H-2, 0–150	78.50	80.00	Disturbed
8H-3, 0–150	80.00	81.50	Disturbed
8H-4, 0–150	81.50	83.00	Disturbed
8H-5, 0–30	83.00	83.30	Disturbed/flow-in
8H-5, 100–150	84.00	84.50	Flow-in
8H-6, 0–83	84.50	85.33	Flow-in
199-1217C-			
2H-1, 0–50	32.00	32.50	Downhole debris
2H-5, 90–150	38.90	39.50	Flow-in
2H-6, 0–100	39.50	40.50	Flow-in
2H-7, 0–69	40.50	41.19	Flow-in
2H-CC, 0–19	41.19	41.38	Flow-in
3H-1, 0–50	41.50	42.00	Flow-in
3H-2, 110–120	44.10	44.20	Chert
3H-3, 60–150	45.10	46.00	Flow-in, chert
3H-4, 0–150	46.00	47.50	Flow-in, chert
3H-5, 0–150	47.50	49.00	Flow-in
3H-6, 0–150	49.00	50.50	Flow-in
3H-7, 0–70	50.50	51.20	Flow-in
3H-CC, 0–26	51.18	51.44	Flow-in
4H-1, 0–150	51.00	52.50	Flow-in
4H-2, 0–150	52.50	54.00	Flow-in
4H-3, 0–150	54.00	55.50	Flow-in
4H-5, 0–60	57.00	57.60	Flow-in
5H-1, 0–56	60.50	61.06	Flow-in
6H-1, 0–60	70.00	70.60	Flow-in, chert
6H-3, 31–32	73.31	73.32	Void

Notes: Data from these intervals were removed from the GRA bulk density, MS, color reflectance, natural gamma, and *P*-wave velocity data sets presented in this chapter. This table is also available in **ASCII.**

Table T5. Composite depths, Site 1217.

Core	Length (m)	Depth (mbsf)	Offset (m)	Depth (mcd)
199-1217A-				
1H	5.5	0.00	0.00	0.00
2H	9.5	5.50	0.00	5.50
3H	9.5	15.00	0.00	15.00
4H	9.5	24.50	0.26	24.76
5H	9.5	34.00	2.50	36.50
6H	7.2	43.50	1.01	44.51
7H	9.5	50.70	0.82	51.52
9H	9.5	61.20	2.35	63.55
10H	9.5	70.70	1.56	72.26
11H	9.5	80.20	1.56	81.76
16X	9.6	128.10	1.56	129.66
199-1217B-				
2H	9.5	20.00	0.02	20.02
3H	9.5	29.50	2.46	31.96
4H	9.5	39.00	3.42	42.42
5H	9.5	48.50	1.08	49.58
6H	9.5	58.00	2.85	60.85
7H	9.5	67.50	2.38	69.88
8H	9.5	77.00	2.38	79.38
199-1217C-				
2H	9.5	32.00	0.72	32.72
3H	9.5	41.50	0.72	42.22
4H	9.5	51.00	–2.18	48.82
5H	9.5	60.50	1.05	61.55
6H	9.5	70.00	0.42	70.42

Note: This table is also available in **ASCII.** [**N1**]

Table T6. Splice tie points, Site 1217.

Hole, core, section, interval (cm)	Depth (mbsf)	Depth (mcd)		Hole, core, section, interval (cm)	Depth (mbsf)	Depth (mcd)
199-				199-		
1217A-1H-CC, 18	5.43	5.43	Append to	1217A-2H-1, 0	5.50	5.50
1217A-2H-7, 128	14.98	14.98	Append to	1217A-3H-1, 0	15.00	15.00
1217A-3H-6, 60	23.10	23.10	Tie to	1217B-2H-3, 8	23.08	23.10
1217B-2H-5, 116	27.16	27.18	Tie to	1217A-4H-2, 92	26.92	27.18
1217A-4H-7, 52	33.02	33.28	Tie to	1217B-3H-1, 132	30.82	33.28
1217B-3H-7, 54	39.04	41.50	Append to	1217B-4H-1, 0	39.00	42.42
1217B-4H-2, 132	41.82	45.24	Append to	1217B-5H-1, 0	48.50	49.58
1217B-5H-5, 128	55.78	56.86	Tie to	1217A-7H-4, 84	56.04	56.86
1217A-7H-7, 48	60.18	61.00	Append to	1217B-6H-1, 0	58.00	60.85
1217B-6H-7, 54	67.05	69.90	Append to	1217C-6H-1, 0	70.00	70.42
1217C-6H-7, 44	79.44	79.86	Append to	1217A-11H-1, 0	80.20	81.76
1217A-11H-7, 48	89.68	91.24				

Note: This table is also available in **ASCII.**

Table T7. Paleomagnetic events used for LSR calculations, Site 1217.

	Chron	Age (Ma)	Depth (mcd)
B	C12N	30.939	23.47
T	C13N	33.058	27.90
B	C13N	33.545	29.88
T	C15N	34.655	32.83
B	C15N	34.940	33.98
T	C16N	35.343	36.78
B	C16N	36.341	45.90
T	C17N	36.618	48.00
B	C17N	38.113	53.53
T	C18N	38.426	54.85
B	C18N	40.130	62.24
T	C19N	41.257	73.57
B	C19N	41.521	75.05

Notes: T = top, B = bottom. Paleomagnetic reversals given as that depth at which the inclination crosses zero (see **"Paleomagnetism,"** p. 12). This table is also available in **ASCII.**

Table T8. Nannofossil and radiolarian events used for LSR calculations, Site 1217.

Marker species/ Zonal boundaries	Age (Ma)	Depth (mcd)	± (m)
Nannofossil events:			
B *Tribrachiatus contortus*	53.6	129.91	0.10
NP9/10	53.9	130.57	0.07
T *Fasciculithus tympaniformis*	55.0	135.91	1.68
Radiolarian events:			
RP19/18	34.9	32.46	0.38
RP18/17	36.4	44.20	1.12
RP17/16	37.7	50.18	1.65
RP16/15	38.8	61.40	0.19
RP15/14	39.5	72.44	0.89

Notes: T = top, B = bottom. Biostratigraphic events are noted with the depth of the sample and the range of that sample (see **"Biostratigraphy,"** p. 9). This table is also available in **ASCII.**

Table T9. Linear sedimentation rates (LSRs), dry bulk density (DBD), and mass accumulation rates (MARs) for major lithologic units, Site 1217.

Interval (mcd)	Facies	LSR (m/m.y.)	DBD (g/cm^3)	MAR ($mg/cm^2/k.y.$)
0–9	Clay	0.76	0.53	40
9–22.5	Clay	0.76	0.60	46
22.5–26	Clay	3.30	0.29	96
26–29.75	Calcareous ooze	3.30	0.41	135
29.75–38	Clay	3.30	0.34	112
38–52	Clay	4.40	0.34	150
52–61	Radiolarian ooze	4.40	0.26	114
61–76	Radiolarian ooze	10.00	0.26	260
76–130	Radiolarian ooze	4.60	0.26	120
130–135	Chalk	4.60	1.23	566

Notes: Control points for LSR values are shown in Tables **T7,** p. 54, and **T8,** p. 55., and Figures **F15,** p. 36, and **F17,** p. 37. Sedimentary unit DBD values are compiled from Table **T13,** p. 61 (see **"Physical Properties,"** p. 18). For more information on the major lithologic units see **"Lithostratigraphy,"** p. 6. This table is also available in **ASCII.**

Table T10. Interstitial water data, Hole 1217A.

Core, section, interval (cm)	Depth (mbsf)	pH	Alkalinity (mM)	Salinity	Cl (mM)	Na (mM)	K (mM)	Ca (mM)	Mg (mM)	SO_4 (mM)	NH_4 (μM)	H_4SiO_4 (μM)	Sr (μM)	Li (μM)	Mn (μM)	Ba (μM)	B (μM)
199-1217A-																	
1H-2, 145–150	2.95	7.20	2.43	35.0	555	481.0	11.9	10.2	50.5	28.7	4.5	281	84	30	1.62	0.21	570
2H-4, 145–150	10.65	7.20	2.61	35.0	555	482.2	12.0	10.1	50.7	29.1	8.9	345	85	31	1.91	0.18	640
3H-3, 145–150	19.45	7.22	2.85	35.0	559	485.4	12.6	10.4	50.4	28.8	8.9	431	86	31	1.10	0.43	659
4H-4, 145–150	29.45	7.37	2.90	35.0	562	490.4	11.8	10.6	52.3	31.2	3.0	489	90	33	0.37	0.19	508
5H-3, 145–150	38.45	7.31	2.90	35.0	561	485.5	12.0	10.6	51.9	29.3	8.9	695	87	36	2.41	0.51	512
7H-3, 145–150	55.15	7.32	2.92	36.0	564	480.5	11.4	11.2	55.9	29.3	11.9	723	87	29	0.55	0.20	461
11H-3, 145–150	84.65	7.32	3.40	35.0	565	486.2	10.5	10.8	53.0	28.0	5.9	789	86	29	0.30	0.23	466

Note: This table is also available in **ASCII.**

Table T11. Bulk sediment data, Holes 1217A and 1217B. (See table notes. Continued on next page.)

Core, section, interval (cm)	Depth (mbsf)	Depth (mcd)	Si (wt%)	Al (wt%)	Ti (wt%)	Fe (wt%)	Mn (wt%)	Ca (wt%)	Mg (wt%)	P (wt%)	Sr (ppm)	Ba (ppm)
199-1217A-												
1H-1, 79–80	0.79	0.79	27.29	9.11	0.91	5.96	0.58	0.44	2.22	0.10	201.93	1777.69
1H-2, 72–73	2.22	2.22	25.01	8.08	0.71	5.04	0.47	0.23	1.93	0.10	175.41	1455.89
1H-3, 73–74	3.73	3.73	24.15	8.31	0.75	5.53	0.62	0.27	2.11	0.09	186.83	1522.89
1H-4, 38–39	4.88	4.88	25.02	8.82	0.88	6.07	0.78	0.37	2.10	0.11	173.83	1343.99
2H-1, 74–75	6.24	6.24	24.69	8.25	0.55	4.96	0.80	0.92	1.89	0.22	189.28	1935.22
2H-2, 74–75	7.74	7.74	23.68	7.76	0.45	5.06	0.95	1.01	1.85	0.27	188.09	1609.20
2H-4, 74–75	9.94	9.94	23.89	7.98	0.46	4.50	0.79	1.37	1.67	0.42	230.55	1281.01
2H-5, 74–75	11.44	11.44	23.76	7.61	0.64	4.02	0.62	1.29	1.35	0.31	240.65	783.29
2H-6, 74–75	12.94	12.94	23.37	7.59	0.55	5.22	0.92	1.09	1.46	0.25	236.50	1549.54
2H-7, 73–74	14.43	14.43	23.22	7.27	0.48	7.48	1.09	1.25	1.34	0.39	229.91	950.25
3H-1, 74–75	15.74	15.74	23.13	7.21	0.43	6.97	1.02	1.12	1.21	0.32	216.08	860.69
3H-2, 74–75	17.24	17.24	23.38	7.45	0.28	7.61	1.36	1.87	1.48	0.50	244.18	1178.08
3H-3, 74–75	18.74	18.74	22.44	7.02	0.47	6.74	1.07	1.41	1.39	0.35	217.68	1041.98
3H-4, 84–85	20.34	20.34	23.14	7.52	0.27	6.24	1.05	1.81	1.29	0.61	224.08	1120.63
3H-5, 79–80	21.79	21.79	22.79	6.73	0.41	6.92	1.21	1.40	1.39	0.34	215.10	867.97
3H-6, 73–74	23.23	23.23	22.44	6.16	0.43	7.73	1.44	1.71	1.73	0.40	232.65	832.40
3H-7, 42–43	24.42	24.42	21.58	5.56	0.34	7.24	1.18	1.08	2.16	0.30	208.59	821.89
4H-1, 106–107	25.56	25.82	23.22	5.27	0.30	5.62	0.91	0.88	2.39	0.19	203.36	2505.90
4H-2, 73–74	26.73	26.99	11.93	2.58	0.19	3.94	0.73	19.75	1.72	0.13	1065.82	1810.75
4H-4, 73–74	28.73	28.99	11.16	2.44	0.18	3.30	0.71	23.17	1.72	0.12	1133.09	716.98
4H-5, 74–75	30.24	30.50	20.79	3.49	0.21	4.70	0.80	6.58	2.52	0.23	463.71	1859.36
4H-6, 73–74	31.73	31.99	24.79	4.72	0.22	3.99	0.59	3.86	1.93	0.13	302.28	1874.27
4H-7, 58–59	33.08	33.34	22.95	4.12	0.30	6.61	1.13	1.92	2.99	0.41	258.53	2134.23
5H-1, 74–75	34.74	37.24	23.60	4.66	0.17	6.47	1.21	1.28	2.93	0.18	136.29	2440.15
5H-2, 74–75	36.24	38.74	22.93	4.57	0.20	6.57	0.89	1.36	3.36	0.35	168.60	1879.90
5H-3, 23–24	37.23	39.73	23.70	5.62	0.20	6.29	0.79	1.56	3.45	0.43	193.74	2792.77
5H-4, 74–75	39.24	41.74	25.38	3.93	0.16	5.72	0.98	1.11	2.83	0.26	195.24	2716.19
5H-5, 74–75	40.74	43.24	26.26	4.28	0.19	8.62	0.97	1.56	2.93	0.27	200.99	2692.24
5H-6, 74–75	42.24	44.74	23.25	4.28	0.13	6.39	1.00	1.21	1.82	0.16	158.07	2589.53
5H-7, 74–75	43.74	46.24	16.01	3.76	0.18	5.76	0.93	1.08	2.52	0.17	229.61	3198.89
6H-1, 52–53	44.02	45.03	25.77	4.56	0.19	8.18	1.53	1.77	2.57	0.58	186.23	1674.55
6H-4, 45–46	48.04	49.05	22.92	4.26	0.19	7.47	1.46	1.35	2.31	0.23	213.09	1768.46
6H-5, 45–46	49.04	50.05	21.43	4.15	0.31	7.58	1.35	1.11	2.38	0.24	164.06	1449.08
6H-6, 73–74	50.04	51.05	23.17	4.36	0.16	8.13	1.49	1.36	2.41	0.26	160.86	1877.55
7H-2, 73–75	52.93	53.75	31.16	1.89	0.08	3.20	0.74	0.65	1.26	0.19	121.17	1390.57
7H-3, 81–83	54.51	55.33	30.80	1.60	0.07	2.45	0.79	0.40	0.97	0.08	134.31	1651.36
7H-4, 72–74	55.92	56.74	30.29	1.56	0.07	2.68	0.56	0.37	1.07	0.08	57.17	1191.05
7H-5, 76–78	57.46	58.28	29.51	1.57	0.07	2.87	0.66	0.48	0.92	0.08	120.00	1493.39
7H-6, 73–75	58.93	59.75	28.65	1.68	0.07	3.69	0.54	0.62	1.17	0.09	94.52	971.91
7H-7, 17–18	59.87	60.69	31.04	0.92	0.08	2.64	0.62	0.09	1.16	0.06	93.97	701.90
9H-1, 74–75	61.94	64.29	31.75	1.37	0.04	2.77	0.52	0.56	1.25	0.14	101.49	1121.32
9H-2, 74–75	62.98	65.33	27.90	1.88	0.09	4.11	0.87	0.50	1.55	0.10	130.27	1355.05
9H-3, 74–75	63.83	66.18	27.01	2.14	0.08	4.08	1.08	0.62	1.58	0.06	128.00	1077.95
9H-4, 113–114	65.72	68.07	26.69	1.89	0.10	5.64	1.06	0.77	1.53	0.04	38.12	1203.58
9H-5, 113–114	67.22	69.57	26.32	2.18	0.09	3.75	0.88	0.87	2.31	0.07	122.38	1160.77
9H-6, 35–36	67.94	70.29	28.29	2.40	0.08	4.11	0.74	0.99	2.31	0.20	121.75	1035.35
10H-1, 110–111	71.80	73.36	29.29	1.90	0.08	3.31	0.66	0.90	2.48	0.29	106.09	953.00
10H-2, 74–75	72.94	74.50	31.32	1.31	0.05	2.21	0.42	0.70	1.96	0.24	84.64	790.18
10H-3, 96–97	74.66	76.22	29.59	2.14	0.09	3.48	0.68	0.90	2.41	0.21	113.30	1081.06
10H-4, 73–74	75.93	77.49	30.50	2.00	0.08	3.70	0.73	0.89	2.31	0.25	105.04	1102.59
11H-1, 74–75	80.94	82.50	27.27	1.36	0.07	3.07	0.68	0.41	1.37	0.11	98.23	1688.13
11H-2, 80–81	82.50	84.06	31.35	1.49	0.07	3.20	0.69	0.66	1.72	0.16	103.39	1374.15
11H-3, 74–75	83.94	85.50	32.45	1.28	0.05	2.46	0.48	0.46	1.45	0.13	83.06	1031.06
11H-4, 74–75	85.44	87.00	32.25	1.45	0.08	3.16	0.58	0.37	1.63	0.08	105.39	1641.32
11H-5, 74–75	86.94	88.50	29.49	1.21	0.07	2.57	0.53	0.30	1.12	0.09	101.44	1173.93
11H-6, 74–75	88.44	90.00	32.79	1.34	0.05	2.81	0.51	0.62	1.52	0.14	89.66	1318.84
11H-7, 48–49	89.68	91.24	31.53	1.38	0.05	2.96	0.58	0.64	1.60	0.17	95.42	1375.10
16X1, 73–75	128.83	130.39	3.65	0.57	0.01	1.27	0.31	41.53*	0.90	0.12	1049.52	1385.10
199-1217B-												
3H-2, 74–75	31.74	34.20	24.54	4.75	0.14	7.92	0.98	1.56	2.80	0.35	200.15	1072.26
3H-3, 74–75	33.24	35.70	23.94	5.03	0.17	5.87	0.83	1.14	3.15	0.18	278.92	3415.37
4H-1, 78–79	39.78	43.20	30.67	3.74	0.14	6.07	1.08	1.03	2.30	0.24	153.26	3554.83
4H-2, 78–79	41.28	44.70	25.35	4.10	0.18	5.31	1.34	1.29	2.46	0.18	179.54	2660.28
5H-1, 77–78	49.27	50.35	31.16	1.91	0.09	4.29	0.67	0.90	1.59	0.13	111.65	1260.02
5H-2, 77–78	50.77	51.85	29.41	2.33	0.10	4.91	0.72	0.90	1.73	0.14	119.20	1672.05
5H-3, 77–78	52.27	53.35	31.33	2.13	0.09	4.03	0.62	0.84	1.44	0.14	113.22	1272.26

Table T11 (continued).

Core, section, interval (cm)	Depth (mbsf)	Depth (mcd)	Si (wt%)	Al (wt%)	Ti (wt%)	Fe (wt%)	Mn (wt%)	Ca (wt%)	Mg (wt%)	P (wt%)	Sr (ppm)	Ba (ppm)
6H-1, 72–73	58.72	61.57	30.24	1.17	0.05	2.76	0.53	0.53	1.17	0.08	88.20	800.32
6H-2, 84–85	60.34	63.19	31.07	1.21	0.07	3.41	0.64	0.20	1.42	0.07	84.06	919.47
6H-3, 83–84	61.83	64.68	26.36	0.91	0.04	1.71	0.37	0.22	0.73	0.03	33.97	373.16
6H-4, 73–74	63.23	66.08	32.87	1.45	0.07	3.39	0.53	0.69	1.29	0.08	101.92	1075.70
6H-5, 73–74	64.73	67.58	30.81	2.14	0.11	5.02	0.58	0.94	1.41	0.15	113.02	1350.49
6H-6, 69–70	66.19	69.04	29.30	2.04	0.09	4.36	0.83	0.92	1.71	0.14	122.43	1322.75
7H-1, 75–76	68.25	70.63	27.77	3.11	0.15	6.25	1.03	1.37	2.49	0.30	138.79	1012.29
7H-2, 73–74	69.73	72.11	28.81	2.20	0.10	4.92	0.77	1.03	2.48	0.14	116.06	1027.68
7H-3, 73–74	71.23	73.61	28.10	2.43	0.11	5.03	0.77	1.10	2.73	0.29	108.55	947.08
7H-4, 73–74	72.73	75.11	28.26	1.92	0.09	4.38	0.71	0.91	2.65	0.18	107.46	975.35

Notes: * = this value is not reliable because 100% $CaCO_3$ is equivalent to 40% Ca (see "Explanatory Notes," this volume).
This table is also available in ASCII.

Table T12. Calcium carbonate and organic carbon data, Holes 1217A and 1217B.

Core, section, interval (cm)	Depth (mbsf)	$CaCO_3$ (wt%)	Organic C (wt%)	$CaCO_3$ (wt%)*
199-1217A-				
1H-2, 72–73	2.22	0.12	0.10	–3.89
1H-4, 38–39	4.88	0.11	0.10	–3.36
2H-2, 74–75	7.74	0.18	0.10	–1.69
2H-6, 74–75	12.94	0.23	0.03	–1.46
3H-1, 74–75	15.74	0.23	0.02	–1.38
3H-4, 84–85	20.34	0.31	0.00	0.38
4H-2, 73–74	26.73	42.42	0.09	45.73
4H-6, 73–74	31.73	6.85	0.00	5.24
5H-2, 74–75	36.24	0.17	0.03	–1.10
5H-5, 74–75	40.74	0.26	0.01	
6H-1, 52–53	44.02	0.28	0.02	0.04
6H-5, 45–46	49.04	0.29	0.01	–1.56
7H-2, 73–75	52.93	0.40	0.00	–2.97
7H-5, 76–78	57.46	0.33	0.00	–3.41
9H-2, 74–75	62.98	0.40	0.00	
9H-5, 113–114	67.22	0.82	0.00	
10H-1, 110–111	71.80	0.45	0.39	
10H-3, 96–97	74.66	0.56	0.00	–2.38
11H-1, 74–75	80.94	0.64	0.00	–3.61
11H-4, 74–75	85.44	0.65	0.25	–3.70
11H-7, 48–49	89.68	0.63	0.00	–3.01
16X-1, 73–75	128.83	83.55	0.22	
199-1217B-				
3H-2, 74–75	31.74	1.23	0.27	
4H-2, 78–79	41.28	0.54	0.00	
5H-2, 77–78	50.77	0.50	0.00	–2.35
6H-4, 73–74	63.23	0.28	0.32	–2.89
7H-3, 73–74	71.23	0.32	0.00	–1.87

Notes: * = calculated from Ca in weight percent. $CaCO_3$ calculated from Ca in weight percent is not given in some cases because weight percent salt and/or Ca data was unavailable. Negative values may be due to an assumed Ca contribution from aluminosilicates in the normative calculation (see the **"Explanatory Notes"** chapter). This table is also available in **ASCII.**

Table T13. Moisture and density measurements, Holes 1217A and 1217B.

Core, section, interval (cm)	Depth (mbsf)	Water content (%)	Density (g/cm³)			Porosity (%)
			Wet bulk	Dry bulk	Grain	
199-1217A-						
1H-1, 80–82	0.80	60.9	1.35	0.53	2.63	80.0
1H-2, 75–77	2.25	66.3	1.29	0.44	2.64	83.5
1H-3, 75–77	3.75	61.0	1.34	0.52	2.61	79.9
1H-4, 40–42	4.90	58.3	1.37	0.57	2.62	78.2
2H-1, 75–77	6.25	57.2	1.38	0.59	2.53	76.7
2H-2, 75–77	7.75	57.5	1.37	0.58	2.49	76.7
2H-4, 75–77	9.95	54.5	1.40	0.64	2.53	74.7
2H-5, 75–77	11.45	54.3	1.41	0.65	2.56	74.8
2H-6, 75–77	12.95	55.8	1.39	0.61	2.51	75.6
2H-7, 75–77	14.45	56.4	1.39	0.60	2.55	76.3
3H-1, 75–77	15.75	56.0	1.39	0.61	2.56	76.1
3H-2, 75–77	17.25	60.4	1.35	0.53	2.60	79.5
3H-3, 75–77	18.75	57.5	1.37	0.58	2.49	76.7
3H-4, 85–87	20.35	55.9	1.39	0.61	2.55	75.9
3H-5, 81–83	21.81	57.6	1.38	0.58	2.57	77.3
3H-6, 75–77	23.25	63.2	1.32	0.49	2.61	81.4
3H-7, 43–45	24.43	73.0	1.22	0.33	2.46	86.7
4H-1, 108–110	25.58	78.4	1.18	0.25	2.63	90.3
4H-2, 75–77	26.75	67.7	1.28	0.41	2.70	84.6
4H-4, 75–77	28.75	67.6	1.29	0.42	2.74	84.8
4H-5, 75–77	30.25	76.8	1.20	0.28	2.67	89.6
4H-6, 75–77	31.75	72.9	1.22	0.33	2.53	86.9
4H-7, 60–62	33.10	75.1	1.21	0.30	2.63	88.6
5H-1, 75–77	34.75	72.2	1.21	0.34	2.26	85.1
5H-2, 75–77	36.25	73.7	1.20	0.31	2.24	86.0
5H-3, 24–26	37.24	70.2	1.23	0.37	2.31	84.2
6H-1, 54–56	44.04	70.4	1.21	0.36	2.13	83.2
6H-4, 47–49	48.06	69.3	1.22	0.37	2.14	82.5
6H-5, 46–48	49.05	67.6	1.22	0.40	2.04	80.6
6H-6, 75–77	50.06	71.4	1.21	0.35	2.15	84.0
7H-1, 119–121	51.89	77.6	1.17	0.26	2.35	88.8
7H-2, 75–77	52.95	76.0	1.19	0.29	2.41	88.2
7H-3, 84–86	54.54	76.7	1.18	0.27	2.32	88.2
7H-4, 75–77	55.95	77.3	1.18	0.27	2.36	88.7
7H-5, 73–75	57.43	78.2	1.16	0.25	2.19	88.5
7H-6, 75–77	58.95	78.1	1.17	0.26	2.31	89.0
7H-7, 18–20	59.88	79.2	1.16	0.24	2.24	89.3
9H-4, 110–112	65.69	79.0	1.17	0.25	2.53	90.3
10H-2, 75–77	72.95	79.4	1.16	0.24	2.30	89.6
10H-3, 98–100	74.68	78.9	1.17	0.25	2.40	89.8
10H-4, 75–77	75.95	76.8	1.18	0.27	2.32	88.2
11H-1, 75–77	80.95	77.7	1.18	0.26	2.42	89.2
11H-2, 81–83	82.51	77.9	1.17	0.26	2.27	88.7
11H-3, 75–77	83.95	77.6	1.17	0.26	2.27	88.5
11H-4, 75–77	85.45	78.5	1.17	0.25	2.33	89.2
11H-5, 75–77	86.95	78.5	1.16	0.25	2.28	89.0
11H-6, 75–77	88.45	77.6	1.16	0.26	2.22	88.2
11H-7, 49–51	89.69	77.1	1.18	0.27	2.37	88.6
16X-1, 73–74	128.83	31.4	1.79	1.23	2.73	55.0
199-1217B-						
3H-1, 75–77	30.25	75.9	1.21	0.29	2.73	89.3
3H-2, 75–77	31.75	73.0	1.23	0.33	2.70	87.7
3H-3, 75–77	33.25	77.5	1.20	0.27	2.82	90.5
3H-4, 75–77	34.75	71.9	1.22	0.34	2.32	85.3
3H-5, 75–77	36.25	72.9	1.20	0.33	2.29	85.8
3H-6, 75–77	37.75	67.2	1.28	0.42	2.59	83.8
4H-1, 75–77	39.75	73.3	1.22	0.33	2.58	87.4
4H-2, 75–77	41.25	73.8	1.21	0.32	2.43	86.9
5H-1, 75–77	49.25	79.1	1.16	0.24	2.42	89.9
5H-2, 75–77	50.75	77.1	1.18	0.27	2.40	88.8
5H-3, 75–77	52.25	76.4	1.18	0.28	2.37	88.2
6H-1, 75–77	58.75	78.9	1.16	0.24	2.27	89.2
6H-2, 85–87	60.35	78.8	1.17	0.25	2.42	89.8
6H-3, 85–87	61.85	76.6	1.18	0.28	2.31	88.1
6H-4, 75–77	63.25	78.8	1.16	0.25	2.25	89.1
6H-5, 75–77	64.75	76.7	1.18	0.27	2.29	88.0
6H-6, 71–73	66.21	76.6	1.18	0.28	2.38	88.4
7H-2, 75–77	69.75	77.1	1.18	0.27	2.47	89.0
7H-3, 75–77	71.25	78.6	1.16	0.25	2.30	89.2
7H-4, 75–77	72.75	79.3	1.16	0.24	2.41	90.0
7H-5, 75–77	74.25	79.2	1.17	0.24	2.51	90.3

Note: This table is also available in **ASCII.**

Table T14. LAS-based mineralogy, Hole 1217A.

Core, section, interval (cm)	Depth (mbsf)	Calcite (model wt%)	Opal (model wt%)	Smectite (model wt%)	Illite (model wt%)
199-1217A-					
1H-1, 24–26	0.25	0.00	19.60	7.81	72.59
1H-1, 80–82	0.81	0.00	15.23	11.67	73.11
1H-2, 23–25	1.74	0.00	23.13	49.57	27.30
1H-2, 75–77	2.26	0.00	16.21	26.58	57.21
1H-3, 23–25	3.24	0.00	16.02	47.26	36.72
1H-3, 75–77	3.76	0.00	10.76	32.67	56.57
1H-4, 26–29	4.77	0.00	9.83	51.37	38.80
1H-4, 40–42	4.91	4.46	0.00	36.35	59.19
2H-1, 21–23	5.72	0.00	19.01	75.92	5.07
2H-1, 75–77	6.26	0.00	9.54	63.42	27.04
2H-2, 21–23	7.22	0.00	19.55	80.45	0.00
2H-2, 75–77	7.76	0.00	3.99	76.44	19.57
2H-3, 21–23	8.72	0.00	17.67	82.33	0.00
2H-4, 23–25	9.44	0.00	19.59	80.41	0.00
2H-4, 75–77	9.96	0.00	14.23	81.63	4.14
2H-5, 23–25	10.94	0.00	19.96	71.69	8.35
2H-5, 75–77	11.46	4.75	20.65	47.30	27.31
2H-6, 23–25	12.44	0.00	24.03	72.61	3.36
2H-6, 75–77	12.96	0.00	23.93	73.48	2.59
2H-7, 23–25	13.94	0.00	29.53	70.47	0.00
2H-7, 75–77	14.46	7.73	28.73	63.54	0.00
3H-1, 75–77	15.76	12.05	29.90	58.05	0.00
3H-2, 23–25	16.74	0.91	29.35	69.74	0.00
3H-2, 75–77	17.26	1.30	29.14	69.56	0.00
3H-3, 23–25	18.24	0.00	29.24	70.76	0.00
3H-3, 75–77	18.76	3.09	28.68	68.24	0.00
3H-4, 23–25	19.74	10.68	30.75	58.57	0.00
3H-4, 85–87	20.36	6.69	27.55	65.76	0.00
3H-5, 23–25	21.24	10.37	26.89	62.74	0.00
3H-5, 81–83	21.82	1.61	27.07	71.32	0.00
3H-6, 23–25	22.74	10.64	23.08	66.28	0.00
3H-6, 75–77	23.26	5.68	22.73	71.59	0.00
3H-7, 23–25	24.24	0.00	23.28	76.72	0.00
3H-7, 43–45	24.44	0.00	20.95	79.05	0.00
4H-1, 108–110	25.59	6.08	10.23	83.69	0.00
4H-1, 124–126	25.75	0.00	24.89	75.11	0.00
4H-2, 23–25	26.24	5.52	30.23	64.24	0.00
4H-2, 75–77	26.76	38.12	3.60	58.28	0.00
4H-3, 23–25	27.74	43.43	8.73	47.85	0.00
4H-4, 8–10	28.09	17.08	58.33	24.59	0.00
4H-4, 75–77	28.76	35.04	4.43	60.54	0.00
4H-5, 23–25	29.74	12.15	23.93	63.92	0.00
4H-5, 75–77	30.26	22.27	22.30	55.43	0.00
4H-6, 23–26	31.24	18.80	21.11	60.09	0.00
4H-6, 75–77	31.76	11.45	43.56	44.99	0.00
4H-7, 23–25	32.74	7.84	17.71	74.45	0.00
4H-7, 60–62	33.11	9.79	14.53	75.68	0.00
5H-1, 23–25	34.24	0.00	20.68	79.32	0.00
5H-1, 75–77	34.76	0.00	19.25	80.75	0.00
5H-1, 125–127	35.26	0.00	23.20	76.80	0.00
5H-2, 23–25	35.74	0.00	15.77	84.23	0.00
5H-2, 75–77	36.26	0.00	16.77	83.23	0.00
5H-3, 17–19	37.18	0.00	24.72	75.28	0.00
5H-3, 24–26	37.25	0.00	19.91	80.09	0.00
5H-7, 33–35	43.34	0.00	17.34	82.66	0.00
6H-1, 23–25	43.74	0.00	21.18	78.82	0.00
6H-1, 54–56	44.05	0.00	16.66	83.34	0.00
6H-4, 23–25	47.83	0.00	18.90	81.10	0.00
6H-4, 47–49	48.07	0.00	20.14	79.86	0.00
6H-5, 20–22	48.80	0.00	24.16	75.84	0.00
6H-5, 46–48	49.06	0.00	23.04	76.96	0.00
6H-6, 23–25	49.55	0.00	21.40	78.60	0.00
6H-6, 75–77	50.07	0.00	19.61	80.39	0.00
7H-1, 119–121	51.90	12.51	44.80	35.47	7.22
7H-1, 140–142	52.11	11.25	44.79	34.42	9.54
7H-2, 23–25	52.44	13.06	44.99	33.45	8.51
7H-2, 75–77	52.96	9.40	42.19	41.89	6.52
7H-3, 23–25	53.94	4.54	53.01	39.82	2.63
7H-3, 84–86	54.55	9.76	47.28	34.95	8.01
7H-4, 23–25	55.44	11.79	48.80	29.88	9.54
7H-4, 75–77	55.96	5.23	55.73	37.30	1.74
7H-5, 23–25	56.94	10.33	43.86	43.17	2.65
7H-5, 73–75	57.44	5.65	49.92	41.44	2.99
7H-6, 23–25	58.44	13.02	43.39	33.71	9.88
7H-6, 75–77	58.96	1.65	49.27	49.09	0.00
7H-7, 18–20	59.89	0.00	52.40	47.61	0.00
7H-7, 54–56	60.25	3.98	54.85	41.17	0.00
9H-2, 24–26	62.49	1.85	44.90	51.02	2.23
9H-3, 24–26	63.34	25.72	22.15	45.47	6.66
9H-4, 24–26	64.84	21.02	19.09	59.89	0.00
9H-4, 110–112	65.70	18.10	18.75	63.15	0.00
9H-5, 24–26	66.34	24.01	12.72	63.28	0.00
9H-6, 24–26	67.84	14.91	25.84	59.25	0.00
10H-1, 124–126	71.95	5.07	36.26	58.67	0.00
10H-2, 23–25	72.44	23.83	29.56	46.62	0.00
10H-2, 75–77	72.96	1.09	47.83	51.09	0.00
10H-3, 23–25	73.94	17.21	33.16	49.64	0.00
10H-3, 98–100	74.69	13.98	34.94	51.08	0.00
10H-4, 23–25	75.44	18.86	33.08	48.06	0.00
10H-4, 75–77	75.96	11.02	35.38	53.60	0.00
11H-1, 75–77	80.96	9.48	39.14	51.39	0.00
11H-2, 23–25	81.94	12.31	34.51	53.17	0.00
11H-2, 81–83	82.52	4.17	42.90	52.93	0.00
11H-3, 23–25	83.44	10.67	39.65	49.69	0.00
11H-3, 75–77	83.96	3.31	48.46	48.23	0.00
11H-4, 23–25	84.94	7.33	41.66	51.01	0.00
11H-4, 75–77	85.46	4.26	45.18	50.57	0.00
11H-5, 23–25	86.44	9.07	29.18	61.75	0.00
11H-5, 75–77	86.96	4.25	47.70	48.04	0.00
11H-6, 23–25	87.94	10.47	30.21	59.32	0.00
11H-6, 75–77	88.46	2.20	46.20	51.60	0.00
11H-7, 23–25	89.44	10.22	38.53	51.24	0.00
11H-7, 49–51	89.70	3.73	43.66	52.61	0.00
16X-1, 73–75	128.84	62.54	0.00	37.46	0.00

Notes: This table is also available in **ASCII**. [**N1**]

Table T15. Split-core velocity measurements, Holes 1217A and 1217B.

Core, section, interval (cm)	Depth (mbsf)	Velocity (m/s)			Anisotropy (%)
		z*	y*	x†	
199-1217A-					
1H-1, 81	0.81	1474	1490		1.1
1H-2, 76	2.26	1475	1496		1.4
1H-3, 76	3.76	1479	1493		0.9
1H-4, 41	4.91	1478	1492		0.9
2H-1, 76	6.26	1481	1495		1.0
2H-2, 76	7.76	1487	1497		0.7
2H-4, 76	9.96	1493	1508		1.0
2H-5, 76	11.46	1499	1511		0.8
2H-6, 76	12.96	1502	1516		0.9
2H-7, 76	14.46	1505	1523		1.2
3H-1, 76	15.76	1508	1524		1.1
3H-2, 76	17.26	1503	1513		0.7
3H-3, 76	18.76	1508	1517		0.6
3H-4, 86	20.36	1510	1538		1.8
3H-5, 82	21.82	1514	1525		0.7
3H-6, 76	23.26	1502	1521		1.2
3H-7, 45	24.45			1545	
4H-1, 109	25.59	1514	1524		0.6
4H-2, 76	26.76			1533	
4H-4, 76	28.76			1525	
4H-5, 76	30.26	1538	1528		–0.7
4H-6, 76	31.76	1510	1556		3.0
4H-7, 61	33.11			1563	
5H-1, 76	34.76	1512	1527		1.0
5H-2, 76	36.26	1515	1535		1.3
5H-3, 25	37.25	1508	1518		0.6
6H-1, 55	44.05	1512	1526		0.9
6H-4, 48	48.07	1499	1510		0.7
6H-5, 47	49.06	1499	1506		0.5
6H-6, 76	50.07	1500	1510		0.7
7H-1, 120	51.9			1558	
7H-2, 76	52.96			1574	
7H-3, 85	54.55			1565	
7H-4, 76	55.96			1557	
7H-5, 74	57.44			1559	
7H-6, 76	58.96			1563	
7H-7, 19	59.89			1567	
10H-2, 76	72.96			1550	
10H-3, 99	74.69			1554	
10H-4, 76	75.96			1564	
11H-1, 76	80.96			1569	
11H-2, 82	82.52			1569	
11H-3, 76	83.96			1569	
11H-4, 76	85.46			1570	
11H-5, 76	86.96			1577	
11H-6, 76	88.46			1572	
11H-7, 50	89.7			1573	
16X-1, 74	128.84	1595		1588	
199-1217B-					
3H-1, 76	30.26			1581	
3H-2, 76	31.76			1569	
3H-3, 76	33.26			1538	
3H-4, 76	34.76			1520	
3H-5, 76	36.26			1523	
3H-6, 76	37.76			1532	
4H-1, 76	39.76			1547	
4H-2, 76	41.26			1526	
5H-1, 76	49.26			1565	
5H-2, 76	50.76			1561	
5H-3, 76	52.26			1568	
6H-1, 76	58.76			1565	
6H-2, 85	60.35			1573	
6H-3, 85	61.85			1558	
6H-4, 76	63.26			1574	
6H-5, 76	64.76			1564	
6H-6, 71	66.21			1560	
7H-2, 76	69.76			1563	
7H-3, 76	71.26			1568	
7H-4, 76	72.76			1571	
7H-5, 76	74.26			1559	

Notes: * = determined by insertion probe, † = determined by contact probe. This table is also available in **ASCII.**

Table T16. Thermal conductivity, Hole 1217A.

Core, section, interval (cm)	Depth (mbsf)	Thermal conductivity (W/[m·K])
199-1217A-		
1H-3, 76	3.76	0.80
2H-3, 32	8.82	0.79
3H-3, 76	18.76	0.76
4H-2, 76	26.76	0.78
5H-3, 76	37.76	0.76
6H-3, 76	46.85	0.74
7H-3, 76	54.46	0.73
10H-3, 76	74.46	0.66
11H-3, 76	83.96	0.71

Note: This table is also available in **ASCII.**

CHAPTER NOTE

N1. 13 December 2002—After the CD-ROM version of this volume was published, errors were noted in the ASCII versions of Tables T5 and T14. This version contains the corrected ASCII files.

*Dates reflect file corrections or revisions.